Electronic transport and magnetization dynamics in magnetic systems

Simone Borlenghi

To cite this version:

Simone Borlenghi. Electronic transport and magnetization dynamics in magnetic systems. Matière Condensée [cond-mat]. Université Pierre et Marie Curie - Paris VI, 2011. Français. NNT : . tel-00590363

HAL Id: tel-00590363
https://theses.hal.science/tel-00590363

Submitted on 3 May 2011

THÈSE DE DOCTORAT DE L'UNIVERSITÉ PARIS VI
préparée au Sérvice de Physique de l'État Condensé du CEA Saclay

Electronic transport and magnetization dynamics in magnetic systems

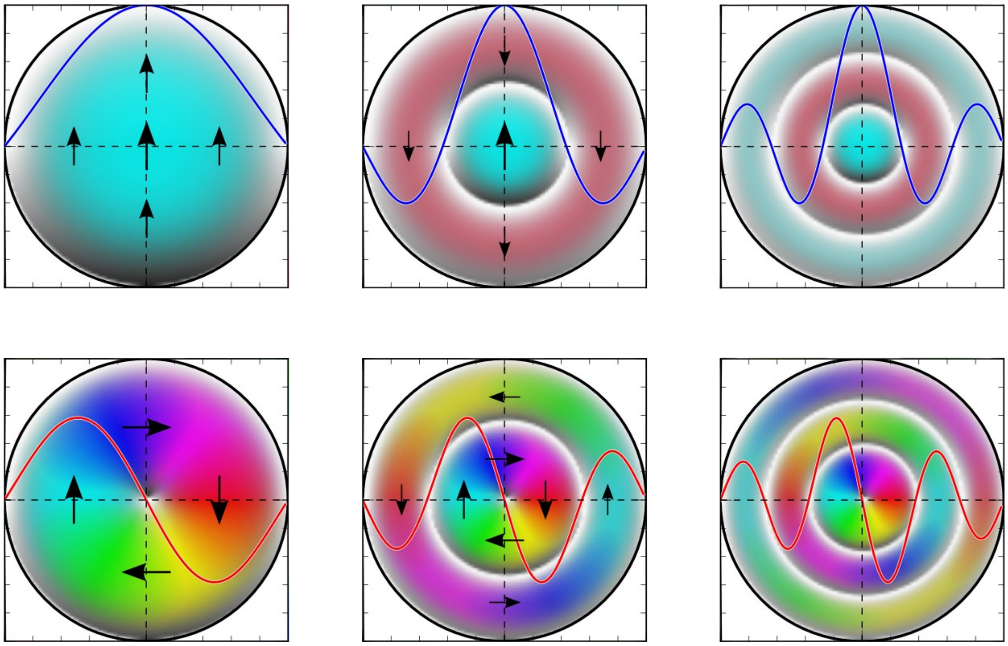

- Simone BORLENGHI -

UNIVERSITÉ PARIS VI – CEA SACLAY
ÉCOLE DOCTORALE 107

Doctorat de Physique - Physique du solide

Simone BORLENGHI GAROIA

ELECTRONIC TRANSPORT AND MAGNETIZATION DYNAMICS IN MAGNETIC SYSTEMS

Thèse présentée pour obtenir le grade de
DOCTEUR DE L'UNIVERSITÉ PIERRE ET MARIE CURIE

Cette thèse, préparée au laboratoire SPEC (CEA/DSM/IRAMIS) au sein du Groupe NanoMagnétisme, a été encadrée par Olivier KLEIN et Xavier WAINTAL.

Composition du Jury:

Mairbek CHSHIEV	Rapporteur
Robert J. HICKEN	Rapporteur
Olivier KLEIN	Directeur de thèse
William SACKS	Examinateur
Nicolas VUKADINOVIC	Examinateur
Xavier WAINTAL	Invité

Special Thanks

This thesis has been a real team work: many people have given theor contribution, especially to the experimental part.

First of all I wish to thank my advisors, Olivier Klein and Xavier Waintal, for their support and their committement in this project. Then I wish to thank the other people who have contributed to this work: Valentin Rychkov, with whom I have worked the first year of my thesis; Gregoire de Loubens and Vladimir Naletov who have performed the experiments.

I thank sincerely the members of my thesis commission for having accepted to examinate my work, and for their useful and pertinent comments, corrections and suggestions.

A special thanks goes to all the other Ph.D. Students and postdocs that I have met during these years: Julie, Jeremie, Phuong-Ahn, Andrey, Tibault, Aurelie, Sébastien, Preden, Ivana, Eva, Keyan, Jean-Damien. With all of them I have always experienced passion for work as well as cooperation and mutual support during the most stressful periods. A very special thanks goes to Remy for many reasons: first he has hosted me (and my luggage) in his 20 m^2 flat when I have been evicted from my appartement, then he has always been forthcoming when I needed someone to talk with (not only about Physics).

Concerning more personal things, these years have been the most difficult of my life, for many reasons. As far as I could see speaking with my colleagues, Ph.D. thesis is tough and stressful for everyone, since in three years one has to learn how to do research, how to talk in public, how to be autonomous, how to correct (or better, avoid) stupid mistakes. Research is made of complicate, difficult and fascinating problems which have to be resolved in many small steps. In each step the probability of making a stupid mistake or to get stuck is quite high, so that one spends most of the time making corrections and thinking about how to move one step further to the next small problem (where one is very likely to make other errors).

It took me three years to realize that, and to see that research is like playing with Lego, without the instructions that tell you how to stick the next piece. Personally, I think that this is passionating and challenging. At the end of my thesis I have seen all the “Lego pieces” going together to make a beautiful construction, and it has been a pleasure to see that this construction is something that explains how the reality (a small part of it) works. The most difficult part of all this is not the problem itself, but to stay optimistic when things go wrong, and to be perseverant and resilient in front of everyday small (and not so small) failures.

During these three years the presence of family and friends has been determinant. I thank my parents for their support throughout all this time. They have helped me in many practical things and they have always been present to encourage me.

A great thanks goes to Doris for her love, energy, curiosity and optimism, which made the last year of my life extraordinary.

And thanks to my friends: Ilsa and Michel, Pepe, Martina, Roberta, Giacomo, Fabrizio, Francesco, Enrico, Khadija, Alberto, Valentino, Benedetta, Nassim.

To conclude, I wish to thank some people that have been determinant for me. Elisabetta Biella, my professor of latin and greek at high school. I have never worked so hard in my life as in that period, and sometimes I still have nightmares about latin and greek examinations. But with her I have learnt that effort is rewarding, and that the hard and boring study of the grammar is the prelude to appreciate a beautiful latin poem.

Antonio Fontana, professor of philosophy, and Furio Gramatica, professor of mathematics and physics. They have awakened my curiosity in front of the huge, complicate and fashinating World.

Contents

Chapter 1

Introduction

The understanding of the mutual influence between spin polarized current and magnetization dynamics in solid state mesoscopic systems, boths from experimental and theoretical point of view, is at the basis of spintronic, the science aiming at utilizing spin-dependent effects in the electronic transport properties [105].

Technological progress in the fabrication of hybrid structures using magnetic metals as well as in nano-lithography has allowed the realization of mesoscopic devices, called *spin valves*, consisting of alternating stacks of ferromagnetic (F) and normal (N) metals, where spin dependent transport properties depend on the relative orientation of the magnetization inside the F layers.

Spin valves exhibits the well-known *giant magneto-resistance* (GMR) effect [6, 11], that is, the resistance depends on the relative angle between the magnetizations of the F layers. Nowadays, this useful property is extensively used in magnetic sensors [33, 72].

The converse effect, discovered in 1996 independently by J. C. Slonczewski [88] and L. Berger [9] is that a direct current can transfer spin angular momentum between two magnetic layers separated by either a normal metal or a thin insulating layer. This phenomenon, called *spin torque*, leads to a very efficient destabilization of the orientation of a magnetic moments [95], which can induce stable precession or reversal of the magnetization inside the F layers [57]. Practical applications are the possibility to control through a current the digital information in magnetic random access memories (MRAMs) [3, 43] or to produce high frequency signals in spin transfer nano-oscillators (STNOs) [76].

The first theoretical description of GMR effect in *collinear* spin valves (*i.e.* systems where the magnetizations in the two F layers are aligned or antialigned) was given by T. Valet and A. Fert in 1993 [97]. After that, many approaches have been developed to treat the more general case of electronic transport through *non collinear* spin valves, where the magnetization between the two F layers are not aligned. These approaches range from purely quantum [89, 16, 34] to semi-classical Boltzman equation, circuit theory [15] and generalized circuit theory [7] or Random Matrix Theory (RMT) [8, 103], and allow to calculate local (spin current, spin accumulation and spin torque) and global (resistance) transport properies of magnetic multilayers. A good understanding has now been reached in the respective domains of applicability and links between the various approaches. The reader can find a comprehensive introduction to spintronic and to the different approaches to spin transport in Refs. [47] and [14].

The most important aspects of these mesoscopic devices is that magnetization dynamics and spin transport are coupled: a given magnetic configuration has an influence on the propagation of current (GMR effect), which itself influences the dynamics of the magnetization (spin torque). The physics of such systems cannot be properly captured by simple (analytically tractable) models, and numerical simulations that treat the magnetic and transport degrees of freedom *on an equal footing* are needed. At present, micromagnetic simulations [37] can describe correctly the dynamics of the magnetization, whithout taking into account the effect of spin transfer on the dynamics. Concerning simulations that couple magnetic and transport degrees of freedom, several steps have already been taken in that direction [49, 108, 10], which are based on two possible strategies: i) the three dimensional texture of the magnetization inside the sample is described correctly using micromagnetic simulations, but the spatial variation of spin torque is neglected or ii) the spatial variation of the magnetization is neglected, using a macrospin approximation and spin torque is then introduced. These approximations neglect the effects related to the spatial inhomogeneity of transport and magnetization inside the sample, which are determinant for a deep understanding of the physics of these systems. In particular, macrospin approximation cannot simulate the different spin wave modes excited by spin transfer effect, which are essential characteristics of a STNO. The main novelty of this work is that we have developed an approach that takes into account correctly both the spatial variation of spin torque and the three dimensional texture of the magnetization inside a realistic spin valve.

The first part of this work is dedicated to the development of a general and flexible model of electronic transport in magnetic mesoscopic devices, that allows to calculate local and global transport properties. Our model of transport consists in two different and complementary approaches, both related to the Landauer-Buttiker formalism [19]. The first approach, called Continuous Random Matrix Theory (CRMT) [79] is a model based on RMT, which allows to include classical concepts like spin accumulations and chemical potentials into scattering formalism. The second approach is based on an effective Tight-Binding (TB) model for magnetic multilayers. The TB model is solved at a purely quantum level using the Non Equlibrium Green Function (NEGF) formalism [27, 53], and can describe systems with arbitrary geometry and connected to an arbitrary number of electronic reservoirs. For diffusive materials, we find a close agreement of TB with CRMT so that the same parametrization can be used for both. Indeed CRMT is an extension of the Valet-Fert diffusive equation [97] to non collinear systems, so that non Ohmic materials have to be described at the quantum level. On the other hand, a full numerical simulations of a realistic spin valve is prohibitive at the TB level. We show how one can combine CRMT with TB method in a multiscale approach, to consider realistic systems where CRMT alone is not applicable. Since CRMT is parametrized by the same set of experimentally accessible parameters as the Valet-Fert theory [97], it has *no free parameters* and can describe many ohmic materials.

In the second part of this work, we have coupled CRMT to Nmag [37], a finite element micromagnetic solver, and we have included spin transfer effect into micromagnetic simulations, taking into account the three dimensional texture of magnetization and spin transfer. This has allowed to simulate the dynamics of a perpendicularly magnetized circular nanopillar crossed by a dc Current Perpendicular to the Plane (CPP) of the layers. A comprehensive analysis of the Spin Wave (SW) spectrum of this system has allowed for a precise identification the modes excited by spin transfer, and of the associated selection rules. A detailed comparison with Ferromagnetic Resonance (FMR) experiment performed with Ferromagnetic Resonance Force Microscope (MRFM) [23, 28, 31] have shown the effectiveness of our model.

To summarize, The construction and the application of a general and flexible spin transport model, that allows to describe in a realistic way the complexity of both electronic transport and magnetization dynamics, is the main achievement of this work. This manuscript is organised as follows:

Chapter 2 consists in an introduction to spintronic and quantum transport. We start with an overview on magnetic multilayers and on the Valet-Fert theory, and we describe the problem in a general way introducing a quantum Hamiltonian for itinerant electrons. This allows to introduce the concepts of spin current and spin torque, whose definition and computation is the main problem faced in the development of our transport models. We introduce also NEGF formalism, scattering matrix theory and Random matrix theory, which constitute the basis of CRMT and TB approaches, and allow to relate them in a direct way.

Chapter 3 is devoted to the description of CRMT, and of the link with Valet-Fert and generalized circuit theory. The model is then applied to the computation of the angular dependence of spin accumulation and spin torque in spin valves.

Chapter 4 contains a detailed description of the TB approach. The model is applied to the computation of transport properties of different bulk materials and spin valves, like spin current, spin torque and magnetoresistance. A comparison with CRMT shows the equivalence of these models for Ohmic conductors, and allows to parameterize TB model. The CRMT/TB multiscale approach is then implemented in a natural way using the Fisher-Lee formula [38], that relates scattering and Green function formalism.

Chapter 5 provides an introduction to the Landau-Lifshitz-Gilbert (LLG) equation [62], to describe the magnetization dynamics in ferromagnets. In particular, we show how to introduce spin torque into the LLG equation according to the Slonczewski-Berger model. Then, we describe an analytical model for spin wave modes [45] inside the simplest possible geometry: the normally magnetized circular spin-valve nano-pillar. This allows to describe the coupled dynamics of the two F layers, to classify spin wave modes according to their symmetries, and to introduce selection rules for SW excitations.

Chapter 6 contains the main results of this work. At first, we describe the MRFM experiment that has allowed to determine the spectrum of the STNO, under the influence of different excitations (rf field, rf current and dc current). Thanks to the preserved axial symmetry, a simplified spectroscopic signature of the different SW eigen-modes is expected. Then, we have performed micromagnetic simulations with spin torque, obtained coupling CRMT to Nmag, and we have compared the simulations with experimental datas. This has allowed to characterize the spectrum of the nanopillar given by dc current excitation, and to determine the selection rules for the excited SW modes. The predictions are coherent with the experimental results, and provide an good test for CRMT as well as a good interpretation of experiments.

1.1 Spin transport in multilayers: a brief introduction

In this work we focus on the transport properties of alternating stacks of Ferromagnetic (F) and non magnetic (or normal-N) materials (multilayers), with sizes ranging from some nanometers to some hundredths of nanometers. Although the model we shall develop in next chapters is quite general (we can describe systems with arbitrary geometry and connected to an arbitrary number of electron reservoirs), we shall restrict to FNF trilayers connected to two contacts, traversed by a current perpendicular to the plane of the layers (CPP configuration). The conctacts (called *leads*) are assumed to be perfect nonmagnetic conductors, through which electrons propagate like in a waveguide, encountering a negligible resistance (the concept of resistance for a perfect conductor shall be described in the follwing chapters).

Transport properties inside ferromagnets depend on the orientation of spins with respect to the localised magnetic moments of the material. In a first approximation, we shall consider that the localized magnetic moments have uniform orientation inside the whole ferromagnetic layer. This simplification allows to consider the assembly of these moments as a single

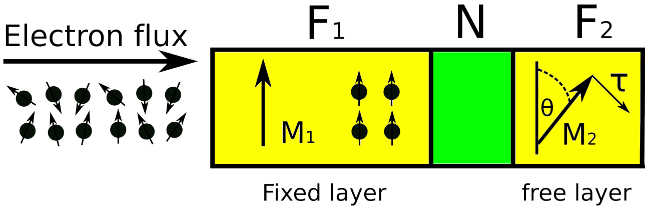

Figure 1.1: Cartoon of an FNF trilayer. A flux of unpolarized electrons impinges layer F_1, with magnetization $\boldsymbol{M}_1$. The spins of incoming electrons, polarized along $\boldsymbol{M}_1$, produce a torque $\boldsymbol{\tau}$ on $\boldsymbol{M}_2$, which depends on the angle θ. between $\boldsymbol{M}_1$ and $\boldsymbol{M}_2$. The resistance of the system depends on the mutual orientation of $\boldsymbol{M}_1$ and $\boldsymbol{M}_2$: it is minimal in the parallel state and maximal in the antiparallel.

magnetization vector $\boldsymbol{M}$. In the following (chapers 5 and 6) whe shall see the exact meaning of this approximation, and how to describe electronic transport in case of a non-uniform magnetization texture.

Let us consider a $\mathrm{F}_1\mathrm{N}\mathrm{F}_2$ system like the one depicted in FIG.(1.1), where the two magnetic layers F_1 and F_2 have magnetization $\boldsymbol{M}_1$ and $\boldsymbol{M}_2$ correspondingly, and electrons near the Fermi energy propagate from left to right. Inside a ferromagnet, conduction electrons with spin parallel to the magnetization (majority, "up"- ↑ electrons), have lower resistiviy than electrons with spin antiparallel to the magnetization (minority, "down"-↓ electrons). While crossing F_1, electrons are *spin polarized* through exchange interaction with the localised magnetic moments of the layer, so that their spins align with $\boldsymbol{M}_1$. As a consequence, an FNF trilayer has lower resistivity in parallel than in antiparallel configuration. As we shall see, the resistance depends on the angle θ between $\boldsymbol{M}_1$ and $\boldsymbol{M}_2$. For this property, FNF multilayers are called *spin valves*: acting on the magnetization it is possible to regulate the resistance of the system, and consequently the current flowing through it.

This effect, known as *Giant Magneto Resistance*, has been observed for the first time by M. N. Baibich *et al.* [6] and G. Binash *et al.* [11], and has been described within a diffusive model by T. Valet and A. Fert [97] for collinear spin valves. Transport properties of these systems are related to two important lengthscales: the mean free path l_σ, which corresponds to the mean distance traveled by an electron with spin $\sigma =\uparrow,\downarrow$ between two collisions, and the spin diffusion (or spin flip) length l_{sf}, which corresponds to the mean distance traveled by an electron before its spin is changed, from up do down or vice-versa (typically by spin-orbit interaction). l_σ is directly related to the resistivity of the spin channel σ, while l_{sf} gives a lengthscale below which electrons mantain their spin polarization (shorter in ferromagnet than in normal materials), and transport depends on spin. Conductors are called *ballistic* if they are shorter than the mean free path,

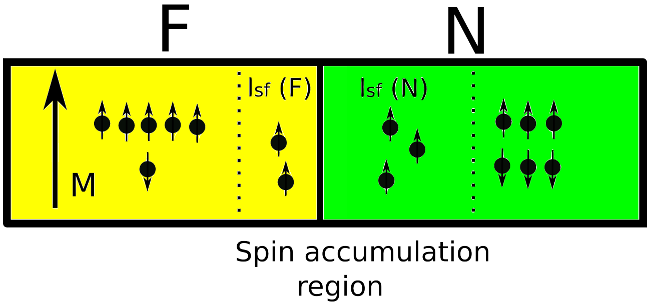

Figure 1.2: Cartoon that represents a F/N interface. Inside the F material, the current is highly polarized along $\boldsymbol{M}$, while inside the N material the current polarization goes to zero. At the interface between the two layers, there is a region of spin accumulation (in this case, of up spins), which extends over the spin diffusion lengths $l_{sf}(F)$ and $l_{sf}(N)$.

and *diffusive* if they are longer than the mean free path [26]. In this work we shall focus on diffusive conductors shorter than the spin diffusion length.

Let us consider FIG.(1.2), which represents the interface between a ferromagnet F and a normal metal N. Inside F majority electrons carry more current than minority electrons, while inside N both spin channels carry the same current. Therefore, there is an *accumulation* of majority electrons within a distance smaller than l_{sf} from the F/N interface. this means that the two spin channels have different chemical potentials μ_σ, to which correspond a diffusion *spin current* j_σ. The degree of spin polarization of the current is defined as $P = (j_\uparrow - j_\downarrow)/(j_\uparrow + j_\downarrow)$, and vanishes inside a normal metal far from the F/N interface. In this description, both the bulk materials and the F/N interfaces are responsible for the resistance of the system [97].

So far we have described the effect of the magnetization on transport, now we shall focus on *spin transfer*, an effect discovered independently by Slonzcewski [88] and Berger [9], which allows to manipulate the dynamics of the magnetization in a ferromagnet through a spin polarized current. Let us consider an electron at the Fermi energy that enters a ferromagnet. If its spin has a component transverse to the magnetization of the ferromagnet, the electron is described by the linear superposition $|\psi(r,t)\rangle = a_\uparrow(r,t)|k_F^\uparrow\rangle + a_\downarrow(r,t)|k_F^\downarrow\rangle$ of k_F^σ being the wavevector at the Fermi energy for spin $\sigma = \uparrow / \downarrow$. The two coefficients $a_\sigma(r,t)$ oscillate as a function of the position (this corresponds to the precession of the spin around the exchange field H_{sd} [94]). This transverse component of the spin is "absorbed" within a length $l_\perp \propto \pi/|k_F^\uparrow - k_F^\downarrow|$ of a few nanometers, and the magnetic moment associated to the transverse spin is transferred to the localised magnetic moments of the ferromagnet. Spin transfer effect acts as a *spin torque* that destabilizes the magnetization [FIG.(1.1)]. In our description, F_1 (called

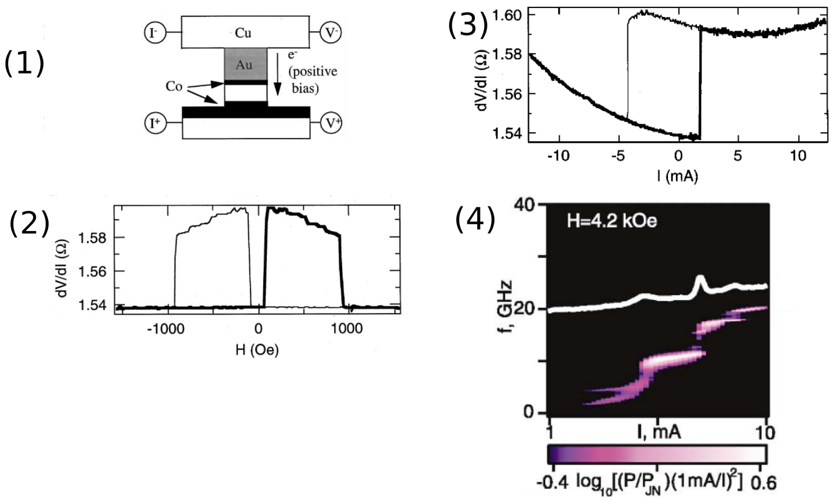

Figure 1.3: **Current induced magnetization reversal** (1) Schematic of the nanopillar used in the experiment: two Cobalt (Co) layers of 40 nm (polarizer) and 2.5 nm (free layer) are separated by a Copper (Cu) spacer of 6 nm. The nanopillar has section 120 × 60 nm. (2) GMR graph of the nanopillar: an external applied field controls the relative orientations of the magnetizations in the two Co layers: parallel and antiparallel states correspond to low and high resistance states. (3) Figure showing the magnetization reversal by spin transfer effect: at zero applied field, a dc current stabilizes parallel and antiparallel states. The current density needed to reverse the magnetization is around 10^7 A/cm^2. Figures extracted from Ref.[3].(4) **Spin wave generation**. The system used in this experiment is a $Co_{40nm}Cu_{10nm}Py_{3nm}$ nanopillar with section 120 × 70 nm. For certain values of the current, the plot dV/dI has some peaks, corresponding to the precession of the free Py layer. Figure extracted from Ref.[56].

fixed layer) acts as a polariser and F_2 (called free layer) is affected by spin torque. Electrons flowing through F_1 are spin polarized along $\boldsymbol{M}_1$ and exert a torque on $\boldsymbol{M}_2$ proportional to $J[\boldsymbol{M}_2\times(\boldsymbol{M}_2\times\boldsymbol{M}_1)]$ [88], J being the current per unit surface crossing F_2. When $\boldsymbol{M}_1$ and $\boldsymbol{M}_2$ are parallel or antiparallel, spin torque vanishes (since the component of spin transverse to $\boldsymbol{M}_2$ is zero). At sufficiently high current, spin torque induces a stable precession (or even a reversal) of $\boldsymbol{M}_2$ with respect to its equilibrium position, and tends to bring back $\boldsymbol{M}_1$ to its equilibrium position. Experimental results of stable precession and magnetization reversal are shown in FIG.(1.3). Changing the direction of the current reverses this situation: we can induce the precession of $\boldsymbol{M}_1$ and stabilize $\boldsymbol{M}_2$, so that choosing the thick layer as polarizer is just a matter of convenience. The dependence of spin torque on the direction of the bias current shall be discussed in details in chapter 2.

The dependence of resistance and spin torque on the mutual orientation of $\boldsymbol{M}_1$ and $\boldsymbol{M}_2$ accounts for the strong coupling between magnetization dynamics and transport properties: spin torque influences the dynamics of $\boldsymbol{M}_2$, which has an influence on the resistance of the system and on transport properties. This, together with the fact that both magnetization and transport properties are spatially inhomogeneus, are the main sources of complexity inside our system. In the following chapters we shall see how to provide a theory that takes into account these aspects. The leading idea is that transport properties depend on the *probability* of electrons to cross a system with different magnetic configurations. We shall see how the different physical quantities introduced above $(j_\sigma, \mu_\sigma, l_\sigma, l_{\text{sf}}, l_\perp)$ are related to these probabilities, and how to calculate transport properties of multilayers in a general way.

Chapter 2

Electronic transport and Random Matrix Theory

2.1 Introduction

In this chapter we review some well established models of electronic transport inside multilayers, and we introduce an approach based on Random Matrix Theory [8, 103], which constitutes the basis of the transport theory developed in chapter 3. In this work we consider diffusive conductors at low temperature and we neglect electron-electron or electron-magnon interaction. We consider conducting electrons near the Fermi energy, and we do not take into account the band structure of the material.

The physical picture we use is the following: an electron propagates in a semi infinite perfect conductor (called *lead*) until it crosses a conducting system. Here it undergoes a certain number of scattering events, due to impurities of the material, and then exits the system and goes through another lead. The system is characterized by some probability coefficients that tell how much the electron is likely to be transmitted or reflected. Global and local transport properties, such as conductance, spin current and spin torque, are related to these coefficients.

In Sec. (2.2) we describe two approaches to spin transport. At first we describe the **Valet-Fert (VF) theory** [97], a diffusive model that allows to describe electron propagation in collinear spin valves. The concept of spin accumulation and chemical potential are included in this model. The parameters of this theory, which are experimentally accessible, plays a key role in the formulation of **Continuous Random Matrix Theory (CRMT)**[79] described in chapter 3. The second approach is based on the description of multilayers using a general quantum Hamiltonian for conduction electrons [102], containing a kinetic part and an impurity potential, which accounts for different transport properties for majority and minority electrons and for spin flip phenomena. Using this Hamiltonian, we introduce the formalism for non collinear spin spin valves, and we define properly spin density, spin current and spin torque.

In Sec. (2.3) we review the **Landauer-Buttiker scattering formalism** [19]. Scattering matrices keep track of the spin degree of freedom and are sensitive to a rotation in spin space, and can describe non collinear spin valves.

In Sec. (2.4) we describe **Random Matrix Theory (RMT)** [8], which is related to the scattering matrix formalism, and provides a useful tool to express transport properties using simple concepts like transmission and reflection probabilities for an electron crossing the system. This formalism can describe non collinear spin valves [103], and it consitutes the basis for the semiclassical approach to spin transport described in chapter 4.

Sec. (2.5) is dedicated to an introduction to **Non Equilibrium Green's Function (NEGF) formalism** [27], through which one can describe quantum transport for conductors at finite temperature. In the case of non interacting electrons, and at low temperature, this formalism is equivalent to scattering formalism [38].

We have recollected the main theories of spin transport in this chapter for two main reasons. First, they give a landscape of the different approaches to magnetic multilayers. Then, they are conceptually related, as it will be shown in the following chapers. We shall see that CRMT is a particular case of RMT, which is itself derived from scattering matrix formalism. Besides, scattering matrix and NEGF formalism are equivalent (in the case of zero temperature and no electron-electron interactions), while CRMT is a generalization of VF theory to non collinear spin valves. There is a neat distinction between *fully quantum* theories (like scattering formalism or NEGF) that can treat purely quantum phenomena like tunneling and *semiclassical theories* (like VF theory), which describe Ohmic conductors and contain naturally the concepts of chemical potential and spin accumulation. In this sense, CRMT is a bridge between VF and quantum theories, since it is formulated in the language of scattering matrices, it takes into account Sharvin Resistance [93, 26] (a purely quantum phenomena), but apart from this is equivalent to VF for collinear spin valves (only Ohmic conductors can be described), and chemical potential can be naturally introduced in the theory. The different approaches and their connections are shown in FIG.(2.1)

2.2 Electronic transport through a multilayer

2.2.1 The Valet-Fert theory of spin transport

The Valet-Fert (VF) theory [97] provides a description of electronic transport in magnetic multilayers based on a diffusive equation, obtained starting from the Boltzmann equation. In the VF formulation, one considers a given current density j flowing along the x axis perpendicular to the plane of the

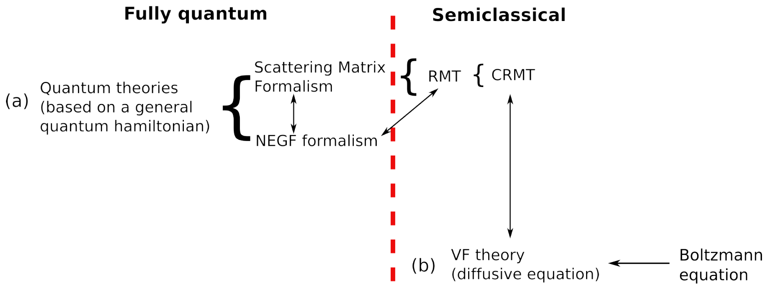

Figure 2.1: Schematic of the theories discussed in this work. (a) contains quantum theories for non collinear spin valves. Scattering and NEGF formalism (implemented using a Tight Binding (TB) Hamiltonian) belong to this family. RMT and CRMT are derived from the scattering approach. The VF theory for collinear spin valves belongs to a different ”family”, since it is based on a diffusive model derived from Boltzmann equation. The arrows represent the direct connections between different theories. For example, scattering formalism and TB model are equivalent, CRMT is a generalization of VF for non-collinear systems (in the collinear case they are equivalent, up to the Sharvin resistance [79] that is contained in CRMT, while in VF has to be added *a posteriori*). TB and RMT are equivalent only for Ohmic conductors. The figure is separated into two regions that divides purely quantum from semiclassical theories. RMT is semiclassical essentially because i) interference effects are averaged [103], and ii) exponential suppression of the conductance (tunnel effect) cannot be described. CRMT is obtained from a particular parametrization of RMT [79].

layers (CPP-Current Perpendicular to Plane geometry), and takes into account only configurations where the magnetizations of a given ferromagnetic layer is "up" or "down" along the z axis, taken as spin quantization axis. The theory describes the propagation of the current j_σ, when the spin σ is parallel ($\sigma =\uparrow$) or antiparallel ($\sigma =\downarrow$) to the local magnetization in a magnetic layer. The VF theory expresses the variation of the current in the x direction, as a function of the *electrochemical potential* $\bar{\mu}_\sigma$, defined as

$$\bar{\mu}_\sigma(x) = \mu_\sigma(x) - eV(x), \tag{2.1}$$

$\mu_\sigma(x)$ being the chemical potential for spin σ and $V(x)$ being the bias voltage applied to the conductor.

In all the layers composing our system we consider a single parabolic conduction band, where electrons have the same effective mass m and Fermi velocity v_F. Collisions of electrons with impurities and defects are supposed to take place both at interfaces between different materials and inside the bulk, and are responsible for the resistance of the system. The collision rates are described using two characteristic times: τ_σ, the mean time between two collisions that preserves the spin σ; and τ_{sf}, is the mean time between two collisions with spin flip. The inverse of these two times are related to the transition probability between two states with wave vectors $\vec{k}$ and $\vec{k}'$. Since the collisions are elastic, the norm of $\vec{k}$ and $\vec{k}'$ is preserved, and only the direction of the velocity is changed at each collision. Two lengths are associated to the characteristic times:

$$\begin{aligned} l_\sigma &= v_F(1/\tau_\sigma + 1/\tau_{sf})^{-1}, && (2.2) \\ l_\sigma^{sf} &= \left(\frac{1}{3}v_F l_\sigma \tau_{sf}\right)^{1/2} = \left(D_\sigma \tau_{sf}\right)^{1/2}, && (2.3) \end{aligned}$$

respectively the electron mean free path l_σ and the spin diffusion length l_σ^{sf} for spin σ. The quantity D_σ is the diffusion constant for spin σ. The mean free path represents the mean distance traveled by electrons between two successive collisions, while the spin diffusion length represents the mean distance at which an electron loses its spin due to spin orbit interaction, or through exchange scattering by paramagnetic moments present in the nonmagnetic layers [20]. The theory being at zero temperature, there are no other source of scattering.

If the spin diffusion length is much longer than the mean free path, the Boltzmann equation model reduces to the two *Valet-Fert equations*:

$$\begin{aligned} j_\sigma &= \frac{g_\sigma}{e}\frac{\partial \bar{\mu}_\sigma}{\partial z}, && (2.4) \\ \frac{\partial j_\sigma}{\partial z} &= \frac{g_\sigma}{e}\frac{\bar{\mu}_\sigma - \bar{\mu}_{-\sigma}}{l_\sigma^{sf2}}, && (2.5) \end{aligned}$$

that relate current density and electrochemical potential. The first equation is just the Ohm's law: the voltage drop is related to the current density j_σ through the conductivity g_σ, which is different for the two spin channels ↑ and ↓. The second equation is a sort of continuity equation: it states that, in steady state, the spin accumulation [98]

$$\mu = \frac{\mu_\uparrow - \mu_\downarrow}{eV} \tag{2.6}$$

due to the spin current divergences is balanced by spin flip processes. The spin dependent electrochemical potential can be written as $\bar{\mu}_\pm = \bar{\mu} \pm \Delta\mu$, where $\Delta\mu$ is the term related to the spin accumulation. $\Delta\mu$ is related to the out of equilibrium magnetization ΔM via

$$|\Delta\mu| = \frac{2\mu_0}{3n\mu_B}|\Delta M|, \tag{2.7}$$

where n is the electron density and μ_B is the Bohr magneton. $\Delta\mu$ satisfies the equation

$$\frac{\partial^2 \Delta\mu}{\partial z^2} = \frac{\Delta\mu}{l_{sf}^2} \tag{2.8}$$

where $1/l_{sf}^2 = (1/l_\uparrow^{sf})^2 + (1/l_\downarrow^{sf})^2$ is the average spin diffusion length. Eq. (2.8) describes the exponential decay of the spin accumulation as a function of the distance from an interface between materials with different magnetization. In the following, we will refer to l_{sf} as spin flip length.

The difference between the resistivity for ↑ and ↓ electrons predicted by Eq. (2.4), is described in a phenomenological way introducing a *bulk spin asymmetry coefficient* β as follows

$$\rho_{\uparrow/\downarrow} = 1/g_{\uparrow/\downarrow} = 2\rho_F^*[(1 \mp \beta)] \tag{2.9}$$

Here $\rho_{\uparrow/\downarrow}$ is the bulk resistivity for spin up (down). The greater is β, the bigger is the difference in resistivity for up and down spins. β itself is defined from the resistivity $\rho_{\uparrow/\downarrow}$ as

$$\beta = \frac{\rho_\downarrow - \rho_\uparrow}{\rho_\downarrow + \rho_\uparrow} \tag{2.10}$$

In a normal metal β vanishes, so that $\rho_\uparrow = \rho_\downarrow \equiv 2\rho_N^*$. In the same way, we introduce an *interfacial spin asymmetry coefficient* γ, that accounts for the resistivity of the interface between two materials:

$$r_{\uparrow/\downarrow} = 2r_b^*[(1 \mp \gamma)] \tag{2.11}$$

In this picture, interfaces are described as virtual materials with witdh d and given resistivity for up and down electrons, and spin diffusion length

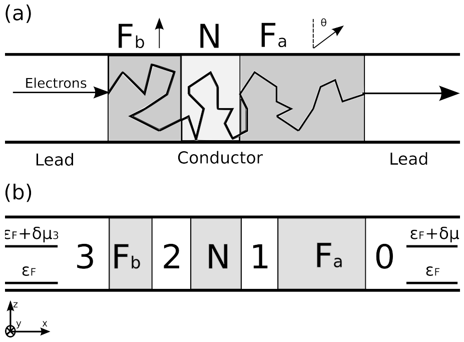

Figure 2.2: (a) Schematic of an electron that propagates from left to right leads, crossing a disordered region. The electronic spin is sensitive to the orientation of the magnetic moments inside the two ferromagnet F_a and F_b. The Hamiltonian of the system takes into account impurity scattering as well as spin dependent scattering. (b) Schematic of the system, where we have introduced fictitious leads. The slight difference on chemical potential of electrons near the Fermi energy creates a flow of electrons in the x direction.

l_{sf}^{eff}. This virtual material is taken to be infinitely thin $d \to 0$, while taking the ratio $\delta = d/l_{sf}^{eff}$ finite. the parameter From Eq.(2.11) one defines

$$\gamma = \frac{r_\uparrow - r_\downarrow}{r_\uparrow + r_\downarrow} \tag{2.12}$$

Much is known experimentally [110, 107] about $r^b_{\uparrow/\downarrow}$, but there are much less experimental data [73] for δ (and those are mainly for normal-normal interfaces). The parameters ρ^*, β, r^*, γ and l_{sf} define the VF theory for bulk and interfaces. This parametrization plays a key role in CRMT theory, and allows to obtain transport properties of a multilayer starting from a few easily accessible parameters.

2.2.2 General quantum Hamiltonian for conduction electrons

In this section we describe a completely different approach to spin transport. Let us consider a Ferromagnetic-Normal metal-Ferromagnetic (FNF) trilayer connected to two electrodes (leads) on the left and right, as shown in FIG.(2.2a). The electrodes are perfect conductors (normal or magnetic) connected to two electronic reservoirs with a given chemical potential. A difference of chemical potential between the leads creates a flux of electrons propagating inside the system. In our model we consider only electrons at the Fermi energy E_F, and neglect the complete band structure of the system. The two ferromagnetic layers are labeled F_a and F_b, while the normal metal spacer is labeled N. The magnetic moments of F_a and F_b point in the direction of unit vectors $\hat{\boldsymbol{m}}_a$ and $\hat{\boldsymbol{m}}_b$ respectively. The angle between $\hat{\boldsymbol{m}}_a$ and $\hat{\boldsymbol{m}}_b$ around the y axis is θ. We assume that $\hat{\boldsymbol{m}}_b$ points in the z direction, while the electron current flows in the x direction. As we will see, the fact that the current flows from left to right (x_+ direction) or from right to left (x_- direction) has a significant physical effect. It is convenient to add pieces of ideal lead (labeled 1, 2, 3 and 4) between the layers F_a, N and F_b.

We describe conduction electrons with the general Hamiltonian

$$\mathcal{H} = \int d\boldsymbol{r} \sum_{\alpha,\beta'=\uparrow,\downarrow} \phi^*_\alpha(\boldsymbol{r}) H_{\alpha\beta} \phi_\beta(\boldsymbol{r}) \tag{2.13}$$

where $\phi_\alpha(\boldsymbol{r})$ is the wave function associated to an electron with spin α. This wave function has spinor structure:

$$\phi(\boldsymbol{r}) = \begin{pmatrix} \phi_\uparrow(\boldsymbol{r}) \\ \phi\downarrow(\boldsymbol{r}) \end{pmatrix} \tag{2.14}$$

The 2 × 2 matrix

$$H = -\frac{\hbar^2}{2m} \bigtriangleup \otimes \mathbf{1} + V(\boldsymbol{r}) - E_F \tag{2.15}$$

contains kinetic, potential and Fermi energy. Here $\mathbf{1}$ is the 2×2 identity matrix, which accounts for the spinor structure of the wave function while the potential $V(\boldsymbol{r})$ represents spin-independent scattering from impurities, as well as spin-dependent effect of local exchange field and spin-flip effect due to spin orbit interaction inside the ferromagnets. In general the distribution of the impurities is different from sample to sample, so that $V(\boldsymbol{r})$ changes from one sample to the other. The 2 × 2 matrix $V(\boldsymbol{r})$ reads

$$V(\boldsymbol{r}) = e^{-i\sigma_y\theta(\boldsymbol{r})/2} \begin{pmatrix} V_{maj}(\boldsymbol{r}) & V_{sf}^{\uparrow\downarrow} \\ V_{sf}^{\downarrow\uparrow} & V_{min}(\boldsymbol{r}) \end{pmatrix} e^{i\sigma_y\theta(\boldsymbol{r})/2}. \tag{2.16}$$

here the diagonal terms account for majority (V_{maj}) and minority (V_{min}) electrons, while the off diagonal terms are responsible for spin flip. A particular choice of these matrix elements strongly depends on the model we use to describe the distribution of impurities inside the sample and on the material. the matrix $\exp[-i\sigma_y\theta(\boldsymbol{r})/2]$ rotates the potential from the external reference frame to the direction of the local exchange field. Outside the ferromagnet, $V_{maj} = V_{min}$. For the system under consideration, the angle $\theta(\boldsymbol{r}) = \theta$ inside F_a and zero elsewhere.

The physical meaning of this Hamiltonian is clear: a flux of electrons with a given spin and kinetic energy enters the system and feels a potential that depends on its spin. This potential is a source of scattering, responsible for the resistance and for spin flip phenomena. The angle θ has an influence on the transport properties of the system. In general, when a flux of electrons enters a ferromagnetic system, it has no spin polarization, i.e. the spins of the electrons are randomly distributed, so that the rotation around a given axis of the potential has no effect upon the flux. In order to have some spin dependent effect, the structure of Eq.(2.16) tells us that the flux of incident electrons has to be spin-polarized. Thus, in our system, for electrons propagating in the x_+ direction the layer F_b acts as a spin filter that polarizes the flux of electrons through exchange interaction, and align their spins with $\hat{\boldsymbol{m}}_b$. this makes the flux of electrons sensitive to the direction of $\hat{\boldsymbol{m}}_a$. Of course the direction of the current can be reversed. In this case the electrons are polarized along $\hat{\boldsymbol{m}}_a$, and become sensitive to the orientation of $\hat{\boldsymbol{m}}_b$.

The potential $V(\boldsymbol{r})$ vanishes in the leads. Nevertheless, we have to take into account another potential: the electrons are confined in the z and y directions, since they cannot propagate outside the system. This confining potential enters the Hamiltonian as boundary conditions of the wave functions in the transverse directions. In particular, in the leads a propagating mode is factorized as

$$\phi(\boldsymbol{r}) = \psi(y,z)\exp(\pm i k_x x), \tag{2.17}$$

where the wave vector of the transverse part $\psi(y,z)$ is quantized due to boundary conditions, while the longitudinal part is a free plane wave with k_x. Of course the leads are not *really* infinite, but since the system is almost one dimensional, and the length of the leads is much bigger than their transversal direction, they may be considered infinite without losing any generality or physical meaning. The factorization of the wave function in plane waves plays a key role in the scattering formalism, as it will be explained below.

2.2.3 Spin density, spin current and spin torque

Starting from the electronic wave functions, one defines spin density $\boldsymbol{\eta}(\boldsymbol{r})$ as:

$$\boldsymbol{\eta}(\boldsymbol{r}) = \frac{\hbar}{2}\sum_{\alpha\beta}\phi^{\dagger}_{\alpha}(\boldsymbol{r})\vec{\sigma}_{\alpha\beta}\phi_{\beta}(\boldsymbol{r}), \tag{2.18}$$

where $\vec{\sigma} = (\sigma_x, \sigma_y, \sigma_z)^T$ is the vector of Pauli matrices, and α, β are indexes in the spin space. The time evolution of spin density reads

$$\begin{aligned}\frac{\partial}{\partial t}\langle\boldsymbol{\eta}(\boldsymbol{r})\rangle &= \frac{i}{\hbar}\langle[H,\eta(\boldsymbol{r})]\rangle \\ &= -\vec{\nabla}\cdot\boldsymbol{j}(\boldsymbol{r}) + \frac{i}{2}\left\langle\phi^{\dagger}(\boldsymbol{r})[V(\boldsymbol{r}),\vec{\sigma}]\phi(\boldsymbol{r})\right\rangle, \end{aligned}\tag{2.19}$$

with the spin current density tensor $\boldsymbol{j}$ defined as

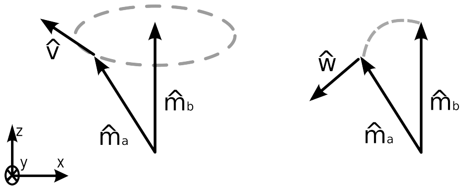

Figure 2.3: Schematic of the out of plane component of the torque $\tau_a^v \hat{\boldsymbol{v}}$ (left side) and the in plane component of the torque $\tau_a^v \hat{\boldsymbol{w}}$ (right side). The equilibrium exchange interaction only has an out of plane component, while the non equilibrium torque is mainly in plane.

$$\boldsymbol{j}(\boldsymbol{r}) = -\frac{i\hbar^2}{4m} \left\langle \phi^\dagger(\boldsymbol{r}) \vec{\nabla} \vec{\sigma} \phi(\boldsymbol{r}) - \vec{\nabla} \phi^\dagger(\boldsymbol{r}) \vec{\sigma} \phi(\boldsymbol{r}) \right\rangle . \tag{2.20}$$

Spin current density has one index in spin space and one index in real space, while $\langle ... \rangle$ stands for quantum mechanical expectation value. Eq. (2.19) shows that, unlike charge current, spin current is not conserved inside the ferromagnet. If a difference of chemical potential is set between the two reservoirs, a *nonequilibrium* spin current flows through the sample. The non conservation of the current implies that the currents in region 0 and 3 are different [see FIG. (2.2b)]. In absence of potential difference there is an *equilibrium* current: the spin current in both regions 0 and 3 vanishes, but the current in regions 1 and 2 is not necessary zero. The existence of a zero bias spin current and the resulting torques is a consequence of the itinerant-electron-mediated exchange interaction (also known as RKKY interaction, see Refs. [77, 111, 52, 46]) between two ferromagnetic films separated by a normal-metal spacer. The current induced torque follows from the non conservation of the nonequilibrium spin current, while the magnetic exchange interaction follows from the nonconservation of the equilibrium spin current between F_a and F_b [102]. The total torque $\boldsymbol{\tau}_a$ and $\boldsymbol{\tau}_b$ on the layers F_a and F_b is given by the spin current *absorbed* by the two ferromagnetic layers:

$$\begin{aligned} \boldsymbol{\tau}_a &= \boldsymbol{J}_0 - \boldsymbol{J}_1, \\ \boldsymbol{\tau}_b &= \boldsymbol{J}_2 - \boldsymbol{J}_3, \end{aligned} \tag{2.21}$$

where $\boldsymbol{J}_i$ is the total spin current that flows in the region $i = 1, 2, 3, 4$,

$$\boldsymbol{J}_i(x) = \frac{\hbar^2}{2m} \mathrm{Im} \int dydz \left\langle \phi^\dagger(x) \vec{\sigma} \frac{\partial}{\partial x} \phi(x) \right\rangle \tag{2.22}$$

The total torque takes into account the contribution from both equilibrium and nonequilibrium current.

Let us focus on the torque $\boldsymbol{\tau}_a$ acting on the magnetic moment of layer F_a [see FIG. (2.3)]. In absence of spin flip scattering, the spin current in the direction of $\hat{\boldsymbol{m}}_a$ is always conserved, so that there is no component of the torque in the direction of the magnetization. Even if spin flip is present, we consider materials where the magnetization is saturated, so that the effect of the spin torque in the direction of the magnetization is negligible, thus the only component of the torque we are interested in are those perpendicular to the $\hat{\boldsymbol{m}}_a$. In addition to the unit vector $\hat{\boldsymbol{m}}_a$ that points along the magnetization direction of F_a, we introduce the unit vectors $\hat{\boldsymbol{v}} = \hat{\boldsymbol{m}}_a \times \hat{\boldsymbol{m}}_b / |\hat{\boldsymbol{m}}_a \times \hat{\boldsymbol{m}}_b|$, which is normal to the plane spanned by $\hat{\boldsymbol{m}}_a$ and $\hat{\boldsymbol{m}}_b$, and $\hat{\boldsymbol{w}} = \hat{\boldsymbol{m}}_a \times \hat{\boldsymbol{v}}$, which lies in the plane spanned by $\hat{\boldsymbol{m}}_a$ and $\hat{\boldsymbol{m}}_b$ and is perpendicular to $\hat{\boldsymbol{m}}_a$. For the configuration of FIG. (2.3), $\hat{\boldsymbol{v}}$ is the unit vector in the y direction and the plane spanned by $\hat{\boldsymbol{m}}_a$ and $\hat{\boldsymbol{m}}_b$ is the xz plane.

Since the torque is perpendicular to the magnetization, $\boldsymbol{\tau}_a$ can be decomposed on the basis $(\hat{\boldsymbol{v}}, \hat{\boldsymbol{w}})$:

$$\boldsymbol{\tau}_a = (\boldsymbol{\tau}_a \cdot \hat{\boldsymbol{v}})\hat{\boldsymbol{v}} + (\boldsymbol{\tau}_a \cdot \hat{\boldsymbol{w}})\hat{\boldsymbol{w}} \tag{2.23}$$

for simplicity from here we set $\boldsymbol{\tau}_a \cdot \hat{\boldsymbol{v}} \equiv \tau_a^v$ and $\boldsymbol{\tau}_a \cdot \hat{\boldsymbol{w}} \equiv \tau_a^w$. The equilibrium torque can be calculated combining the commutator

$$[V(\boldsymbol{r}), \sigma_y] = -2i \frac{\partial V}{\partial \theta} \tag{2.24}$$

with Eq.(2.19), and it is simply given by the derivative of the energy $E = \langle H \rangle$ of the trilayer to the angle theta:

$$\boldsymbol{\tau}_a^v = \frac{\partial E}{\partial \theta}, \tag{2.25}$$

while a straightforward calculation gives, for the nonequilibrium torque:

$$\boldsymbol{\tau}_a^w = -\frac{1}{2} \int_{\boldsymbol{r} \in F_a} d\boldsymbol{r} \left\langle \phi^\dagger(\boldsymbol{r}) (V_{maj} - V_{min}) (\sigma \cdot \hat{\boldsymbol{v}}) \phi(\boldsymbol{r}) \right\rangle. \tag{2.26}$$

The in-plane torque τ_a^w, pushes $\hat{\boldsymbol{m}}_a$ towards or away from $\hat{\boldsymbol{m}}_b$. The equilibrium torque is simply given by

$$\boldsymbol{\tau}_a^{eq} = -\boldsymbol{J}_2 = -\boldsymbol{J}_3 = -\boldsymbol{\tau}_b. \tag{2.27}$$

This relation, combined with with the requirement that $\boldsymbol{\tau}_a$ and $\boldsymbol{\tau}_b$ are perpendicular respectively to $\hat{\boldsymbol{m}}_a$ and $\hat{\boldsymbol{m}}_b$, implies that, in equilibrium, the in-plane torque vanishes. The out-of-plane torque causes a precession of one magnetic moment around the other one. This is similar to the Larmor precession of the moments in a (possibly θ dependent) magnetic field. In the presence of dissipation, the system will relax to the lowest energy configuration, where the energy is minimal and the torque is zero (Eq.2.25).

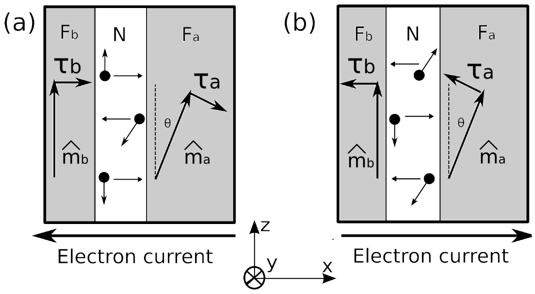

Figure 2.4: Schematic that shows the dependance of spin torque on the direction of the current. For electrons coming from the right, their spin is polarized along m_a, and a torque τ_a (respectively τ_b) acts on m_a (respectively m_a) as shown in fig. (a). When the direction of the current is reversed, the direction of the torque is reversed as well, as shown in fig. (b).

In the following we will consider only the nonequilibrium spin torque, since the role of equilibrium spin torque is negligible (the reason will become clear when we will discuss Random Matrix Theory).

The presence of two ferromagnetic layers has the effect of allowing for multiple scattering of the electrons between the two layers, which gives rise to an asymmetry of the torque with respect to the current direction. To see how this asymmetry arises, let us consider the FNF system shown in FIG.(2.4). When the current enters the sample from the right, electrons transmitted through F_a are polarized along $\hat{\boldsymbol{m}}_a$. The spin polarized flux of electrons impinges on F_b and exerts a torque on the moments of F_b so as to align $\hat{\boldsymbol{m}}_b$ with $\hat{\boldsymbol{m}}_a$. When electrons enter from the left, repeating the argument for F_b, we find that the spin of the electrons reflected from F_b are aligned antiparallel to $\hat{\boldsymbol{m}}_b$, and hence, in turn, exerts a torque on the moments of F_a trying to align $\hat{\boldsymbol{m}}_a$ antiparallel to $\hat{\boldsymbol{m}}_b$. Subsequent multiple reflections of electrons between F_a and F_b reduce the magnitude of the initial torques, but they do not eliminate or reverse them, since the elctron flux is reduced after each reflection.

If there were no other forces acting on the magnetization (anisotropy, shape effects...) the result would be a pinwheel motion with both moment rotating in the same direction. When the current is injected from the right, the direction of the torques are reversed: now the flow of electrons exerts a torque on F_a trying to align its moment parallel to $\hat{\boldsymbol{m}}_b$, while it exerts a torque on F_b that push the moment $\hat{\boldsymbol{m}}_b$ antiparallel to $\hat{\boldsymbol{m}}_a$.

2.3 Scattering matrix approach to electronic transport

2.3.1 Definition of scattering matrix

In the previous section we have written a Hamiltonian H [Eq.(2.15)] that describes what happens *inside* the conductor. In order to solve the problem of electron propagation we should in principle diagonalize the Shroedinger equation

$$\hat{H}\phi(\boldsymbol{r}) = E\phi(\boldsymbol{r}) \tag{2.28}$$

inside all the regions of the trilayer (F_a, N, F_b and the leads), a task that might be extremely complicated. Scattering matrix formalism, developed by R. Landauer, Y. Imry and M. Buttiker [19], offers an alternative view of the problem which provides a complete description of transport inside a coherent conductor at low frequency, temperature and voltages, under circumstances where electron-electron interactions can be neglected. In this view an electron propagates inside a perfect lead as a plane wave, enters the conductor, and is transmitted to another lead (or reflected back) with a certain probability amplitude. The formalism is apt to describe the transport through a conductor connected to an arbitrary number of leads. In this simple description there is no need to diagonalize the problem inside the conductor: the Hamiltonian simply determines the transmission and reflection probability for the electron entering the system from a lead. The theory to calculate these coefficient will be described in the next chapters. For the moment we consider the transmission and reflection coefficients as free parameters of the scattering formalism.

As we have seen in the previous section [Eq. (2.17)], the wave function ψ of an electron in a lead separates into a longitudinal and transverse part,

$$\psi_n^{\pm}(\boldsymbol{r}) = \Phi_n(y,z)\exp(\pm ik_n x). \tag{2.29}$$

Mode n has a real wave number $k_n > 0$ and a transverse wave function Φ_n. Due to the boundary conditions on Φ_n, the transverse wave vectors k_y and k_z are quantized. The integer $n = 1, ..., N_{ch}$ labels the propagating modes, also referred to as *scattering channels*. The normalization of the wave function is chosen such that it carries unit current.

We will first deal with spinless particles, the generalization to 1/2 spin electrons being straightforward. Let us consider the system depicted in FIG. (2.5). The "spinless electrons" propagating in lead 1 and 2 can be written on the basis of the ψ_n as follows:

$$\Psi_1(\boldsymbol{r}) = \sum_{n=1}^{N_{ch}} \left(a_n^+\psi_n^+(\boldsymbol{r}) + a_n^-\psi_n^-(\boldsymbol{r})\right), \tag{2.30}$$

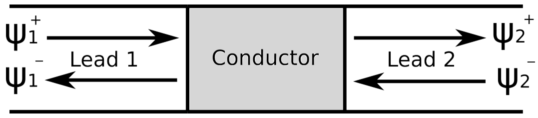

Figure 2.5: Cartoon representing plane waves that move inward and outward a conductor. The wavefunctions Ψ_1^{pm} and Ψ_2^{pm}, propagating in lead 1 and 2 correspondingly, are linear superpositions of the propagative modes. The conductor is represented with a scattering matrix S that relates incoming modes to outgoing modes.

$$\Psi_2(\boldsymbol{r}) = \sum_{n=1}^{N_{ch}} (b_n^- \psi_n^-(\boldsymbol{r}) + b_n^+ \psi_n^+(\boldsymbol{r})). \tag{2.31}$$

where the superscripts $(+,-)$ refers to waves propagating from left to right and from right to left correspindingly, while coefficients a_n and b_n refers respectively to lead 1 and 2. Thus, a wave incident on the disordered region is described by a vector of coefficients

$$c^{in} = (a_1^+, a_2^+, ...a_{N_{ch}}^+, b_1^-, b_2^-, ..., b_{N_{ch}}^-). \tag{2.32}$$

The first set of N_{ch} coefficients refers to the left lead and the second set of N_{ch} coefficients to the right lead. Similarly, the outgoing wave has vector of coefficients

$$c^{out} = (a_1^-, a_2^-, ...a_{N_{ch}}^-, b_1^+, b_2^+, ..., b_{N_{ch}}^+). \tag{2.33}$$

The scattering matrix S is a $2N_{ch} \times 2N_{ch}$ matrix which relates the two vectors,

$$c^{out} = Sc^{in}. \tag{2.34}$$

It has the block structure

$$S = \begin{pmatrix} r & t' \\ t & r' \end{pmatrix} \tag{2.35}$$

with $N_{ch} \times N_{ch}$ transmission matrices t and t' (transmission amplitudes from left to right and from right to left) and reflection matrices r and r' (reflection amplitudes from left to left and from right to right). In the case of spinless particles the coefficients of the scattering matrix are complex numbers. The generalization to 1/2 spin particles is done replacing each of the coefficients t_n, t'_n, r_n, r'_n of the n^{th} propagating mode with 2×2 matrices. This keeps track of the spinor structure of the wave functions propagating inside the leads, and associates to each spin up and down state a transmission and reflection

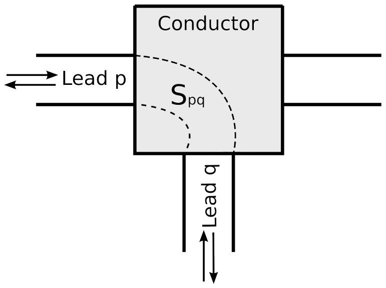

Figure 2.6: Scattering matrix that connects leads p and q in a multi-terminal device. In such a device, each pair of leads has its own scattering matrix that describe transport properties

amplitude. Taking into account the spin degree of freedom, S is a $4N_{ch} \times 4N_{ch}$ matrix, and each block described by Eq.(2.35) contains $2N_{ch}\times 2N_{ch}$ transmission and reflection matrices. So, in general, each coefficient of the scattering matrix relates different modes with arbitrary spin and it is thus specified by four indexes: two channel indexes (m, n) and two spin indexes (σ, σ'). In this way, scattering formalism properly describes spin dependent transport, where electrons can be transmitted or reflected preserving or changing their spin, according to the microscopic interactions that take place in the disordered region.

From scattering matrix one can calculate various transport properties of the system. In particular the conductance

$$G = \lim_{V\to 0}\frac{\bar{I}}{V} \tag{2.36}$$

defined as the ratio of the time average electrical current $\bar{I}$ over the voltage difference V between the two electron reservoirs in the limit of vanishingly small voltage. At zero temperature, the conductance is given by the Landauer formula [19, 26]

$$G = \frac{2e^2}{h}\mathrm{Tr}(tt^\dagger) \tag{2.37}$$

where t is the transmission matrix of the system, and the trace has to be taken in the channel and spin spaces. Eq. (2.37) has a simple interpretation as sum over the transmission probability of all the modes entering the system. The prefactor $G_0 = 2e^2/h$ is the quantum of conductance, and the factor 2 is due to the twofold spin degeneracy.

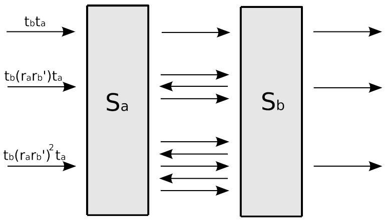

Figure 2.7: Cartoon representing the multiple reflections of a particle crossing two systems connected in series, described by the scattering matrices S_a and S_b.

2.3.2 Scattering matrix for a multi-terminal device

The same formalism can be adapted to a system with many terminal, by adding a pair of indexes (p, q) to the transmission and reflection coefficients, that label the terminals considered. We can see a multi-terminal device like a system endowed with more than one scattering matrix, each matrix describing the transport between leads p and q [FIG.(2.6)]. In general, a scattering matrix S_{pq} relates the modes c_{pq}^{in} that enter the system from leads p and q, to the modes c_{pq}^{out} that comes out from the system through these leads. Eqs. (2.34) and (2.34) then become

$$c_{pq}^{out} = S_{pq} c_{pq}^{in}, \tag{2.38}$$

$$S_{pq} = \begin{pmatrix} r_{pq} & t'_{pq} \\ t_{pq} & r'_{pq} \end{pmatrix}. \tag{2.39}$$

The Landauer formula can be simply generalized to a multi-terminal device. At zero temperature, current I_p and voltages V_p and V_q at leads p and q are related via the conductance G_{pq}:

$$I_p = \sum_q G_{pq}(V_p - V_q), \tag{2.40}$$

where the conductance now reads

$$G_{pq} = \frac{2e^2}{h} \mathrm{Tr} t_{pq} t_{pq}^{\dagger}. \tag{2.41}$$

In general we refer to the transmission probability $\bar{T}_{pq} = \mathrm{Tr} t_{pq} t_{pq}^{\dagger}$ between leads p and q as transmission function. The reader can find a comprehensive description of scattering matrix formalism in Ref.[26]

2.3.3 "Ohm's law" for quantum conductors

Let us consider two conductors a and b, described by the scattering matrices S_a and S_b, and connected in series. Classical electromagnetism tells us that the resistance of the composed system is $R_{a+b} = R_a + R_b$. When two quantum conductors a and b are connected in series, the scattering matrix of the total system $a+b$ has to be calculated adding all the possible processes leading to the transmission of the electron through the two systems [FIG.(2.7]. The transmission matrix t_{a+b} of the two conductors a and b connected in series can be written as a sum

$$t_{a+b} = t_b t_a + t_b(r_a r'_b)t_a + t_b(r_a r'_b)(r_a r'_b)t_a + ..., \tag{2.42}$$

that includes the direct process where the electron is transmitted by a and b $(t_b t_a)$, the process where the electron is transmitted by a, reflected by b and a and transmitted by b $(t_b(r_a r'_b)t_a)$ and so on. This series can be summed as:

$$t_{a+b} = t_b[1 - r_a r'_b]^{-1} t_a \tag{2.43}$$

A similar procedure gives the other transmission and reflection coefficients:

$$\begin{aligned} r_{a+b} &= r_b + t_b[1 - r_a r'_b]^{-1} r_a t'_b && (2.44)\\ t'_{a+b} &= t'_a[1 - r_b r'_a]^{-1} t_b && (2.45)\\ r'_{a+b} &= r'_b + t_b[1 - r_b r'_a]^{-1} r'_a r'_b && (2.46)\end{aligned}$$

These rules describe how transmission and reflection *amplitudes* (i.e. complex numbers which take into account the phase shift accumulated by the electron crossing the conductor) have to be summed when two or more conductors are put in series. In Sec. (2.4.1) we shall see how to apply the sum rule to transmission and reflection *probabilities.* This gives an equivalent of the Ohm's low at quantum level. The sum rule plays a key role in the theory of transport that we shall describe in the following two chapters.

2.3.4 Application of scattering matrix formalism to the study of an FNF trilayer

In this section we show how to apply scattering matrix formalism to the study of spin transport inside an FNF trilayer. Although we shall restrict our formulas to this simple case, this method is applicable for an arbitrary array of alternating magnetic-nonmagnetic layers. In this section we follow mainly Ref.[103]. FIG. (2.8) shows the FNF junction where fictitious perfect leads (labeled 0,1,2 and 3) have been added in between the layers F and N and between the F layers and the electron reservoirs on either sides of the sample. The introduction of these leads allows for a description of the

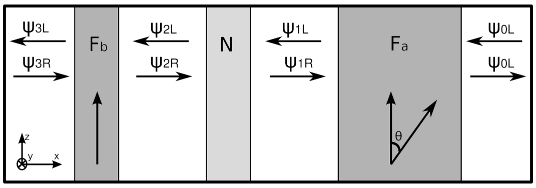

Figure 2.8: Schematic of the setup used for the definition of the scattering matrices in the layers F_a, F_b and N. Amplitude of left and right moving propagating waves are defined in fictitious ideal leads 0,1,2 and 3 between the layers and between the layers and the reservoirs.

system using scattering matrices. Inside the leads, the transverse degrees of freedom are quantized [see Eq. (2.29)], giving N_{ch} propagating modes at the Fermi level, where $N_{ch} \approx A/\lambda_F^2$, A being the cross section area of the junction and λ_F the Fermi wave length. Expanding the electronic wave functions in these modes, we can describe the system in terms of the projection $\Psi_{i,L/R}$ of the wave function onto the left (right) going modes in region i. The $\Psi_{i,L/R}$ are $2N_{ch}$-component vectors, counting the N_{ch} transverse modes and spin. Normalization is done in such a way that each mode carries unit current. The amplitudes of the wave function into two neighbouring ideal leads are connected through the scattering matrices S_b, S_a and S_N, that relate outgoing modes and ingoing modes at the layers b, N and a as follows:

$$\begin{pmatrix} \Psi_{3L} \\ \Psi_{2R} \end{pmatrix} = S_b \begin{pmatrix} \Psi_{3R} \\ \Psi_{2L} \end{pmatrix}, \tag{2.47}$$

$$\begin{pmatrix} \Psi_{1L} \\ \Psi_{0R} \end{pmatrix} = S_a \begin{pmatrix} \Psi_{1R} \\ \Psi_{0L} \end{pmatrix}, \tag{2.48}$$

$$\begin{pmatrix} \Psi_{2L} \\ \Psi_{1R} \end{pmatrix} = S_N \begin{pmatrix} \Psi_{2R} \\ \Psi_{1L} \end{pmatrix}. \tag{2.49}$$

We decompose these matrices into $2N_{ch} \times 2N_{ch}$ transmission and reflection matrices:

$$S_b = \begin{pmatrix} r_b & t'_b \\ t_b & r'_b \end{pmatrix}, \tag{2.50}$$

With the same decomposition for S_a and S_N. Due to the spin degree of freedom, the reflection and transmission matrices are expressed in terms of four $N_{ch} \times N_{ch}$ blocks:

$$r_b = \begin{pmatrix} r_{b\uparrow\uparrow} & t'_{b\uparrow\downarrow} \\ t_{b\downarrow\uparrow} & r'_{b\downarrow\downarrow} \end{pmatrix} \tag{2.51}$$

where the subscripts ↑, ↓ refers to spin up and down in the z-axis basis. The scattering matrix of the magnetic layers depends on the angle θ the moments may have with the z axis. The matrix $S_a(\theta)$ is related to $S_a(\theta = 0)$ through a rotation in spin space. For example, $r_a(\theta)$ reads

$$r_a(\theta) = R_\theta r_a(0) R_{-\theta}, \tag{2.52}$$

where

$$R_\theta = \begin{pmatrix} \cos\frac{\theta}{2} & -\sin\frac{\theta}{2} \\ \sin\frac{\theta}{2} & \cos\frac{\theta}{2} \end{pmatrix} \otimes 1_{Nch} \tag{2.53}$$

is the matrix that realizes the rotation in spin space around the y axis for each channel. Inside the normal layer the transmission and reflection subblocks are diagonal, so that a non magnetic layer does not affect the spin state. To calculate the net spin current deposited into each magnetic layer, we need to keep track of the amplitudes in the different regions of the system. Therefore, we define $2N_{ch} \times 2N_{ch}$ matrices $\Gamma_i^{L/R}$ and $\Lambda_i^{L/R}$ so that we may express all the $\Psi_i^{L/R}$ as a function of the amplitudes incident from the two electrodes (region 0 and 3):

$$\begin{pmatrix} \Psi_{iL} \\ \Psi_{iR} \end{pmatrix} = \begin{pmatrix} \Gamma_{iL} & \Lambda_{iL} \\ \Gamma_{iR} & \Lambda_{iR} \end{pmatrix} \begin{pmatrix} \Psi_{0L} \\ \Psi_{3R} \end{pmatrix} \tag{2.54}$$

with the convention that $\Gamma_{0L} = \Lambda_{3R} = 1$ and $\Gamma_{3R} = \Lambda_{0L} = 0$. In order to calculate the torque exercised on layer F_b for a current entering from the left, we need to calculate the matrix Γ_{2L}. To simplify the notation from here we write $\Omega \equiv \Gamma_{2L}$. The matrix Ω relates Ψ_{2L} to the incoming amplitudes Ψ_{0L} coming from the right. To calculate it, we set $\Psi_{3R} = 0$ and, using Eqs. (2.47-2.49) we get the equations

$$\begin{aligned} \Psi_{1L} &= t'_a \Psi_{0L} + r_a \Psi_{1R}, \\ \Psi_{1R} &= t_n \Psi_{2R} + r'_n \Psi_{1L}, \\ \Psi_{2L} &= r_n \Psi_{2R} + t'_n \Psi_{1L}, \\ \Psi_{2R} &= r'_b \Psi_{2L}, \\ \Psi_{3L} &= t'_b \Psi_{2L}, \end{aligned} \tag{2.55}$$

from which we obtain

$$\Omega = \frac{1}{1 - r_n r'_b} t'_n \frac{1}{1 - r_a t_n r'_b (1 - r_n r'_b)^{-1} t'_n - r_a r'_n} t'_a. \tag{2.56}$$

The modes inside the reservoirs are at Fermi level ε_F. When the chemical potential in the left (right) reservoir is sligthly increased by $\delta\mu_3$ ($\delta\mu_0$), a non equilibrium spin current flows. For each region $i = 0, 1, 2, 3$ the spin current

$\boldsymbol{J}_i$ is the difference between left going and right going contribution. From Eqs. (2.22) and (2.54) one gets:

$$\frac{\partial \boldsymbol{J}_i}{\partial \mu_0} = \frac{1}{4\pi}\mathrm{Re}[\mathrm{Tr}_{2N_{ch}}\vec{\sigma}\Gamma_{iR}\Gamma^{\dagger}_{iR} - \mathrm{Tr}_{2N_{ch}}\vec{\sigma}\Gamma_{iL}\Gamma^{\dagger}_{iL}] \tag{2.57}$$

$$,\frac{\partial \boldsymbol{J}_i}{\partial \mu_3} = \frac{1}{4\pi}\mathrm{Re}[\mathrm{Tr}_{2N_{ch}}\vec{\sigma}\Lambda_{iR}\Lambda^{\dagger}_{iR} - \mathrm{Tr}_{2N_{ch}}\vec{\sigma}\Lambda_{iL}\Lambda^{\dagger}_{iL}], \tag{2.58}$$

where the trace is taken on the channel space. If the spin current inside regions 2 and 3 is different, then angular momentum has been deposited in the layer F_b. This creates a torque $\boldsymbol{\tau}_b$ on the magnetic moments of the ferromagnet

$$\boldsymbol{\tau}_b = \boldsymbol{J}_3 - \boldsymbol{J}_2. \tag{2.59}$$

Setting $\delta\mu_0 = -eV_0$ one has the following expression for spin torque:

$$\frac{\partial \boldsymbol{\tau}_b}{\partial V_0} = -\frac{4}{4\pi}\mathrm{Re}\mathrm{Tr}_{2N_{ch}}[\boldsymbol{\Sigma}\Omega\Omega^{\dagger}] \tag{2.60}$$

where the matrix $\boldsymbol{\Sigma}$ reads

$$\boldsymbol{\Sigma} = \vec{\sigma} - t'^{\dagger}_b\vec{\sigma}t'_b - r'^{\dagger}_b\vec{\sigma}r'_b. \tag{2.61}$$

This expression contains both non equilibrium and equilibrium spin torque [Eqs.(2.59) and (2.60)]. Since the former is typically a factor $1/N_{ch}$ smaller and vanishes upon ensemble averaging [8, 103]), it will be negelected in our calculations based on random matrix theory (see next section). For the non equilibrium torque one has $\partial\boldsymbol{\tau}_b/\partial V_0 = -\partial\boldsymbol{\tau}_b/\partial V_3$, up to a correction of order $1/N_{ch}$.

2.4 Random matrix theory

2.4.1 Sum of amplitudes and sum of probabilities

In a multilayer, scattering happens inside the bulk , and at the interfaces between different materials (due to the potential barrier felt by electrons at the crossing between materials with different properties). Each subpart of the system has its own scattering matrix, and it is important to be able to combine several parts to obtain the global $\hat{S}$ matrix [Eqs.(2.43) and (2.44)]. This is particularly important when one is interested in calculating the spin torque, as one also needs to calculate the spin current flowing *inside* the system and not only near the electrodes. On the other hand, the sum of scattering matrices of subpart of a system gives reflection and transmission *amplitudes* for electron flowing through it, while the physical quantities are obtained from transmission and reflection *probabilities.* In this section we show how to sum transmission/reflection probabilities of subparts of the system to obtain the properties of the system as a whole. This procedure, which gives an equivalent of the Ohm's law at quantum level, is the cornerstone of the transport models developed in this work.

Let us consider the sum rule for a spinless particle crossing two conductors a and b connected in series, described by the scattering matrices S_a and S_b. The generalization to 1/2 spin electrons is straightforward and consists simply in adding an index for the spin degree of freedom to the element of scattering matrices. Let us suppose that the these matrices are diagonal in channel space, so that there is no mixing of channels in the propagation of particles. According to Eq. (2.43) the transmission amplitude t_{a+b} for the two conductors in series is

$$t_{a+b} = t_b \frac{1}{1 - |r_a||r_b|e^{i\phi}} t_a \tag{2.62}$$

where whe have written separately the modulus of the coefficients r_a and r_b and their phase $e^{i\phi}$. The transmission probability T_{a+b} of the two systems in series is given by $|t_{a+b}|^2$. If the conductor has many open channels, the phase $e^{i\phi}$ varies randomly from channel to channel, so that the average over the channels is done averaging on the angle ϕ:

$$T_{a+b} = \frac{1}{2\pi} \int_0^{2\pi} |t_b|^2 |t_a|^2 \frac{1}{1 - r_a r_b e^{i\phi}} \frac{1}{1 - r_b^* r_b^* e^{-i\phi}} d\phi \tag{2.63}$$

This integral can be calculated performing the substitution $z = e^{i\phi}$, and $dz = ie^{i\phi} d\phi \rightarrow d\phi = -i\frac{dz}{z}$:

$$T_{a+b} = \frac{-i}{2\pi} |t_a|^2 |t_b|^2 \int_C \frac{1}{1 - r_a r_b z} \frac{1}{1 - \frac{r_a r_b}{z}} \frac{dz}{z}, \tag{2.64}$$

where C is the circle with unit radius. A straightforward calculation with the residual theorem gives:

$$T_{a+b} = T_b \frac{1}{1 - R_a R_b} T_a, \tag{2.65}$$

where we have set $|t_i|^2 = T_i$ and $|r_i|^2 = R_i$, $i = a, b$. Thus, in this simple spinless case, the sum rule for the transmission probabilities is the same as the sum rule for the transmission amplitudes, and is obtained simply substituting the transmission and reflection coefficients with their square modulus. For the conservation of the probability one has $T_i + R_i = 1$, thus Eq.(2.66) takes the form

$$\frac{1}{T_{a+b}} = \frac{1}{T_a} + \frac{1}{T_b} - 1 \tag{2.66}$$

The resistance of each block, expressed in Ohms, is obtained multiplying $1/T_i$ by the *Sharvin resistance* [93, 26] $R_{\mathrm{sh}} = h/(e^2 N_{ch})$:

$$R_{a+b} = R_a + R_b - \mathcal{R}_{Sh} \tag{2.67}$$

When more than two conductors are put in series, the Sharvin resistance has to be added only once, independently of the number of conductors that have to be added. Indeed, the Sharvin resistance is a *contact resistance*, *i.e.* as an additional resistance given by the fact that electrons reservoirs, which contain number of channels that might be considered infinite, are connected to a conductor with a finite number of channels. Thus, a perfect conductor with does not have zero resistance, but a resistance of h/e^2 per propagative channel. In macroscopic conductors the number of channels is huge, and the Sharvin resistance is negligible. However, in mesoscopic its effect has to be taken into account.

Indeed, Eq.(2.66) holds in general, and the sum rule of ”probability matrices” is *exactly the same* as the sum rule of scattering matrices. To each scattering matrix s containing (t, t', r, r'), we associate a ”hat matrix”, $(\hat{t}, \hat{t}', \hat{r}, \hat{r}')$, which represents the transmission/reflection probability for an electron crossing the system. The sum rule for hat matrices is exactly the same as the sum rule for scattering matrix.

$$\begin{aligned}
\hat{t}_{a+b} &= \hat{t}_b[\hat{1} - \hat{r}_a\hat{r}'_b]^{-1}\hat{t}_a \\
\hat{r}_{a+b} &= \hat{r}_b + \hat{t}_b[\hat{1} - \hat{r}_a\hat{r}'_b]^{-1}\hat{r}_a\hat{t}'_b \\
\hat{t}'_{a+b} &= \hat{t}'_a[\hat{1} - \hat{r}_a\hat{r}'_b]^{-1}\hat{t}_b \\
\hat{r}_{a+b} &= \hat{r}'_b + \hat{t}_b[\hat{1} - \hat{r}_b\hat{r}'_a]^{-1}\hat{r}'_a\hat{t}'_b
\end{aligned} \tag{2.68}$$

This substitution of amplitudes with probabilities and of the whole system with a sum of simpler subblocks is the leading idea of the *multiscaleapproach* that will be described in chapters 3 and 4: a given system can be decomposed in subblocks, where transport properties are computed using the most convenient approach (semiclassical or fully quantum). When one has obtained the hat matrices of each subblock, one can sum them using Eq.(2.68) to in order to obtain the hat matrix of the system as a whole.

2.4.2 Scattering matrices and ”hat” matrices

In the previous section we have found an addition law for probability ”hat matrices” in a general way, without making any assumption about the structure of those matrices. In this section, we shall give a precise definition of hat matrices and their relation with quantum transport.

Random matrix theory (RMT) treats large matrices whose elements are randomly distributed. Once the probability distribution of the matrices has been chosen, one can calculate the correlation functions of eigenvalues and eigenvectors. Different physical properties can be related to these correlation functions. RMT was developed by Dyson, Wigner, Mehta and Gaudin

[67], to understand the statistics on energy levels inside heavy nuclei. More recently RMT has been applied to chaotic systems [12] and quantum transport [1, 8, 103]. In this section we shall see how to apply RMT to spin transport.

According to Eq.(2.60), the torque on the magnetic moments of the two layers F_a and F_b not only depends on the scattering matrices S_a and S_b of these layers, but also on the scattering matrix S_n of the normal layer in between. If the normal layer is disordered, spin torque depends on the location of the impurities, while if it is ballistic, spin torque depends sensitively on the phase shift accumulated in N. In general, sample to sample fluctuations of the torque are a factor $1/N_{ch}$ smaller than the average [8]. N_{ch} is large (typically $N_{ch}{\approx}10^3 - 10^5$), the torque is well characterized by its average.

Inside a single system with many channels, the transmission and reflection coefficients vary randomly from channel to channel. The scattering matrix can be therefore considered as a matrix whose elements are *randomly distributed.* In particular, the scattering matrix of the normal layer can be written using the polar decomposition [68, 66]

$$S_n = \left(\begin{array}{cc} U & 0 \\ 0 & V' \end{array} \right) \left(\begin{array}{cc} \sqrt{1-T} & i\sqrt{T} \\ i\sqrt{T} & \sqrt{1-T} \end{array} \right) \left(\begin{array}{cc} U' & 0 \\ 0 & V \end{array} \right), \tag{2.69}$$

Where U, V, U' and V' are $2N_{ch} \times 2N_{ch}$ unitary matrices and T is a diagonal matrix containing the eigenvalues of $t_n t_n^\dagger$. Since S_n is diagonal in spin space, U, U', V and V' are block diagonal:

$$U = \left(\begin{array}{cc} u & 0 \\ 0 & u \end{array} \right) \tag{2.70}$$

with similar definitions for U', V and V'. According to the isotropic approximation [8], these matrices are uniformly distributed in the group $U(N_{ch})$. Thus, the central matrix in Eq.(2.69) contains the transmission properties of the layer, while the outer blocks mix the modes in an ergodic way: an electron entering the system in a given mode will leave it with a certain probability and an arbitrary mode, and gets a random phase in the process.

We shall calculate the *average* spin torque, obtained averaging over T and the unitary matrices. this averaging can be done in a general way according to the following prescription: to a given $2N_{ch} \times 2N_{ch}$ matrix a one assigns a 4×4 "hat" matrix $\hat{a}$ with elements

$$A_{\eta\lambda\mu\nu} = \frac{1}{N_{ch}} \mathrm{Tr}_{N_{ch}} [a_{\eta\lambda} a^\dagger_{\mu\nu}], \tag{2.71}$$

where we have implied channel indices in matrices $a, a^\dagger$, each of the index η, λ, μ, ν is a spin index $\uparrow / \downarrow$, and the trace has to be taken in each of the $N_{ch} \times N_{ch}$ blocks. A general property of this average is that the fluctuations are a factor of order N_{ch} smaller than the average. This justifies the fact that we have neglected the equilibrium spin torque, which is a factor N_{ch} smaller than the non equilibrium torque. Eq.(2.71) *in extenso* reads

$$\hat{a} = \frac{1}{N_{ch}} \mathrm{Tr}_{Nch} \begin{pmatrix} A_{\uparrow\uparrow}A^{\dagger}_{\uparrow\uparrow} & A_{\uparrow\uparrow}A^{\dagger}_{\uparrow\downarrow} & A_{\uparrow\downarrow}A^{\dagger}_{\uparrow\uparrow} & A_{\uparrow\downarrow}A^{\dagger}_{\uparrow\downarrow} \\ A_{\uparrow\uparrow}A^{\dagger}_{\downarrow\uparrow} & A_{\uparrow\uparrow}A^{\dagger}_{\downarrow\downarrow} & A_{\uparrow\downarrow}A^{\dagger}_{\downarrow\uparrow} & A_{\uparrow\downarrow}A^{\dagger}_{\downarrow\downarrow} \\ A_{\downarrow\uparrow}A^{\dagger}_{\uparrow\uparrow} & A_{\downarrow\uparrow}A^{\dagger}_{\uparrow\downarrow} & A_{\downarrow\downarrow}A^{\dagger}_{\uparrow\uparrow} & A_{\downarrow\downarrow}A^{\dagger}_{\uparrow\downarrow} \\ A_{\downarrow\uparrow}A^{\dagger}_{\downarrow\uparrow} & A_{\downarrow\uparrow}A^{\dagger}_{\downarrow\downarrow} & A_{\downarrow\downarrow}A^{\dagger}_{\downarrow\uparrow} & A_{\downarrow\downarrow}A^{\dagger}_{\downarrow\downarrow} \end{pmatrix}, \tag{2.72}$$

With the prescription Eq.(2.71) one can associate to a given scattering matrix S defined in Eq.(2.35), the hat matrix

$$\hat{S} = \begin{pmatrix} \hat{r} & \hat{t}' \\ \hat{t} & \hat{r}' \end{pmatrix} \tag{2.73}$$

where each element is a 4×4 hat matrix that accounts for transmission and reflection trough a given system. To get an insight on the physics described with this formalism, let's focus on the transmission matrix $\hat{t}$. This matrix reads

$$\hat{t} = \begin{pmatrix} T_{\uparrow\uparrow\uparrow\uparrow} & T_{\uparrow\uparrow\uparrow\downarrow} & T_{\uparrow\downarrow\uparrow\uparrow} & T_{\uparrow\downarrow\uparrow\downarrow} \\ T_{\uparrow\uparrow\downarrow\uparrow} & T_{\uparrow\uparrow\downarrow\downarrow} & T_{\uparrow\downarrow\downarrow\uparrow} & T_{\uparrow\downarrow\downarrow\downarrow} \\ T_{\downarrow\uparrow\uparrow\uparrow} & T_{\downarrow\uparrow\uparrow\downarrow} & T_{\downarrow\downarrow\uparrow\uparrow} & T_{\downarrow\downarrow\uparrow\downarrow} \\ T_{\downarrow\uparrow\downarrow\uparrow} & T_{\downarrow\uparrow\downarrow\downarrow} & T_{\downarrow\downarrow\downarrow\uparrow} & T_{\downarrow\downarrow\downarrow\downarrow} \end{pmatrix}, \tag{2.74}$$

The elements $T_{\uparrow\uparrow\uparrow\uparrow}$ and $T_{\downarrow\downarrow\downarrow\downarrow}$ are real numbers that represent the transmission probabilities for an electron with spin parallel (up) and antiparallel (down) to the magnetization of the layer F_b, while $T_{\uparrow\downarrow\uparrow\downarrow}$ and $T_{\downarrow\uparrow\downarrow\uparrow}$ represents the probability for an electron to be transmitted flipping its spin (for an electron with spin up to be transmitted with spin down and vice versa).

The terms on the diagonal $T_{\uparrow\uparrow\downarrow\downarrow}$ and $T_{\downarrow\downarrow\uparrow\uparrow} = (T_{\uparrow\uparrow\downarrow\downarrow})^*$, called *mixing transmissions* and denoted T_{mx}, are complex numbers. In a magnetic material T_{mx} measures how much a spin transverse to the magnetic layer is likely to be transmitted. Due to the large number of modes the average T_{mx} decays rapidly with the size of the ferromagnet. Thus this terms are small in magnetic systems, but they play a role when the magnetic moment of the electrons and the magnetization of the layer are not aligned, since they are responsible for the spin torque, as it will be shown below. To simplify the notation, from here we set

$$\begin{aligned} T_{\uparrow\uparrow\uparrow\uparrow} &\equiv T_{\uparrow\uparrow} \\ T_{\downarrow\downarrow\downarrow\downarrow} &\equiv T_{\downarrow\downarrow} \\ T_{\uparrow\downarrow\uparrow\downarrow} &\equiv T_{\uparrow\downarrow} \\ T_{\downarrow\uparrow\downarrow\uparrow} &\equiv T_{\downarrow\uparrow} \end{aligned} \tag{2.75}$$

with this notation, Eq.(2.74) can be written in the more compact form

$$\hat{t} = \begin{pmatrix} T_{\uparrow\uparrow} & \cdot & \cdot & T_{\uparrow\downarrow} \\ \cdot & T_{\mathrm{mx}} & \cdot & \cdot \\ \cdot & \cdot & T^*_{\mathrm{mx}} & \cdot \\ T_{\downarrow\uparrow} & \cdot & \cdot & T_{\downarrow\downarrow} \end{pmatrix} \tag{2.76}$$

This matrix contains all the terms necessary to describe transport our system (the other terms represented by dots do not have any physical meaning in our description). As a further simplification, we define

$$\begin{aligned} T_\uparrow &= T_{\uparrow\uparrow} + T_{\downarrow\uparrow} \\ T_\downarrow &= T_{\downarrow\downarrow} + T_{\uparrow\downarrow} \end{aligned} \tag{2.77}$$

The coefficient $T_\uparrow$ represents the probability for an electron injected with spin up or down to be transmitted with spin up. It is the sum of two processes: the process when an electron enters with spin up and its spin is unchanged ($T_{\uparrow\uparrow}$), and the process where an electron enters with spin down and undergoes a spin flip ($T_{\downarrow\uparrow}$). In the same way, the coefficient $T_\downarrow$ is the probability for an electron to be transmitted with spin down. The same notation as Eqs.(2.75-2.76-2.77) is used for reflection hat matrices.

From Eq.(2.75,) one can write the conductance G of the system as

$$\langle G \rangle = \frac{N_{ch} e^2}{h} \left(T_{\uparrow\uparrow} + T_{\uparrow\downarrow} + T_{\downarrow\uparrow} + T_{\downarrow\downarrow} \right). \tag{2.78}$$

This formulation relates the conductance to the probabilities for different processes (spin flip and spin preserving) through which transmission may occur, and it corresponds to the Landauer formula [Eq.(2.37)], where $tt^\dagger$ has been substituted with the transmission probability averaged over the propagative channels. Using the definitions of Eq.(2.75) we can write the spin-polarization of the current as

$$P_I^\sigma = \frac{T_{\uparrow\sigma} - T_{\downarrow\sigma}}{T_{\uparrow\sigma} + T_{\downarrow\sigma}}. \tag{2.79}$$

Notice that in the averaging process one considers *only* the propagative channels, so that exponential suppression of the conductance is not taken into account. This means that the theory is suitable for Ohmic conductors, while tunnelling phenomena cannot be described within this formalism.

So far, the coefficients of hat matrices appear as free parameters of the theory. In chapters 4 and 5 we shall describe two different procedures to obtain these coefficients.

The Sharvin resistance relates transmission probabilities to the resistance expressed in Ohms. In particular, the *intrinisic* total resistance (*i.e.* the resistance of the conductor minus the Sharvin resistance) R_I^σ for spin σ of a conductor is

$$R_I^\sigma = \mathcal{R}_{sh}\left(\frac{1}{T_{\uparrow\sigma} + T_{\downarrow\sigma}} - 1\right). \tag{2.80}$$

This relation takes into account both the transmission probability without spin flip ($T_{\sigma\sigma}$) and the transmission with spin flip ($T_{\sigma\sigma'}$). Eq.(2.67) gives a prediction which is in contrast with the Ohm's law, according to which the resistance of two conductors connected in series should sum up *exactly*. As the size of the conductor increases, the number of channels grows and the Sharvin resistance quickly goes to zero, so that in the classical limit the Ohm's law is recovered.

2.4.3 Application to the FNF trilayer: comparison with the scattering matrix formalism

In this section we apply RMT to the description of the FNF multilayer treated in Sec.(2.3.4) This allows to see the analogy between scattering matrix formalism and RMT, and to define spin torque using hat matrices. We suppose that the trilayer is described by the hat matrices $\hat{S}_a$, $\hat{S}_N$ and $\hat{S}_b$. In particular, the hat matrices of the normal layer read

$$\hat{t}_n = \frac{g_n}{N_{ch}} 1_4, \tag{2.81}$$

$$\hat{r}_n = \left(1 - \frac{g_n}{N_{ch}}\right) 1_4, \tag{2.82}$$

where g_n is the conductance of the normal layer and 1_4 is the 4×4 identity matrix. Proceeding in the same way as in Sec. (2.3.4), one can define the matrix

$$\hat{\Omega} = \frac{1}{1 - \hat{r}_n \hat{r}'_b} \hat{t}'_n \frac{1}{1 - \hat{r}_a \hat{t}_n \hat{r}'_b (1 - \hat{r}_n \hat{r}'_b)^{-1} \hat{t}'_n - \hat{r}_a \hat{r}'_n} \hat{t}'_a. \tag{2.83}$$

which has a structure similar to Eq. (2.56). In the same spirit, one is brought to define (compare with Eq. 2.61)

$$\hat{\vec{\sigma}} = \frac{1}{N_{ch}} \mathrm{Tr}_{N_{ch}} \begin{pmatrix} \vec{\sigma}_{\uparrow\uparrow} & \vec{\sigma}_{\downarrow\uparrow} & \vec{\sigma}_{\uparrow\downarrow} & \vec{\sigma}_{\downarrow\downarrow} \\ 0 & 0 & 0 & 0 \\ 0 & 0 & 0 & 0 \\ \vec{\sigma}_{\uparrow\uparrow} & \vec{\sigma}_{\downarrow\uparrow} & \vec{\sigma}_{\uparrow\downarrow} & \vec{\sigma}_{\downarrow\downarrow} \end{pmatrix}. \tag{2.84}$$

Using these matrices, spin torque now reads

$$\left\langle \frac{\partial \tau_b}{\partial V_0} \right\rangle = -\frac{e}{4\pi} \mathrm{Re}\mathrm{Tr}_4[\hat{\vec{\sigma}} \hat{\Omega}] \tag{2.85}$$

and the total transmission hat matrix of the system reads

$$\hat{t} = \hat{t}'_b \hat{\Omega} \tag{2.86}$$

After the averaging one has that $\langle \partial \tau_b / \partial V_0 \rangle = -\langle \partial \tau_b / \partial V_3 \rangle$ (see [103]), so that the linear response of the torque to a small bias voltage (which is the regime we want to describe) reads

$$\tau_b = \left\langle \frac{\partial \tau_b}{\partial V_0} \right\rangle (V_0 - V_3). \tag{2.87}$$

Averaging over the propagative channel has allowed us to reduce enormously the parameters of the model, without losing generality and physical insight. Scattering matrix provides a fully phase coherent description of the FNF trilayer, containing $4N_{ch} \times 4N_{ch}$ parameters for each of the transmission/reflection matrices of the system. Averaging over the propagative channels reduces the parameters to 16 for each hat matrix appearing in the computation, while completely eliminates the phase coherence. For an Ohmic, diffusive spin valve, the physics of transport is fully caputured by Random Matrix Theory.

2.4.4 Rotation of hat matrices

The scattering matrix of a piece of magnetic material is most easily found in the basis parallel to the local magnetization, *i.e.* the reflection and transmission matrices are given for the majority and minority electrons. For non-collinear multilayers where different magnetization directions come into play, one needs to rotate the original S matrix onto its form

$$\tilde{S} = R_{\theta,\vec{n}} S R^{\dagger}_{\theta,\vec{n}} \tag{2.88}$$

in the chosen working basis, where

$$R_{\theta,\vec{n}} = \exp(-i\vec{\sigma}\cdot\vec{n}\ \theta/2) = \cos(\theta/2) - i\vec{\sigma}\cdot\vec{n}\ \sin(\theta/2) \tag{2.89}$$

is the rotation matrix of angle θ around the unit vector $\vec{n}$ that brings the magnetization onto the z-axis of the working basis. In term of hat matrices, this translates directly into

$$\hat{\tilde{S}} = \hat{R}_{\theta,\vec{n}} \hat{S} \hat{R}^{\dagger}_{\theta,\vec{n}} \tag{2.90}$$

with,

$$\hat{R}_{\sigma\eta,\sigma'\eta'} = R_{\sigma\sigma'} R^{*}_{\eta\eta'}, \tag{2.91}$$

a unitary matrix. Rotating hat matrices allows one to describe transport for noncollinear systems,as we have done with scattering matrices.

2.5 Green's function and quantum transport

The scattering matrix provides the response at one lead due to an excitation at another. Green's function is a more general concept that allows to determine the response at any point of the system due to an excitation at any other. When electron-electron or electron-phonon interactions are present, one has to include excitation inside the conductor and Green's function formalism is a powerful tool to describe electronic transport in this case (see for example [26, 27]). As we shall see in this section, global and transport properties of a multilayer connected to an arbitrary number of leads are directly related to the Green's function.

For non interacting transport, the only excitations that one has to take into account are those due to the waves incident from the leads to the system. In this simple case, scattering matrix and Green's function are related concept, and one can use both formalisms in an equivalent way. In particular, one can express transmission and reflection coefficients of the system via the Green's function [see Sec.(4.3)].

2.5.1 Green's function and self energy

For a system with Hamiltonian $\mathcal{H}$, the retarded Green's function $G(\boldsymbol{r},\boldsymbol{r}')$ is the solution of the equation $\mathcal{H}G(\boldsymbol{r},\boldsymbol{r}')=\delta(\boldsymbol{r},\boldsymbol{r}')$, that describes the response at position $\boldsymbol{r}$ due to an excitation at $\boldsymbol{r}'$. G is defined as

$$G=[E-\mathcal{H}+i\eta]^{-1} \tag{2.92}$$

E being the energy of the system, and $i\eta\to0^+$ being a small imaginary part that includes boundary conditions. To solve Eq.(2.92) numerically, we discretize the spatial coordinates so that the conductor becomes a network of C sites, and $G(\boldsymbol{r},\boldsymbol{r}')$ becomes the $C\times C$ matrix G_{ij}, which relates the response at site i to an exitation at site i.

The Green's function of our system has, in addition to the coordinates, two indexes for the spin (that take into account spin preserving and spin-flip transmission/reflection phenomena). these indexes will be introduced later to express the relation between G and the scattering matrix.

Once the Hamiltonian for the discrete system has been defined, the computation of G consists in finding the the matrix $[(E+i\eta)1-\mathcal{H}]^{-1}$. Since the leads extend to infinity, the coductor is an open system. If one simply truncates the matrix at some point, then one would effectively be describing a closed system with fully reflecting boundaries.

The open system can be described by a closed one with new boundary conditions, given by the presence of the leads. In particular, we add a term to the Hamiltonian, called *self energy* Σ_p^R, that describes the interaction between the system and lead p [See FIG.(2.9)]. The superscript R is a reminder that this self energy refers to the retarded Green's function. Self

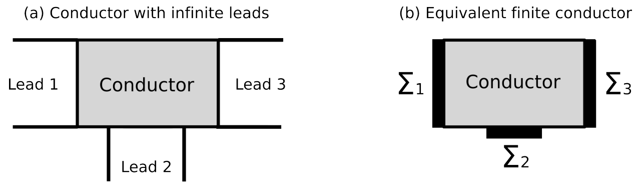

Figure 2.9: Cartoon representing a conductor connected to three leads that extend to infinity(a), and a finite conductor whose leads have been substituted with self-energies (b). Self-energy describe the effect of the leads on the conductor, and correspond to an additional term of the Hamiltonian of the system.

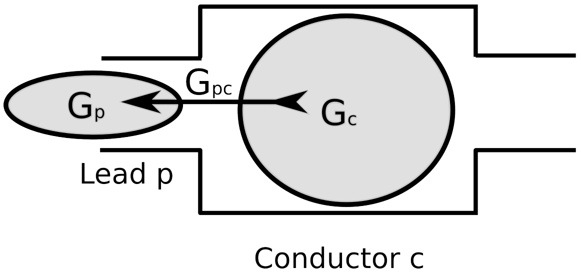

Figure 2.10: Cartoon of a conductor connected to two leads. The overall Green's function can be split into a component for the isolated lead p (G_p), a component for the isolated conductor c (G_c), and a component that couples the two system (G_{pc})

energy is defined as follows: consider a conductor connected to the lead p as shown in FIG. (2.10). The Hamiltonian of the whole system can be split into three terms $\mathcal{H}_C$, $\mathcal{H}_p$ and V_{pC}, that describe respectively the conductor C, the lead p and the coupling between them. In the same way one can divide the Green's function into $G_C = [(E + i\eta)1 - \mathcal{H}_C]^{-1}$, $G_p = [(E + i\eta)1 - \mathcal{H}_P]^{-1}$ and $G_{pC} = [(E + i\eta)1 - V_{pC}]^{-1}$ for the three systems. One can show that (see [26]) $\Sigma_p^R = (V_{pC})^\dagger G_{pC} V_{pC}$, and that the Green's function that takes into account the presence of the leads reads

$$G = \left(E1 - \mathcal{H}_C - \Sigma^R\right)^{-1} \tag{2.93}$$

$\Sigma^R = \sum_p \Sigma_p^R$ is the total self-energy of the system. In a similar way, one can define the advanced self energy Σ_p^A related to the advanced Green's function [26].

The eigenvalue equation $\left(H_C + \Sigma^R\right)\psi_\alpha = \varepsilon_\alpha \psi_\alpha$ of the system in presence of self-energy allows to get insight on the effect of the leads of the system. The eigenenergies are now complex:

$$\varepsilon_\alpha = \epsilon_{\alpha 0} - \Delta_\alpha - \frac{i}{2}\gamma, \tag{2.94}$$

where $\varepsilon_{\alpha 0}$ is the eigenenergy of the isolated conductor described by $\mathcal{H}_\mathcal{C}$. The time evolution operator reads

$$\exp\{-i\varepsilon_\alpha t/\hbar\} \to \exp\{-i(\varepsilon_{\alpha 0} - \Delta_\alpha)t/\hbar\} \exp\{-\gamma_\alpha t/2\hbar\}. \tag{2.95}$$

Δ_α represents the shift in the energy due to the modification of the dynamics of the particle inside the conductor by the interaction with the leads, while the imaginary part of the energy γ_α make Eq. (2.95) exponentially decaying in time. the quantity $|\psi_\alpha(t)|^2 = |\psi_\alpha|^2 \exp\{-\gamma_\alpha t/\hbar\}$ expresses the probability to find an electron inside the conductor. This means that a particle injected anywhere in the conductor will disappear through one of the leads after a characteristic time $\hbar/\gamma_\alpha$.

The properties of the leads are described by the matrix $\Gamma = i(\Sigma^R - \Sigma^A)$. In Sec.(4.3) we shall see how to relate this matrix to the eigenfunctions of the system.

Once we have chosen the shape of the conductor, the position of the leads and the number of sites C of the whole system, and we have written the Hamiltonian, the problem of finding the Green's function is completely defined, and the computation consists in inverting a matrix with $C \times C$ elements. To compute the Green's function G in a performant way, we start considering a small region of the conductor, described by the Green's function g, and coupled to a neighbouring region with a small term U, such that one has $G^{-1} = g^{-1} - U$. One can express G using the *self consistent Dyson equation* [26]

$$G = g + gUG, \tag{2.96}$$

That can be expanded into the perturbative series $G = g + gUg + gUgUg + gUgUgUg + ...$, which allows to express G as a function of the unperturbed Green's function g and of the perturbation U. The technique at the basis of the calculations that we have performed is the following: after we have divided the system into a network of sites, we define a Hamiltonian that contains a probability amplitude for an electron to jump from one site to the other. We compute at first the Green's function of a site, and we treat the hopping with neighbouring sites as the perturbation U. The Green's function can be computed adding one site at a time until the whole system is described.

2.5.2 A short introduction to NEGF formalism

Local and transport properties of a quantum system, described by a given Hamiltonian and connected to several leads, can be calculated via the formalism of the Non Equilibrium Green's Functions (NEGF) [54, 21]. This formalism allows to properly take into account the transport properties of the system, and the interactions of the systems with the "external world", modeled by a certain number of leads, connected to electron reservoirs. Each lead p is described via a self-energy, and the statistics of the electron reservoirs are described by the Fermi function, which takes into account the temperature T_p and the chemical potential μ_p of lead p. In the formalism of second quantization, the *non equilibrium lesser Green function* reads

$$G^{<}_{\sigma i,\eta j}(E) = i \int dt e^{-iEt} \left\langle c^{\dagger}_{\eta j} c_{\sigma i(t)} \right\rangle \tag{2.97}$$

where the indexes (i, j) stand for position in the lattice and the indexes (σ, η) for spin, while $c^{\dagger}_{\sigma i}$ and $c_{\sigma i}$ are the usual creation and annihilation operators for an electron propagating inside the lattice. The simplicity of this formalism comes from the fact that in our case, without electron-electron interaction, $G^{<}$ can be written in terms of the retarded Green's function G, defined in Eq.(2.93):

$$G^{<} = G \sum_{p} f_p (\Sigma^{\dagger}_p - \Sigma_p) G^{\dagger}, \tag{2.98}$$

where $f_p = 1/(1 - \exp[(E - \mu_l)/kT_p])$ is the Fermi function, and Σ_p are the self-energies at lead p. Eqs. (2.97) and (2.98) together allows to go from language of creation and annihilation operators to the languages of retarded Green's functions. For example, the spin density at site i reads

$$\vec{n}_i = \frac{\hbar}{2} \sum_{\eta,\eta'} c^{\dagger}_{i\eta} \vec{\sigma}_{\eta\eta'} c_{i\eta'} \tag{2.99}$$

and using $G^{<}$ one has

$$\eta_i = \frac{1}{2\pi} Im \int_{-\infty}^{+\infty} dE G^{<}_{ii}(E). \tag{2.100}$$

Spin current is calculated from the time evolution of spin density, which depends on the Hamiltonian of the system:

$$\frac{\partial}{\partial t} \langle n_i \rangle = \frac{i}{\hbar} \langle [H, n_i] \rangle . \tag{2.101}$$

To resolve this equation, it is necessary to specify the Hamiltonian of the system. This approach is taken in chapter 4, where we consider a Tight-Binding (TB) Hamiltonian, and we represent the system as a discrete lattice. The TB Hamiltonian shall be described in chapter 4, here we anticipate that this Hamiltonian is the sum of three parts (hopping, spin orbit interaction and impurity potential), so that the commutator $[H, n_i]$ splits into three separate terms, from which one obtains three current densities having different physical meaning:

$$
\begin{aligned}
\boldsymbol{j}_{\sigma,ij} &= -\frac{1}{2}\mathrm{Im}\left\{t_{ij}\left\langle c^{\dagger}_{\sigma i}\vec{\sigma}_{\sigma\sigma}c_{\sigma j}\right\rangle\right\} && (2.102)\\
\boldsymbol{j}^{so}_{\sigma i,\eta j} &= -\frac{1}{2}\mathrm{Im}\left\langle c^{\dagger}_{\sigma i}t^{so}_{\sigma i,\eta j}\vec{\sigma}c_{\eta j}\right\rangle && (2.103)\\
\rho_{\sigma i} &= \frac{2}{\hbar}(\vec{V}_{\sigma i}\times\vec{n}_{\sigma}i) && (2.104)
\end{aligned}
$$

Eq.(2.102) corresponds to spin current density associated to transmission and reflection phenomena that preserve the spin, Eq.(2.103) correspond to spin current densities of spin-flip processes, and Eq. (2.104) is a spin density associated to the onsite potential. Notice that at equilibrium the spin density is constant in time, so that the first term of Eq.(2.101) vanishes, so that the three current densities are related:

$$\boldsymbol{j}_{\sigma,ij} + \boldsymbol{j}^{so}_{\sigma i,\eta j} + \rho_{\sigma i} = 0. \qquad (2.105)$$

The first term is the one we refer to as spin current density, and is the one used in our computations to obtain spin torque. These terms can be written using lesser Green's functions. In particular, spin current density reads:

$$
\begin{aligned}
\boldsymbol{j}_{ij} &= \frac{1}{4\pi}\int dE(t_{ij}\vec{\sigma}G^{<}_{ji} - t_{ji}\vec{\sigma}G^{<}_{ij}). && (2.106)\\
& && (2.107)
\end{aligned}
$$

In our picture the system is divided into sites, and $\boldsymbol{j}_{ij}$ refers to the spin current that propagates from site i to site j. We are interested in the total spin current that flows through a cross section of the system. Such current is obtained summing $\boldsymbol{j}_{ij}$ over the cross section of the system. Substituting $G^{<}$ with Eq.(2.98), one obtains spin current expressed using retarded Green's functions. We remind that we consider zero temperature, where the Fermi function reduces to a step function, and electronic transport occurs near the Fermi Energy.

The formalism described in this section has been adopted for transport calculations described in chapter 4. The computations have been performed using the KNIT package [80], based on an algorithm described in Ref.[53], that allows to compute Green functions for a system with arbitrary geometry, connected to an arbitrary number of electron reservoirs.

Chapter 3

Continuous Random Matrix Theory

3.1 Introduction

The basic ingredients of the RMT theory presented in the previous chapter are the hat matrices of the various subparts of the system. Once those are known, they can be concatenated to obtain various physical observables using the sum rule defined in Eq.(2.68). There are two routes that one can take to obtain those matrices. The first one is to go back to their definition in term of the original quantum problem, and compute them from purely quantum calculations. This route has been taken with ab-initio calculation for the interfaces between several magnetic and non-magnetic layers [110, 106]. In next chapter we shall describe a quantum approach to magnetic multilayer based on TB Hamiltonian. The second route taken here is to derive those matrices from phenomenological considerations.

In Sec.(3.2) we associate to hat matrices some probability vectors that account for the probability for an electron to be in a specific region of the system. These vectors play the role of the wave functions in the scattering formalism, and allow one to define spin accumulation and spin current in a natural way.

In Sec.(3.3) we show how to derive hat matrices from phenomenological considerations. The $\hat{S}$ matrix for a piece of bulk material or for an interface between two different metals will be parametrized by a few parameters. The leading idea behind this parametrization is that a conductor can be divided in infinitely thin "slices". Once the hat matrix of a "slice" is known, we can determine the hat matrix of the system as a whole, integrating this matrix over the length of the system. The model obtained with this procedure is what we call Continuous Random Matrix Theory (CRMT) [79].

In Sec.(3.4) we show how to put CRMT parameters in one to one correspondance with the parameters of the well established Valet-Fert theory

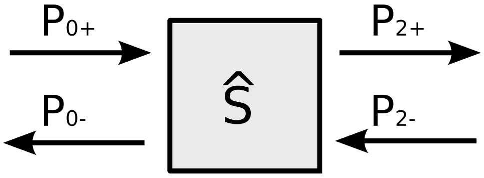

Figure 3.1: Cartoon of the $\hat{S}$ matrix approach. We define the region 0 on the left and the region 2 on the right (region 1 in between will appear later in the text). The + (−) respectively stands for right (left) going modes. The mode amplitude $\psi_{i\pm\sigma}$ at the quantum level become $P_{i\pm\sigma}$ in RMT.

described in Sec.(2.2.1). This has a double advantage, since it allows to make a direct connection with a widely spread theory, and it also allows to make direct use of the important experimental effort that has been done to parametrize Valet-Fert theory.

In Sec.(3.5) we make the link between CRMT and Generalized Circuit Theory [7], a powerful tool that allows to perform transport calculations in noncollinear configuration of the magnetization.

Sec.(3.6) is dedicated to a direct integration of CRMT in some simple cases. This allows for a better definition of the VF parameters in diffusive systems.

In the Sec.(3.7) whe show some application of the theory to the computation of spin accumulation and spin torque in realistic spin valves.

3.2 Hat matrices and probability vectors

3.2.1 Probability 4-vectors

The matrix $\hat{S}$ contains transmission and reflection probabilities for right-moving and left-moving electrons, and has a form similar to Eq.(2.35),

$$\hat{S} = \begin{pmatrix} \hat{r}' & \hat{t} \\ \hat{t}' & \hat{r} \end{pmatrix}, \tag{3.1}$$

In analogy with scattering matrices, we introduce 4-vectors $\boldsymbol{P}_{i\pm}$, which corresponds to the modes amplitudes $\boldsymbol{\psi}_{i\pm\sigma}$:

$$\boldsymbol{P}_{i\pm} = \begin{pmatrix} P_{i\pm,\uparrow} \\ P_{i\pm,mx} \\ P^{*}_{i\pm,mx} \\ P_{i\pm,\downarrow} \end{pmatrix} \tag{3.2}$$

The components of the 4-vector $\boldsymbol{P}_{i\pm}$ have interpretation in term of probabilities. For instance, $\boldsymbol{P}_{0+\uparrow}$ ($\boldsymbol{P}_{2-\downarrow}$) accounts for the probability to find a right (left) moving electron in region 0 (2) with spin ↑ (↓) [see FIG.(3.1)]. The mixing components, P_{mx} are complex numbers which correspond to the probability to find the electron with spin along the x (real part) or y (imaginary part) axis. Inside magnetic layers where the z axis will correspond to the direction of the magnetization, they will correspond to the small probability for the spin to have a part transverse to the magnetization. Again, in analogy with Eq.(2.35) which expresses the amplitudes of the outgoing modes in term of the incoming ones, we have,

$$\begin{pmatrix} \boldsymbol{P}_{0-} \\ \boldsymbol{P}_{2+} \end{pmatrix} = \hat{S} \begin{pmatrix} \boldsymbol{P}_{0+} \\ \boldsymbol{P}_{2-} \end{pmatrix}. \tag{3.3}$$

When the "mixing" components of the 4-vectors play no role, as in collinear systems, Eq.3.3 has an obvious interpretation in term of a Master equation. For instance, its first row expresses that the probability to find a left going electron in region 0 has two contributions coming from the probability to have a reflection and transmission event. In other word, instead of the original interference problem with amplitudes, one now deals with the classical equivalent with probabilities. For non-collinear system however, the presence of the quantum SU(2) structure of the spin introduces some quantum numbers (the mixing coefficients) and the Markov process interpretation does not hold, strictly speaking.

The expression for the currents and spin current in term of the "hat" matrices given in Eqs.(2.58) and (2.58), can be now reformulated in terms of $\boldsymbol{P}$-vectors:

$$\boldsymbol{J}_i = \frac{N_{ch}}{4\pi} \left[\vec{\boldsymbol{\sigma}} \cdot \boldsymbol{P}_{i+} - \vec{\boldsymbol{\sigma}} \cdot \boldsymbol{P}_{i-} \right] \tag{3.4}$$

and

$$\boldsymbol{I} = \frac{1}{e\mathcal{R}_{sh}} [P_{+\uparrow} + P_{+\downarrow} - P_{-\uparrow} - P_{-\downarrow}] \tag{3.5}$$

where I is the charge current and $\mathcal{R}_{sh} = h/(N_{ch}e^2)$ is the Sharvin resistance. $\vec{\vec{\sigma}} = (\vec{\sigma}_{\uparrow\uparrow}, \vec{\sigma}_{\downarrow\uparrow}, \vec{\sigma}_{\uparrow\downarrow}, \vec{\sigma}_{\downarrow\downarrow})$ is 4-vector composed of components of Pauli matrices. To complete the theory, we need the boundary conditions imposed on the incoming electrons on both sides of the system. We focus here on normal electrodes, but these conditions can be easily generalized to the case where the electrodes are themselves magnetic. We have,

$$\boldsymbol{P}_{0+} = \begin{pmatrix} \mu_0 \\ 0 \\ 0 \\ \mu_0 \end{pmatrix}, \quad \boldsymbol{P}_{2-} = \begin{pmatrix} \mu_2 \\ 0 \\ 0 \\ \mu_2 \end{pmatrix} \tag{3.6}$$

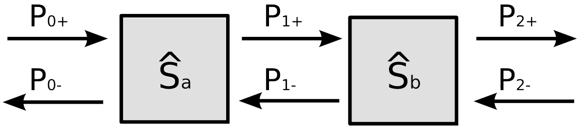

Figure 3.2: Cartoon of the system made of two subsystems a and b.

where μ_0 and μ_2 are the respective chemical potentials of the two electrodes. For a given matrix $\hat{S}$, the combinations of Eqs.(3.3,3.4,3.5) and Eq.(3.50) form a complete set of equations to obtain the physical quantities. Eq.(3.3) reads for each of them,

$$\begin{pmatrix} \boldsymbol{P}_{0-} \\ \boldsymbol{P}_{1+} \end{pmatrix} = \hat{S}_a \begin{pmatrix} \boldsymbol{P}_{0+} \\ \boldsymbol{P}_{1-} \end{pmatrix}, \begin{pmatrix} \boldsymbol{P}_{1-} \\ \boldsymbol{P}_{2+} \end{pmatrix} = \hat{S}_b \begin{pmatrix} \boldsymbol{P}_{1+} \\ \boldsymbol{P}_{2-} \end{pmatrix} \tag{3.7}$$

Eliminating $\boldsymbol{P}_1$ we find addition law for hat-matrices:

$$\begin{pmatrix} \boldsymbol{P}_{0-} \\ \boldsymbol{P}_{2+} \end{pmatrix} = \hat{S}_{a+b} \begin{pmatrix} \boldsymbol{P}_{0+} \\ \boldsymbol{P}_{2-} \end{pmatrix} \text{with,} \tag{3.8}$$

$$\hat{t}_{a+b} = \hat{t}_b \frac{1}{\hat{1} - \hat{r}'_a \hat{r}_b} \hat{t}_a \tag{3.9}$$

$$\hat{r}_{a+b} = \hat{r}_a + \hat{t}_a \hat{r}_b \frac{1}{\hat{1} - \hat{r}'_a \hat{r}_b} \hat{t}_a \tag{3.10}$$

and similar expressions for $\hat{r}'_{a+b}$ and $\hat{t}'_{a+b}$, which justifies Eq.(2.68). We can also use Eq.(3.7) to express $\boldsymbol{P}_{1\pm}$ in terms of the incoming fluxes:

$$\begin{pmatrix} \boldsymbol{P}_{1+} \\ \boldsymbol{P}_{1-} \end{pmatrix} = \begin{pmatrix} \frac{1}{1 - \hat{r}'_a \hat{r}_b} \hat{t}_a & \hat{r}'_a \frac{1}{\hat{1} - \hat{r}_b \hat{r}'_a} \hat{t}'_b \\ \hat{r}_b \frac{1}{\hat{1} - \hat{r}'_a \hat{r}_b} \hat{t}_a & \frac{1}{1 - \hat{r}_b \hat{r}'_a} \hat{t}'_b \end{pmatrix} \begin{pmatrix} \boldsymbol{P}_{0+} \\ \boldsymbol{P}_{2-} \end{pmatrix} \tag{3.11}$$

Using Eqs.(3.4,3.50,3.11), one can calculate the spin current in the region 1 inside the system.

3.2.2 From scattering degrees of freedom to spin accumulation and spin current

The natural variables of RMT, as it was introduced above, are the 4-vectors $\boldsymbol{P}_{x\pm}$ which characterize the "probability" to find a left or right moving electron in region x. Let us now introduce a new set of variables defined as

$$\boldsymbol{j}(x) = [\boldsymbol{P}_+(x) - \boldsymbol{P}_-(x)]/(e\mathcal{R}_{\text{sh}}), \tag{3.12}$$

$$\boldsymbol{\mu}(x) = [\boldsymbol{P}_+(x) + \boldsymbol{P}_-(x)]/2 \tag{3.13}$$

As we shall see, these two 4-vectors correspond respectively to the spin resolved current and chemical potentials flowing in the system. There are two complementary ways to make this connection. The first one is to write our fundamental equations [essentially Eq.(3.3)] in term of these new variables. This will be done toward the end of this section, and we will find that $\boldsymbol{j}(x)$ and $\boldsymbol{\mu}(x)$ satisfies the well known Valet-Fert diffusive equations for continuous collinear systems and the equations of circuit theory for discrete non-collinear ones. This connection is very interesting from the theoretical point of view as very different routes have been taken to obtain these equations (scattering and Random matrix theory on one side and Keldysh Green function formalism and quasi-classical approximation on the other side). It has also a practical interest as one can use Eq.(3.12) and Eq.(3.13) to go back and forth between a "scattering" approach and a "diffusive" approach and both have technical advantages for practical calculations.

There is a second, more direct, way to connect respectively $\boldsymbol{j}(x)$ and $\boldsymbol{\mu}(x)$ to the concepts of spin currents and spin accumulation. For $\boldsymbol{j}(x)$, the connection is staightforward, as Eq.(3.4) reads,

$$\vec{J}(x) = \frac{\hbar}{2e}\vec{\vec{\sigma}} \cdot \boldsymbol{j}(x) \tag{3.14}$$

while

$$I = \boldsymbol{j}_\uparrow + \boldsymbol{j}_\downarrow \tag{3.15}$$

The connection between $\boldsymbol{\mu}(x)$ and a hypothetical spin resolved chemical potential is more problematic as scattering theory does not have any notion of local chemical potential. In fact, the existence of a local chemical potential would imply some sort of local equilibrium inside the system. However, the theory that we have developed so far is purely elastic and such a local equilibrium is not present. We will find that everything happens *as if* there were some sort of local equilibrium, except for one important point: the presence or absence of the contact resistance (see the discussion at the end of this section).

In order to provide a physical undertanding of $\mu(x)$, we make use of a theoretical method known as the voltage probe [17, 18]: we connect a point inside the system (region 1) to an external electrode and adjust the (spin resolved) chemical potential of this electrode so that no (spin) current flow from/to it. In the absence of magnetism, this could be achieved experimentally with the help of a STM tip. In mesoscopic physics, the voltage probe is used to induce some decoherence [55] in an otherwise perfectly coherent theory, hence introducing a finite phase coherence time which depends on the coupling of the system with the probe. Here, we will take this coupling to be extremely small, so that the probe will not affect the physics of the system. On the other hand, we are interested in the voltage that one must apply on the probe to stop any current from flowing from/to it: this will be

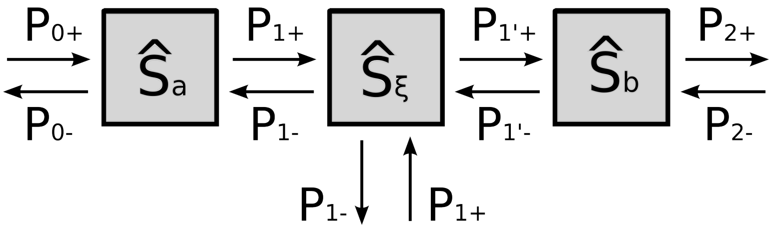

Figure 3.3: Cartoon of the system in presence of the voltage probe.

our definition of an *effective* local chemical potential, and we shall find that this definition matches the one of $\mu(x)$. The setup is shown in FIG.(3.3).

In addition to $\hat{S}_a$ and $\hat{S}_b$ defined previously, we introduce the matrix $\hat{S}_\epsilon$ which describe the (small) coupling to the probe,

$$\hat{S}_\epsilon = \begin{pmatrix} 0 & 1-\epsilon & \epsilon \\ 1-\epsilon & 0 & \epsilon \\ \epsilon & \epsilon & 1-2\epsilon \end{pmatrix}, \tag{3.16}$$

with $\epsilon \ll 1$. When $\epsilon = 0$ the probe is decoupled from the conductor and the electrons freely propagate between the regions 1 and $1'$.

The full system is entirely determined by the following set of equations,

$$\begin{pmatrix} \boldsymbol{P}_{0-} \\ \boldsymbol{P}_{1+} \end{pmatrix} = \hat{S}_a \begin{pmatrix} \boldsymbol{P}_{0+} \\ \boldsymbol{P}_{1-} \end{pmatrix}, \begin{pmatrix} \boldsymbol{P}_{1'-} \\ \boldsymbol{P}_{2+} \end{pmatrix} = \hat{S}_b \begin{pmatrix} \boldsymbol{P}_{1'+} \\ \boldsymbol{P}_{2-} \end{pmatrix}$$
$$\begin{pmatrix} \boldsymbol{P}_{1-} \\ \boldsymbol{P}_{1'+} \\ \boldsymbol{P}_{p-} \end{pmatrix} = \hat{S}_\epsilon \begin{pmatrix} \boldsymbol{P}_{1+} \\ \boldsymbol{P}_{1'-} \\ \boldsymbol{P}_{p+} \end{pmatrix}, \tag{3.17}$$

to which one must add the incoming boundary conditions on the three electrodes $\boldsymbol{P}_{0+}$, $\boldsymbol{P}_{2-}$ [Eq.(3.50)] and $\boldsymbol{P}_{p+}$ (the probe). Eliminating $\boldsymbol{P}_{1,1'}$ we obtain $\hat{S}$. In particular we get to leading order in ϵ,

$$\begin{aligned} \hat{S}_{p,0} &= \epsilon(\hat{1} + \hat{r}_b)\frac{1}{\hat{1} - \hat{r}'_a\hat{r}_b}\hat{t}_a \\ \hat{S}_{p,2} &= \epsilon(\hat{1} + \hat{r}_a)\frac{1}{\hat{1} - \hat{r}_b\hat{r}'_a}\hat{t}'_b \\ \hat{S}_{p,p} &= 1 - 2\epsilon + O(\epsilon^2) \end{aligned} \tag{3.18}$$

We now impose that $\boldsymbol{J}_p = 0$ [Eq.(3.4)] which provides our boundary condition on the probe:

$$\boldsymbol{P}_{p+} = \frac{1}{2\epsilon}\hat{S}_{p,0}\boldsymbol{P}_{0+} + \frac{1}{2}\hat{S}_{p,2}\boldsymbol{P}_{2-} \tag{3.19}$$

Using Eq.(3.11) and Eq.(3.13), we arrive at,

$$\boldsymbol{P}_{p+} = \frac{1}{2}\left(\boldsymbol{P}_{1+} + \boldsymbol{P}_{1-}\right) = \boldsymbol{\mu}_1 \tag{3.20}$$

In other words, the spin resolved voltages that one need to apply on the probe is equal to the formal chemical potential that we have defined in Eq.(3.13) so that it is legitimate to call $\mu(x)$ a chemical potential.

3.3 Continuous Random Matrix Theory

3.3.1 General form of the hat matrices in magnetic and non magnetic materials.

A typical magnetic multilayer consists of alternating layers of magnetic and non-magnetic materials of various widths. We decompose the corresponding S matrices in the bulk and interface parts that will be parametrized independently. The general form of a hat matrix ($\hat{t}$ in what follows but similar considerations apply to t', r and r') is a full 4×4 matrix given by Eq.(2.72). In the absence of spin-orbit scattering (and/or magnetic impurities), spin is a good quantum number of the problem and the t matrix is diagonal in spin space (in the basis parallel with the magnetization). Hence $\hat{t}$ is also diagonal. It consists on one hand of the probabilities $T_{\uparrow\uparrow}$ ($T_{\downarrow\downarrow}$) for an ↑ (↓) spin to be transmitted and on the other hand of the mixing transmission, $T_{mx} = (1/N_{ch})\mathrm{Tr}_{Nch}(t_{\uparrow\uparrow}t_{\downarrow\downarrow})$. In order to take into account spin-orbit interaction, a finite probability $T_{\uparrow\downarrow}$ ($T_{\downarrow\uparrow}$) for a ↓ (↑) spin to be transmitted as a ↑ (↓) spin must be considered (spin flip probabilities). In the following, we suppose that mixing elements (complex numbers) that also involve spin-flip scattering can be totally ignored, leading to the following form of the hat-matrix:

$$\hat{t} = \begin{pmatrix} T_{\uparrow\uparrow} & 0 & 0 & T_{\uparrow\downarrow} \\ 0 & T_{mx} & 0 & 0 \\ 0 & 0 & T_{mx}^{*} & 0 \\ T_{\downarrow\uparrow} & 0 & 0 & T_{\downarrow\downarrow} \end{pmatrix}. \tag{3.21}$$

with the probabilities $T_{\sigma\sigma'} = 1/N_{ch}\mathrm{Tr}_{N_{ch}}(t^{\dagger}_{\sigma\sigma'}t_{\sigma\sigma'})$. Note that the unitarity of the S matrix imposes the following constraint on the mixing coefficient:

$$|T_{mx}| \leq \sqrt{T_{\uparrow\uparrow}T_{\downarrow\downarrow}}. \tag{3.22}$$

In a non-magnetic material there is no preferred direction for the spin, thus a hat matrix of the non-magnetic metal must be invariant with respect to rotations. One finds by inspection that there are two 4×4 matrices invariant with respect to rotation around an arbitrary axis:

$$\hat{I}_1 = \begin{pmatrix} 1 & 0 & 0 & 0 \\ 0 & 1 & 0 & 0 \\ 0 & 0 & 1 & 0 \\ 0 & 0 & 0 & 1 \end{pmatrix}, \quad \hat{I}_2 = \begin{pmatrix} 1 & 0 & 0 & 1 \\ 0 & 0 & 0 & 0 \\ 0 & 0 & 0 & 0 \\ 1 & 0 & 0 & 1 \end{pmatrix} \tag{3.23}$$

Hence, we write the hat matrix of a normal layer as a combination of these two invariants:

$$\hat{t} = [T - 2T_{sf}]\hat{I}_1 + T_{sf}\hat{I}_2. \tag{3.24}$$

where T is the total transmission probability while T_{sf} is the probability of transmission with spin-flip.

3.3.2 hat matrices for an infinitely thin conductor

So far we have discussed the form of the hat matrices for an arbitrary subpart of the system. This general form is directly useful for the parametrization of the hat matrices of interfaces. For bulk material, we introduce the $\hat{S}$ matrix of a very thin slice of material of width δL. The matrix $\hat{S}(\delta L)$ (and therefore the bulk properties of the material) is entirely characterized by two matrices Λ^t and Λ^r defined as,

$$\hat{t}(\delta L) = 1 - \Lambda^t \delta L \tag{3.25}$$

$$\hat{r}(\delta L) = \Lambda^r \delta L \tag{3.26}$$

Once $\hat{S}(\delta L)$ is known, one can make use of the addition law discussed in Sec.(2.4.1) to obtain a differential equation that allows the computation of $\hat{S}(L)$: combining $\hat{S}(L)$ and $\hat{S}(\delta L)$ one obtains $\hat{S}(L + \delta L)$. For example $\hat{t}(L + \delta L)$ reads

$$\hat{t}(L + \delta L) \approx [\hat{1} + \hat{r}(L)\Lambda^r \delta L - \Lambda^t \delta L]\hat{t}(L). \tag{3.27}$$

So, in the limit $\delta L \to 0$ one obtains

$$\frac{\partial \hat{r}}{\partial L} = \Lambda^r - \Lambda^t \hat{r} - \hat{r}\Lambda^t + \hat{r}\Lambda^r \hat{r} \tag{3.28}$$

$$\frac{\partial \hat{t}}{\partial L} = -\Lambda^t \hat{t} + \hat{r}\Lambda^r t \tag{3.29}$$

Eq.(3.28) and Eq.(3.29) can be integrated analitically to obtain $\hat{S}(L)$ of an arbitrary bulk part (see the following of this chapter). However, for numerical purposes, it is more efficient to use directly Eqs. (3.9) and (3.10) which can be used recursively, leading to an extremely fast integration time $\propto \log L$.

The matrices Λ^t and Λ^r are parametrized by the general form given in Eq.(3.21) an Eq.(3.24). The parametrization is further constrained by the unitarity of S (conservation of current). Due to the origin essentially ballistic of the finite mixing coefficient, we neglect the corresponding contribution to Λ^r. Eventually, a bulk magnetic material is characterized by four independent parameters $\Gamma_\uparrow$, $\Gamma_\downarrow$ $\Gamma_{\rm sf}$ and $\Gamma_{\rm mx}$:

$$\Lambda^t = \begin{pmatrix} \Gamma_\uparrow + \Gamma_{\rm sf} & 0 & 0 & -\Gamma_{\rm sf} \\ 0 & \Gamma_{\rm mx} & 0 & 0 \\ 0 & 0 & \Gamma^*_{\rm mx} & 0 \\ -\Gamma_{\rm sf} & 0 & 0 & \Gamma_\downarrow + \Gamma_{\rm sf} \end{pmatrix}, \tag{3.30}$$

$$\Lambda^r = \begin{pmatrix} \Gamma_\uparrow - \Gamma_{\rm sf} & 0 & 0 & \Gamma_{\rm sf} \\ 0 & 0 & 0 & 0 \\ 0 & 0 & 0 & 0 \\ \Gamma_{\rm sf} & 0 & 0 & \Gamma_\downarrow - \Gamma_{\rm sf} \end{pmatrix}, \tag{3.31}$$

These four parameters correspond in turn to five different lengths. The two most important one are the mean free paths for majority ($l_\uparrow$) and minority ($l_\downarrow$) electrons defined as $l_\sigma = 1/\Gamma_\sigma$. Next comes the spin diffusion length $l_{sf} = [4\Gamma_{sf}(\Gamma_\uparrow + \Gamma_\downarrow)]^{-1/2}$ [see below Eq.(3.40] and Sec.(3.6)). Last the complex number $\Gamma_{\rm mx} = 1/l_\perp + i/l_L$ where $l_\perp$ is the penetration length of transverse spin current inside the magnet while l_L is the Larmor precession length. These definitions are supported by the form of $T_{\rm mx}(L)$ which is readliy obtained by integrating Eq.(3.29),

$$T_{mx}(L) = e^{-L/l_\perp - iL/l_L} \tag{3.32}$$

$l_\perp$ and l_L, are believed to be roughly equal, and the smallest characteristic lengths with typical values in the nm range. The explicit form of $T_{\sigma\sigma'}(L)$ will be discussed in the last section of this chapter. In a normal metal, the parametrization obeys Eq.(3.24) and we have

$$\Lambda^t = [\Gamma + 2\Gamma_{sf}]\hat{I}_1 - \Gamma_{sf}\hat{I}_2. \tag{3.33}$$

$$\Lambda^r = [\Gamma - 2\Gamma_{sf}]\hat{I}_1 + \Gamma_{sf}\hat{I}_2. \tag{3.34}$$

The theory is now formally complete. A given multilayer is then constructed by using the addition law defined in Eq.(2.68) for the various bulk layers and the corresponding interfaces.

3.4 Correspondence between CRMT and Valet Fert theory

VF parameters are experimentally accessible, and allow for a precise characterization of transport properties of many materials. This parametrization can be used to parametrize the matrices Λ^t and Λ^r of CRMT. On one hand, this allows to build a theory of transport whose parameters are *completely determined by experimental data*, on the other hand, it allows to verify that, for collinear systems, VF theory and CRMT are strictly equivalent (up to the way Sharvin resistance is introduced, as we shall see soon).

1. **Parametrization of Bulk.** Let us start with $\hat{S}(\delta x)$ which relates $\boldsymbol{P}_\pm(x)$ and $\boldsymbol{P}_\pm(x+\delta x)$ on the two sides of a thin slice of material according to Eq.(3.3). The explicit form of $\hat{S}(\delta x)$ given by Eqs. (3.26) and (3.26) provides differential equation for $\boldsymbol{P}_\pm(x)$ which are the counterparts of Eq.(3.28) and Eq.(3.29):

$$\begin{aligned}\frac{\partial \boldsymbol{P}_+(x)}{\partial x} &= -\Lambda^t \boldsymbol{P}_+(x) + \Lambda^r \boldsymbol{P}_-(x)\\ \frac{\partial \boldsymbol{P}_-(x)}{\partial x} &= -\Lambda^r \boldsymbol{P}_+(x) + \Lambda^t \boldsymbol{P}_-(x).\end{aligned} \tag{3.35}$$

In the absence of magnetic texture, the equations for $P_{\pm,\uparrow}$ and $P_{\pm,\downarrow}$ are decoupled from the equations for $P_{\pm,mx}$ and $P^*_{\pm,mx}$. Focussing on the first and the last row of the Eq. (3.35) we get explicitly,

$$\frac{\partial}{\partial x}\begin{pmatrix} P_{\uparrow\pm} \\ P_{\downarrow\pm}\end{pmatrix} = -\tilde{\Lambda}^t \begin{pmatrix} P_{\uparrow\pm} \\ P_{\downarrow\pm}\end{pmatrix} + \tilde{\Lambda}^r \begin{pmatrix} P_{\uparrow\mp} \\ P_{\downarrow\mp}\end{pmatrix}, \tag{3.36}$$

where $\tilde{\Lambda}^t$ and $\tilde{\Lambda}^r$ are 2×2 matrices,

$$\tilde{\Lambda}^{t/r} = \begin{pmatrix} \Gamma_\uparrow \pm \Gamma_{\mathrm{sf}} & \mp\Gamma_{\mathrm{sf}} \\ \mp\Gamma_{\mathrm{sf}} & \Gamma_\downarrow \pm \Gamma_{\mathrm{sf}}\end{pmatrix} \tag{3.37}$$

Eq.(3.36) accounts for the conservation of probability in the scattering events, *i.e.* it is the Master equation of the underlying Brownian motion undertaken by the electrons upon the various reflection and transmission events.

Using Eq.(3.12) and Eq.(3.13) we can now write Eq.(3.36) in terms of $\boldsymbol{j}(x)$ and $\boldsymbol{\mu}(x)$, and arrive at,

$$j_{\uparrow/\downarrow}(x) = -1/(e\Gamma_\sigma \mathcal{R}_{\mathrm{sh}})\ \partial_x \mu_{\uparrow/\downarrow}(x) \tag{3.38}$$

$$\partial_x j_{\uparrow/\downarrow}(x) = 4\Gamma_{\mathrm{sf}}/(e\mathcal{R}_{\mathrm{sh}})\ [\mu_{\downarrow/\uparrow}(x) - \mu_{\uparrow/\downarrow}(x)] \tag{3.39}$$

which are precisely the Valet-Fert equations. [97] Hence, for a collinear system, C-RMT simply reduces to VF theory. This allows us to build a one to one correspondence between the CRMT parameters ($\Gamma_\uparrow$, $\Gamma_\downarrow$ and Γ_{sf}) and the VF parameters $\rho_\uparrow$, $\rho_\downarrow$ (resistivities for majority and minority electrons) and l_{sf}:

$$\frac{1}{l_{\rm sf}} = 2\sqrt{\Gamma_{\rm sf}}\sqrt{\Gamma_\uparrow + \Gamma_\downarrow} \tag{3.40}$$

$$\beta = \frac{\Gamma_\downarrow - \Gamma_\uparrow}{\Gamma_\uparrow + \Gamma_\downarrow} \tag{3.41}$$

$$\frac{\rho^*}{\mathcal{R}_{\rm sh}} = (\Gamma_\uparrow + \Gamma_\downarrow)/4 \tag{3.42}$$

Note that the mixing coefficient Γ_{mx} is not fixed by this parametrization as they only play a role in non collinear configurations. So far there are very few experimental data [92] allowing to extract Γ_{mx} so that one often relies on model or *ab-initio* calculations to estimate it.

2. **Parametrization of interfaces.** In VF theory, the interface boundary conditions are obtained by introducing an virtual material of width d, resistivity ρ_σ^{eff} and spin diffusion length $l_{\rm sf}^{eff}$. This virtual material is then taken to be infinitely thin $d \to 0$ while keeping the interface parameters finite: $\delta = d/l_{\rm sf}^{eff}$ and $r_\sigma^b = \rho_\sigma^{eff} d$. Repeating the same procedure for CRMT allows us to map the VF parameters to CRMT interfaces,

$$T_{\uparrow\uparrow} = \frac{(1+e^{-\delta})/2}{1+2(r^{b*}/\mathcal{R}_{sh})(1-\gamma)} \tag{3.43}$$

$$T_{\downarrow\uparrow} = \frac{(1-e^{-\delta})/2}{1+2(r^{b*}/\mathcal{R}_{sh})(1-\gamma)} \tag{3.44}$$

$$T_{\uparrow\downarrow} = \frac{(1-e^{-\delta})/2}{1+2(r^{b*}/\mathcal{R}_{sh})(1+\gamma)} \tag{3.45}$$

$$T_{\downarrow\downarrow} = \frac{(1+e^{-\delta})/2}{1+2(r^{b*}/\mathcal{R}_{sh})(1+\gamma)} \tag{3.46}$$

$$R_{\uparrow\uparrow} = 1 - \frac{1}{1+2(r^{b*}/\mathcal{R}_{sh})(1-\gamma)}, R_{\downarrow\uparrow} = 0 \tag{3.47}$$

$$R_{\downarrow\downarrow} = 1 - \frac{1}{1+2(r^{b*}/\mathcal{R}_{sh})(1+\gamma)}, R_{\uparrow\downarrow} = 0 \tag{3.48}$$

$$\tag{3.49}$$

Alternatively, the interface $\hat{S}$ matrix can be obtained directly from *ab-initio* or model quantum calculations (see the next chapter). Once again, the mixing reflection and transmission coefficients are not fixed by CPP GMR experiments. Those numbers can be extracted from angular resolved magneto-resistance or spin pumping experiments but limited data are available so far [94].

We have just proved that for a collinear system, VF theory and CRMT are simply equivalent. There is however a small difference that appears in the boundary conditions at the electrodes. In CRMT those boundary conditions come from the (quantum) Landauer formula and the presence of different voltages between the reservoirs located at, say, $x = 0$ and $x = L$ imposes $P_{+\sigma}(0) = eV(0)$ and $P_{-\sigma}(L) = eV(L)$ [see Eq.(3.50)]. A direct consequence of these boundary conditions is the existence of a finite resistance (the Sharvin resistance described in the previous chapter), even for perfectly transparent interfaces and materials with negligeable resistivity. In the context of mesoscopic physics, this leads to the quantization of conductance in unit of $2e^2/h$ which has been observed repeatedly [99, 104]. These boundary conditions can be expressed in term of $\mu_\sigma(x)$ and $j_\sigma(x)$, and give,

$$\begin{aligned}
\boldsymbol{\mu}_\sigma(0) + (e\mathcal{R}_{\rm sh}/2)\; j_\sigma(0) &= eV(0) \qquad (3.50)\\
\boldsymbol{\mu}_\sigma(L) - (e\mathcal{R}_{\rm sh}/2)\; j_\sigma(L) &= eV(L) \qquad (3.51)
\end{aligned}$$

In other words, one needs to add $\mathcal{R}_{\rm sh}/2$ resistors on the two sides of the multilayer. For typical spin valve pillars, the intrinsic resistance of the pillar is only a few time $\mathcal{R}_{\rm sh}$ so that one really needs to take into account the presence of these Sharvin resistances in series to properly describe the pillar. We note that those proper boundary conditions can easily be included in a standard VF calculation.

3.5 Correspondance between CRMT and Generalized Circuit Theory

Let us now turn to non-collinear configurations. An alternative popular and powerful approach in this case is the so-called circuit theory[7] where the system is discretized into various parts connected by "nodes" where one defines the spin resolved chemical potential. Circuit theory, initially derived for very resistive elements has been further extended into the "generalized" circuit theory to properly take into account the Sharvin resistance. The similarity between (generalized) circuit theory and RMT was recognized very early and it was shown in many cases that both theories gave the same result [14]. Here we show that the analogy is in fact complete: RMT and generalized circuit theory are the same theory written in different variables: $\boldsymbol{P}_+$ and $\boldsymbol{P}_-$ for RMT and $\boldsymbol{\mu}$ and $\boldsymbol{j}$ for circuit theory. One simply goes from one to the other using Eq.(3.12) and Eq.(3.13).

The most general version of RMT between the two sides of a conductor is given by Eq.(3.2). Turning now to $\boldsymbol{\mu}$ and $\boldsymbol{j}$ variables on the two sides L (left) and R (right) of the conductor, we get,

$$(\hat{1} + \hat{r} + \hat{o}'\hat{t})\frac{e\mathcal{R}_{\rm sh}}{2}\boldsymbol{j}_R = 2\hat{o}'\boldsymbol{\mu}_L - (\hat{1} - \hat{r} + \hat{o}'\hat{t})\boldsymbol{\mu}_R \tag{3.52}$$

$$(\hat{1} + \hat{r}' - \hat{o}\hat{t}')\frac{e\mathcal{R}_{\rm sh}}{2}\boldsymbol{j}_L = (\hat{1} - \hat{r}' + \hat{o}\hat{t}')\boldsymbol{\mu}_L - 2\hat{o}\boldsymbol{\mu}_R \tag{3.53}$$

where $\hat{o} = t(1 + \hat{r})^{-1}$ and $\hat{o}' = t'(1 + \hat{r}')^{-1}$. These two equations can be seen as the generalization of Ohm law and their linear combination provides the conservation equation for spin current. Eq.(3.52) and Eq.(3.53) can be considered as an extension of (generalized) circuit theory, including in particular interface spin-flip scattering.

To recover generalized circuit theory, we need to make a few assumptions. First, we neglect spin-flip scattering so that the hat matrices are purely diagonal (in the local basis of the magnetization). Second, we suppose that $R_{\rm mx}$ might be non zero but set $T_{\rm mx} = 0$. Eq.(3.52) and Eq.(3.53) simplify into

$$j_{L\sigma} = j_{R\sigma} = \frac{1}{e\mathcal{R}_{\rm sh}}\frac{T_{\sigma\sigma}}{1 - T_{\sigma\sigma}}[\mu_{L\sigma} - \mu_{R\sigma}] \tag{3.54}$$

$$j_{L/R,{\rm mx}} = \pm\frac{2}{e\mathcal{R}_{\rm sh}}\frac{1 - R_{\rm mx}^{L/R}}{1 + R_{\rm mx}^{L/R}}\mu_{L/R,{\rm mx}} \tag{3.55}$$

where $R_{\rm mx}^{L/R}$ are the mixing reflections from left to left ($R_{\rm mx}^{L}$) and right to right ($R_{\rm mx}^{R}$). Eq.(3.54) and Eq.(3.55) are precisely the equations that define generalized circuit theory [7] which proves the equivalence with (C)RMT in this limit. In fact, the renormalization coefficients of generalized circuit theory [7] were chosen such that the calculation of the conductance with RMT and generalized circuit theory fully agree with each other.

3.6 Direct integration of CRMT equations

In this section, we integrate the CRMT equations for the bulk properties of a magnetic layer. The usual route for that would be to use the correspondance between our matrix theory and Valet-Fert diffusion equation. Here, we use a direct integration of Eq.(3.28) and Eq.(3.29), although it is probably more tedious. Eq.(3.28) that defines hat reflection matrix is decoupled from the Eq.(3.29) for hat transmission matrix and should be integrated first. For an homogeneous magnetization, the first and last rows and columns of the hat matrices decouple from the inner (mixing) part so we can effectively consider 2×2 matrices.

We note $\hat{r}_0$ the large L limit of $\hat{r}(L)$. We seek for a solution of Eq.(3.28) in the following form: $\hat{r}(L) = \hat{r}_0 + \hat{r}_1(L)$. Equation for $\hat{r}_1(L)$ takes the form:

$$\frac{\partial \hat{r}_1}{\partial L} = (\hat{r}_0\Lambda^r - \Lambda^t)\hat{r}_1 + \hat{r}_1(\Lambda^r\hat{r}_0 - \Lambda^t) + \hat{r}_1\Lambda^r\hat{r}_1 \tag{3.56}$$

with $\hat{r}_0$ having zeros everywhere except in the corners. We reduce $\hat{r}_0$ to 2×2 matrix r_0 that obey the following equation:

$$\tilde{\Lambda}^r - \tilde{\Lambda}^t r_0 - r_0\tilde{\Lambda}^t + r_0\tilde{\Lambda}^r r_0 = 0 \tag{3.57}$$

here we se 2×2 matrices $\tilde{\Lambda}^{t/r}$ defined in Eq.(3.37) since all transverse spin decayed in infinitely large sample. Using Eq.(3.37) we find:

$$\frac{1-r_0}{1+r_0}\Gamma\frac{1-r_0}{1+r_0} = \Gamma_{sf} I_1 \tag{3.58}$$

with diagonal matrix $\Gamma = \text{diag}(\Gamma_\uparrow, \Gamma_\downarrow)$ and full matrix $I_1 = (1,-1;-1,1)$. Following [84] we find the solution of Eq.(3.58)

$$r_0 = \frac{1-\Gamma_{sf}^{1/2}\Gamma^{-1}(\Gamma I_1)^{1/2}}{1+\Gamma_{sf}^{1/2}\Gamma^{-1}(\Gamma I_1)^{1/2}} \tag{3.59}$$

If we introduce new matrices:

$$\begin{aligned} \hat{r}_1(L) &\equiv e^{\Omega_B L}\bar{r}(L)e^{\Omega_A L} &(3.60)\\ \bar{\Lambda}(L) &\equiv e^{\Omega_A L}\Lambda^r e^{\Omega_B L}, &(3.61)\end{aligned}$$

where $\Omega_A = r_0\Lambda^r - \Lambda^t$ and $\Omega_B = \Lambda^r r_0 - \Lambda^t$. We can rewrite Eq.(3.56) for $\bar{r}$:

$$\frac{\partial \bar{r}^{-1}}{\partial L} = -\bar{\Lambda}(L), \tag{3.62}$$

This equation can be trivially integrated. Applying Eq.(3.60) we find $\hat{r}(L)$ and solving Eq.(3.29) we find $\hat{t}(L)$. The analytical expressions of $\hat{r}(L)$ and $\hat{t}(L)$ for the layer of an arbitrary length L are cumbersome. Let us consider limiting case of a very long layer $L \gg l_{sf}$. From the elements of $\hat{t}$ let us calculate resistivity per spin channel $\rho_{\uparrow\downarrow}$, bulk spin asymmetry β and spin flip length l_{sf}. The resistivity of spin-channels is related to the total transmission probability per spin:

$$\rho_\uparrow = \frac{1}{L}\left(\frac{\mathcal{R}_{\text{sh}}}{T_{\uparrow\uparrow}(L)+T_{\downarrow\uparrow}(L)}\right) \tag{3.63}$$

$$\rho_\downarrow = \frac{1}{L}\left(\frac{\mathcal{R}_{\text{sh}}}{T_{\downarrow\downarrow}(L)+T_{\uparrow\downarrow}(L)}\right). \tag{3.64}$$

Using Eqs.(3.63,3.64) we find analogs of VF resistivity ρ_d^* and spin assymetry β_d in the deep diffusive limit. Spin flip length is related to the decay of the polarization of the spin current that decays exponentially as e^{-L/l_{sf}^d} and eventually saturates toward its assymptotic value β_d

$$\begin{aligned}
\rho_d^* &= (\rho_\uparrow + \rho_\downarrow)/4 && (3.65)\\
\beta_d &= \frac{\rho_\downarrow - \rho_\uparrow}{\rho_\downarrow + \rho_\uparrow} && (3.66)\\
\frac{1}{l_{sf}^d} &= -\frac{1}{L}\log\left(\frac{T_{\uparrow\uparrow}(L) - T_{\downarrow\uparrow}(L)}{T_{\uparrow\uparrow}(L) + T_{\downarrow\uparrow}(L)} - \beta_d\right) && (3.67)
\end{aligned}$$

where $\mathcal{R}_{\text{sh}}$ now represents the Sharvin resistance for a system of unit surface (typically $\mathcal{R}_{\text{sh}} = 0.5\ f\Omega.m^2$ for Cu). We express diffusive VF parameters in terms of parameters in Eq.(3.30) for $\Lambda^{t,r}$ in C-RMT and find the following expressions:

$$\begin{aligned}
\frac{1}{l_{\text{sf}}^d} &= 2\sqrt{\Gamma_{\text{sf}}}\sqrt{\Gamma_\uparrow + \Gamma_\downarrow} && (3.68)\\
\beta_d &= \frac{\Gamma_\downarrow - \Gamma_\uparrow}{\Gamma_\uparrow + \Gamma_\downarrow + 1/l_{sf}^d} && (3.69)\\
\frac{\rho_d^*}{\mathcal{R}_{\text{sh}}} &= (\Gamma_\uparrow + \Gamma_\downarrow)/4. && (3.70)
\end{aligned}$$

Now we compare diffusive values of $l_{sf}^d, \rho_d^*, \beta_d$ with ones found from the mapping of the underlying C-RMT equations with VF. We find that β_d in Eq.(3.66) contains additional $1/l_{sf}$ with respect to β in Eq.(3.40). We note that the difference between β and β_d become important only when $\rho^* l_{sf} \ll \mathcal{R}_{sh}$. It is known that polarization of spin current injected in a normal layer N from a ferromagnetic layer F is less than the polarization of spin current in the bulk of the ferromagnet F

$$\beta' = \frac{\beta}{1 + r_{sf_N}/r_{sf_F}}, \tag{3.71}$$

$r_{sf_N} = \rho_N l_{sf}$ being the resistivity of a normal layer within spin flip length and $r_{sf_F} = \rho_F^* l_{sf}$. If we plot the polarization of spin current in a layer of Permalloy as a function of position inside the layer see FIG. 3.4 we find that the polarization of spin current decreases towards the ends of the sample as having some normal layer outside as in Eq.(3.71). In fact Eq.(3.50) defining boundary conditions says that each spin channel of a magnetic conductor is connected to leads through the half of the Sharvin resistance $\mathcal{R}_{sh}/2$. The decrease of the spin current polarization occurs due to the spin accumulation near the contacts between the conductor and the leads. Using $r_{sf_N} = \mathcal{R}_{sh}/4$ and $r_{sf_F} = \rho^* l_{sf}$ we rewrite Eq.(3.71) in the following form:

$$\beta' = \frac{\beta}{1 + \mathcal{R}_{sh}/(4\rho^* l_{sf})}. \tag{3.72}$$

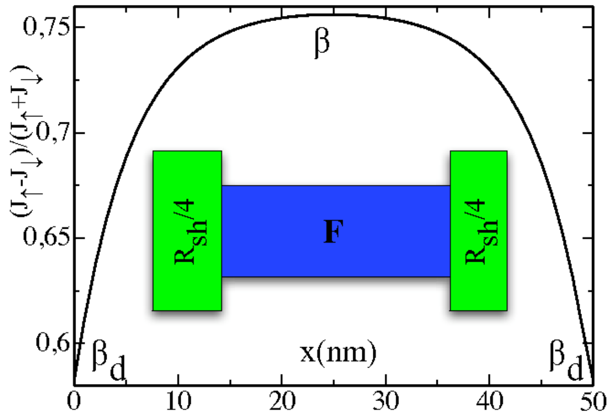

Figure 3.4: Polarization of the spin current inside a Py layer of length 50 nm. In the middle of the sample polarization of the spin current is equal to the β close to the ends it decreases due to the interface spin accumulation to the value defined by Eq.(3.72).

Using Eq.(3.70) we find that $\beta' = \beta_d$ of Eq.(3.69). This means solution of Eqs.(3.29,3.28) in $L \gg l_{sf}$ takes into account boundary conditions Eq.(3.50). If one defines VF parameters ρ^*, β, l_{sf} from the elements of $\hat{t}, \hat{r}$ using Eqs. (3.65,3.66,3.67) one has to take into account the difference between VF β and β_d for $L \gg l_{sf}$. This example shows the importance of the theory for the spin transport that takes into account Sharvin resistance $\mathcal{R}_{sh}$.

3.7 Applications of CRMT to the description of spin valves

We consider the valve depicted in FIG.(3.5a) and note $\vec{J}_A$, $\vec{J}_N$ and $\vec{J}_B$ the spin currents just before, in between and after the two magnetic layers F_A and F_B. For non collinear magnetization, spin current is not conserved and the spin torque on F_A and F_B is defined as,

$$\boldsymbol{\tau}_A = \boldsymbol{j}_A - \boldsymbol{j}_N, \quad \boldsymbol{\tau}_B = \boldsymbol{j}_N - \boldsymbol{j}_B \tag{3.73}$$

Let us start with a simple geometric construction that allows to get a physical picture for the torque in a rather general way. To do so, we need two hypothesis: (i) the mixing transmission are small (it is the case for metallic magnetic layers) so that $\boldsymbol{J}_A$ and $\boldsymbol{J}_B$ are parallel to the magnetization of F_A and F_B respectively. (ii) the system is thin enough for spin-flip scattering to be ignored in the active region so that $\vec{\tau}_A$ ($\vec{\tau}_B$) is perpendicular to $\boldsymbol{J}_A$ ($\boldsymbol{J}_B$). The construction goes as follows, see FIG.(3.5b) and (c): first we

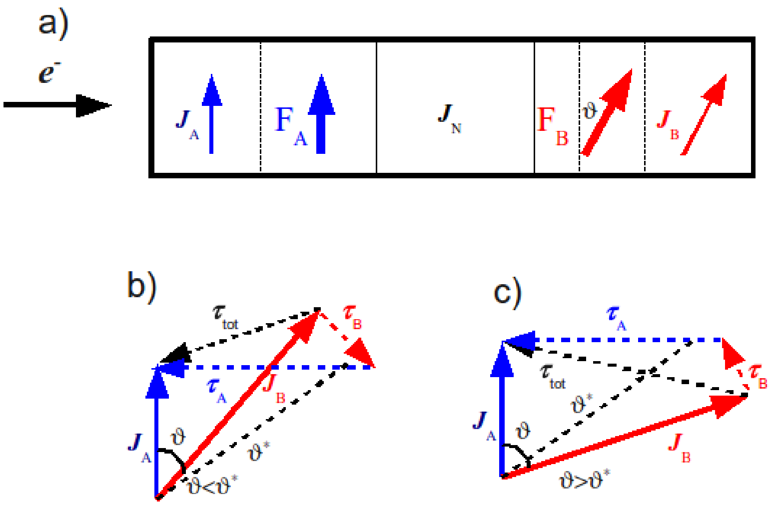

Figure 3.5: (a) Schematic of a spin valve with two ferromagnetic layer F_A and F_B whose magnetization makes an angle θ. (b) and (c): geometric construction of the spin torque, see text. $\vec{J}_A$, $\vec{J}_N$ and $\vec{J}_B$ are the spin currents along the valve while $\vec{\tau}_A$ and $\vec{\tau}_B$ are the torque on the two magnetic layers.

plot $\boldsymbol{J}_A$ and $\boldsymbol{J}_B$ which make the same angle θ as the magnetization of the respective magnetic layers. Then, we note that $\boldsymbol{\tau}_{tot} \equiv \boldsymbol{\tau}_A + \boldsymbol{\tau}_B = \boldsymbol{J}_A - \boldsymbol{J}_B$ does not depend on the unknown $\boldsymbol{J}_N$ and points from the tip of $\boldsymbol{J}_B$ to the tip of $\boldsymbol{J}_A$. The construction of the torque is then straightforward: the two vectors $\vec{\tau}_A$ and $\vec{\tau}_B$ are chosen such that they are perpendicular to their respective layer and their sum goes from the tip of $\boldsymbol{j}_B$ to the tip of $\boldsymbol{J}_A$. This simple construction gives, in particular, the sign of the torque as a function of the angle θ. We find that when, say, $J_B > J_A$ the torque on the layer with the highest polarization (F_B) can become wavy [65, 41, 71], *i.e.* instead of favoring the parallel or antiparallel configurations, the torque stabilizes (or destabilizes depending of the direction of the current) a configuration with a finite angle θ^*. The critical angle θ^* where the torque vanishes verifies $|J_A/J_B| = \cos\theta^*$. On the other hand, at small angle, one has the following development $|J_A/J_B|(\theta) = 1 - \eta\theta^2/2 + \ldots$ (Current conservation imposes $J_A = J_B$ at $\theta = 0$ and the ratio is an even function of θ) so that "waviness" is found when $\eta > 1$. In a symmetric structure $\eta = 0$, so that a finite asymmetry is needed to enforce waviness.

Without spin-flip scattering, we find

$$\eta = [\gamma_B r_B^* - \gamma_A r_A^* + (\gamma_B - \gamma_A) r_A^* r_B^* / \mathcal{R}_{\text{sh}}] / (\gamma_B r_B^* + \gamma_A r_A^*) \tag{3.74}$$

where the effective parameters γ_A and r_A^* include both the interface and bulk properties of layer A. More generally, the crossover between normal

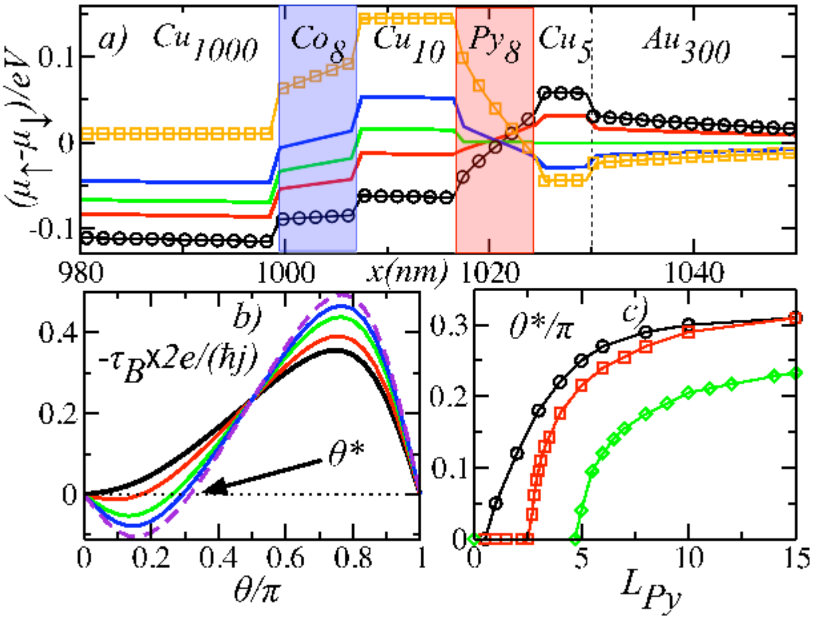

Figure 3.6: a) Spin accumulation in the middle of a spin valve A = $Cu_{1000}Co_8Cu_{10}Py_8Cu_5Au_{300}$ (thickness in nm) for different angle $\theta = 0$ (circles),$\pi/4$, $\pi/2$, $3\pi/4$ and π (squares). Symbols stand for VF calculations while lines correspond to C-RMT. b) torque $\tau_B(\theta)$ (per total current j) on the Py-layer of A for various Py-thickness L_{Py} from 0.5nm (thick) to 15nm (dashed). c) Stability angle θ^* as a function of L_{Py} for A (circles), B = $Cu_{1000}Co_8Cu_{10}Py_{L_{Py}}Cu_{1000}$ with $\delta = 0$ (squares) and B with $\delta_{CoCu} = \delta_{CoPy} = 0.25$ (diamonds).

and wavy can be discussed by looking at the small angle expression derived by Fert et al [Eq.(5) in [36], we omit the ballistic corrections]. It can be obtained by relating the spin accumulation in the spacer for $\theta \ll 1$ to spin current and spin accumulation at $\theta = 0$, and then applying Eq.(3.55). It reads,

$$\frac{d\tau_B}{d\theta}|_{\theta=0} = -\frac{\hbar}{e}\left[\frac{j_\uparrow - j_\downarrow}{4}|_{\theta=0} + \frac{\mu_\uparrow - \mu_\downarrow}{2e\mathcal{R}_{\text{sh}}}|_{\theta=0}\right] \tag{3.75}$$

When, for instance, one crosses the assymetry border from $J_A > J_B > 0$ to $J_B > J_A > 0$, the spin accumulation, proportional to the gradient of the spin current, changes from negative to positive and the second term in Eq.(3.75) becomes negative and begins to compensate the first one. The crossover from normal to wavy occurs when, by a further increase of assymetry, the spin accumulation term wins and reverse the sign of $d\tau_B/d\theta|_{\theta=0}$ (see Gmitra and Barnaś [41] for an extensive discussion of the normal to wavy crossover).

Typical examples of our numerical results are presented in FIG. (3.6) for Co/Cu/Py samples in which the asymmetry comes from the short l_{sf} and large polarization and resistivity of Py. Starting from a small value of L_{Py}, an increase of the assymetry and finally a crossover to wavy ($\theta^* \neq 0$) can be obtained by increasing L_{Py} as shown in FIG. (3.6) (b) and (c). By comparing the curves in samples with and without Au on the right of the valve, one sees that the short l_{sf} of Au in a layer close to Py tends to increase the asymmetry and the waviness. On the other hand, interface spin-flip is found to favour a normal spin torque. In the experimental results of Boulle *et al.* [71] a wavy behaviour was found for Cu/Co/Cu/Py/Cu/Au structures with equal thicknesses (8 nm) for Co and Py.

Chapter 4

Effective quantum approach to magnetic multilayers

4.1 Introduction

In this chapter we develop a different approach to spin transport, which is based on the description of the system with an effective Hamiltonian for itinerant electrons, and allows for numerical computations of transport properties for systems with arbitrary shape and connected to an arbitrary number of leads.

In Sec.(4.2) we define the Tight Binding (TB) Hamiltonian of the system. According to this model, the conductor is represented as a network of sites, each sites representing one atom or a group of atoms, and electrons jump from one site to the other with some probability amplitude. An onsite potential as well as a spin-orbit interaction are taken into account do describe the resistance of the system due to impurities and spin flip phenomena. These phenomena can be described with a few free parameters, namely a "disorder" for majority and minority electrons, spin-orbit coupling and hopping between sites.

In Sec.(4.3) we show how to express hat matrices using Green's functions, via the Fisher-Lee formula [38].

In Sec. (4.4) we show numerical simulations of multilayers within the TB model. Computation of spin current and spin torque for different structures are shown. We have compared calculations performed with TB model and CRMT, and we have found a good agreement between these calculations, in the regime where Green's function formalism and RMT are equivalent (Ohmic conductors).

CRMT and TB approaches are different in performances (CRMT is faster) and in the range of physical phenomena they can describe (CRMT is purely one dimensional and semiclassical, while TB is fully three dimensional and can describe purely quantum systems, such as tunnel junctions or semiconductors). In this chapter we show how to combine these approaches to have a versatile and fast tool to describe quantum transport inside a great variety of systems. The idea behind what we have called a *multiscale approach* is simple: a system can be split into subparts. Each subpart can be described using CRMT or TB model, according to the physics one want to capture, and in order to minimize computational time. The outputs of CRMT and TB calculations will be in the end hat matrices of the subblocks of the system, that can be summed up to reproduce the transport properties of the system as a whole, according to the sum rule described in Sec.(2.4.1)

4.2 Effective tight binding Hamiltonian approach to spin transport

In this section, we take a completely different approach from the CRMT theory described in the previous chapter, and derive a full quantum mechanical approach. Such an approach is *a priori* very tempting as it allows to deal with many different systems (metals, tunnel junctions, magnetic semi-conductors...) within one unified framework and using only few approximations. However, for practical calculations, such a direct approach has a prohibitive numerical cost so that only very small systems can be studied, even for the minimum model that we will introduce below. Hence, instead of a full quantum general treatment, we focus on two goals: (i) we want to study the validity of CRMT theory as well as deviations coming from quantum effects. (ii) Certain systems cannot be treated accurately within CRMT. It is the case for instance of tunneling junctions which are intrinsically quantum (CRMT being a spin extension of Ohm law, it cannot describe an exponential suppression of the resistance). For those systems, we want to provide a purely quantum description of the pieces that require it (for instance the oxide layers) to obtain effective boundary conditions while the rest of the system is described by CRMT. This is the way we implement the multiscale description of our system.

The starting point of our quantum approach is the choice of the Hamiltonian of the problem. Here we consider a tight binding (TB) Hamiltonian parametrized to reproduce the main bulk and interface properties of a few diffusive magnetic and non magnetic metals. TB approximation is conceptually simple and suitable for numerical simulations, since it is intrinsically discrete. There are several way one can derive a TB Hamiltonian for magnetic multilayers. For instance, one can use multi-orbital ($s, p, d...$) models where each site of the TB model corresponds to an atom and where all the on site energies and hopping amplitudes are parametrized to reproduce *ab-initio* calculations. When one is interested in transport properties however, one is not interested in a model that reproduces the entire band structure of a material, but only what happens around the Fermi level. Here, we take an

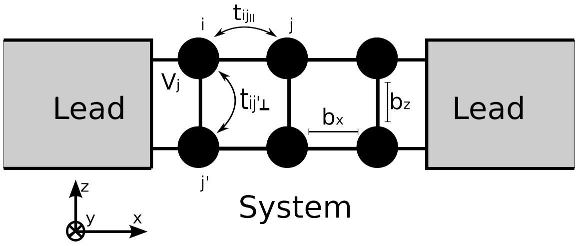

Figure 4.1: A cartoon representing a conductor described by the TB model, with hopping t_{ij}, disorder V_i and intersite distances b_y and b_z. Hopping can have an additional term t^{so} that mix spin up and down channels and describes spin-orbit interaction. The system is connected to two leads.

even more limited approach: we construct our model such that it correctly reproduces the five characteristic length scales that were introduced in the previous chapters (mean free path for majority ($l_\uparrow$) and minority ($l_\downarrow$) electrons, spin-flip diffusion length (l_{sf}), transverse penetration length ($l_\perp$) and Larmor precession length (l_L)). This quantum model can hence be viewed as an effective approach valid for diffusive metals, but many features described below do not depend on the specific details of the model. The simulations shown in this chapter have been performed using the KNIT package [53, 80].

We discretize the inner space of a 3D conductor by introducing a cubic lattice of intersite distances $\boldsymbol{b}(b_x, b_y, b_z)$ [See FIG.(4.1)], and we consider electronic wave functions localized in the nodes of the lattice. Each node may represent one atom, or a group of atoms. The general TB Hamiltonian for electrons in a 3D lattice reads.

$$H = -\sum_{<i,j>} c_i^\dagger t_{ij} c_j - \sum_{<i,j>} c_i^\dagger t_{ij}^{so} c_j + \sum_i c_i^\dagger V_i c_i \tag{4.1}$$

Here the summation is taken over all the nearest neighbour sites $< i, j >$, and $(c_i^{\sigma\dagger}, c_i^\sigma)$ are the usual creation and annihilation operators for the electrons. The indexes i, j stand for position in the lattice, while the index $\sigma =\uparrow / \downarrow$ refers to spin.

The first term of the Hamiltonian is the matrix

$$t_{ij} = \begin{pmatrix} t_\parallel + t_\perp & 0 \\ 0 & t_\parallel + t\perp \end{pmatrix}, \tag{4.2}$$

that represents the amplitude for an electron with spin up or down to jump on neighbour sites on the lattice.This matrix depends on the material and fixes the band structure. The coefficients $t_\parallel$ and $t_\perp$ are the hopping along the multilayer growth direction x and the transverse directions (y, z) correspondingly. Allowing for different $t_\parallel$ and $t_\perp$ is advantageous in the simulations: it allows for different discretization steps in the x direction and y, z plane. Also, by taking $t_\perp$ significantly smaller than $t_\parallel$, one ensures that the number of propagating channels is maximum and constant over a large window of energy, hence reducing mesoscopic effects. On the other hand, the model acquires some intrinsic anisotropy not present in the original materials, so that the physical meaning of the calculations is doubtful outside the quasi-one dimensional geometry considered here

The second term in the Hamiltonian represents the scattering potential for electrons with different spins:

$$V_i = v_i \begin{pmatrix} W^\uparrow & 0 \\ 0 & W^\downarrow \end{pmatrix}. \tag{4.3}$$

Electrons with different spin σ feel the same profile of the disorder defined by random numbers v_i distributed according to the uniform distribution with $v_i \in [-0.5, 0.5]$, but with different strength W^σ. A different resistance for up and down spin can be simulated also assigning a different hopping for the two spin channels.

Since the system we study is diffusive, its resistance is proportional to the inverse of the elastic mean free time τ_{el} of the electrons [26]. According to the Fermi golden rule, this is related to the onsite potential via

$$\frac{1}{\tau_{el}} = \frac{2\pi}{\hbar}\overline{|\langle|k|V_i|k'|\rangle|^2}\,\overline{\nu}(E_f), \tag{4.4}$$

where $\overline{\nu}(E_f)$ is the density of states per site at the Fermi level. Here we consider V_i uniformly distributed in the interval $[-W/2; W/2]$, so that $\overline{|\langle k|V_i|k'\rangle|^2} = W^2/12$ [2]. The resistance is though proportional to W^2.

The last term t_{ij}^{so} introduces some spin-orbit interaction responsible for a finite spin-flip scattering length. Its spin structure respects time-reversal symmetry and is given by,

$$t_{ij}^{so} = W_{so} \begin{pmatrix} \xi_{ij} & -\eta_{ij}^* \\ \eta_{ij} & \xi_{ij}^* \end{pmatrix}, \tag{4.5}$$

where the elements of the matrix are random complex numbers distributed according to the gaussian distribution, with $\overline{\eta_{ij}^2} = \overline{\xi_{ij}^2} = 1$. Different pairs of nearest neighbours have independent values of η_{ij}^2 and ξ_{ij}^2. W_{so} represent the strength of spin orbit interaction. The parameters $t_\parallel^\sigma$, $t_\perp^\sigma$, $W^{\uparrow,\downarrow}$ and W^{so} which define the TB-model allow to tune the different characteristic lenghs that have been introduced before.

In order to complete the model, the above bulk model has to be extended to describe interfaces properties. Interfaces are represented as hopping elements that link the sites of two different materials. In this view, an interface acts as a potential barrier between two adjacent materials, and does not contain any disorder or spin orbit interaction. The Hamiltonian that describes interfaces is thus simply given by

$$H_{int} = -\sum_{i,j} \boldsymbol{c}_i^{\dagger} t_{ij}^{int} \boldsymbol{c}_j \tag{4.6}$$

where the indexes i, j belong to the sites of the adjacent materials, and the matrix t_{ij}^{int} is given by

$$t_{ij}^{int} = \begin{pmatrix} t_{\uparrow} & 0 \\ 0 & t_{\downarrow} \end{pmatrix}, \tag{4.7}$$

4.2.1 Dispersion relation of the TB Hamiltonian

We consider first the one dimensional case, the generalization to a three diimensional conductor being straightforward. Suppose that one has a uniform 1D wire with a constant potential V, then the eigenfunctions are plane waves $\psi_k(x) = e^{ikx}$ with the parabolic dispersion relation $E = V + \hbar^2 k^2/2m$. For a discrete wire with lattice constant b and lattice sites indexed by j, the Schroedinger equation is the finite different equation [26]

$$E\psi_j = (V + 2t)\psi_j - t\psi_{j-1} - t\psi_{j+1} \tag{4.8}$$

which is satisfied by a solution of the form $\psi_j = e^{ikx_j}$, $x_j = jb$. Substituting this solutions into Eq.(4.8) gives the dispersion relation

$$E = V + 2t(1 - \cos(kb)), \tag{4.9}$$

from which one obtains the electron velocity $v = \frac{\partial E}{\partial k} = 2bt\sin(kb)$. The generalization to the 3D case reads

$$E(k_x, k_y, k_z) = 2[t_{\parallel}\cos(k_x b_x) + t_{\perp}(\cos(k_y b_y) + \cos(k_z b_z))], \tag{4.10}$$

which defines one conduction band of width $6t$. We have introduced two different hoppings $t_{||}, t_{\perp}$ for longitudinal (x) and transverse (y, z) directions correspondingly. The reason for this choice shall be specified soon.

In our simulations we have considered a parallelepiped-shaped system, with $\mathcal{L}$ sites in the x direction, and M sites in the y and z directions. Electron current propagates between the leads in the x direction.

Since the electronic wavefunctions vanish outside the system, the transverse wave vectors k_y and k_z are quantized, and may assume only the values $n_y\pi/(M_y + 1)$, and $n_z\pi/(M_z + 1)$ for the y and z directions correspondingly with n_y (n_z) entire numbers between 1 and M_y (M_z). The modes corresponding to real value of $\vec{k}$ determined by Eq. (4.10) are called *propagative channels*, and are exactly the same as the channels of the scattering theory (see chapter 3).

4.2.2 Length-scales, energy and hopping

Eq. (4.10) shows that, at fixed energy E, if the hopping in the longitudinal and transverse directions are the same, not all the channels are open, while setting $t_\parallel$ between 1 and 3 and $t_\perp = 0.4$, allows one to open all the $M_y \times M_z$ modes at $E \approx 0$ (for this reason all our simulations have been performed at zero energy).

Due to computational difficulties, if we use a model in which one lattice site corresponds to one atom, we would be able to make numerical calculations on samples with size of 10-15 nm. In our simulations it is not necessary to consider one site as one atom. The lattice constant should be smaller than the relevant length scales of the problem: the elastic mean free path for majority and minority spins l_σ, and the spin flip length l_{sf}.

For the materials widely used in experiments these length are of the order of 10-100 nm [44, 109]. Besides,the magnetization of a 3D multilayer system varies on the length scale of about 2-5 nm [81], and the discretization length of our systems should be smaller than this quantity. In all the simulations we have taken a lattice constant b=1 *nm*. This allows us to make numerical calculations on experimentally relevant samples, with sizes of about 200 nm.

4.3 Green's function and hat matrices

The typical output of TB calculations is given in term of the retarded Green's function G of the system. In this short section we show that G is related by the Fisher-Lee formula [38] to the scattering matrix. In particular, we are going to derive an explicit formula for the hat matrices described in section 2.4.2, in terms of the Green's functions of the system. The Fischer-Lee formula reads

$$t^{nm}_{\sigma\eta} = \sqrt{v_n v_m} \sum_{ij} \chi^{n*}_{\sigma i} G_{\sigma i,\eta j} \chi^{m}_{\eta j}, \tag{4.11}$$

$$r^{nm}_{\sigma\eta} = -\delta_{nm} + i\sqrt{v_n v_m} \sum_{ij} \chi^{n*}_{\sigma i} G_{\sigma i,\eta j} \chi^{m}_{\eta j}. \tag{4.12}$$

where $t^{nm}_{\sigma\eta}$ and $r^{nm}_{\sigma\eta}$ are transmission and reflection amplitudes between the spin state η in channel m and the spin state σ in channel n; v_m (v_n) are the velocities of an electron in channels m (n); χ^{η}_{mi} is the value of the transverse wave function of the m-th mode in the i-th site with spin η; $G_{\sigma i,\eta j}$ is the value of the retarded Green function between the spin state η at the j-th site and spin state σ at the i-th site. The summation is taken over interface sites (i, j) which are on the border between the system and a lead. Note that in general the size of the transmission/reflection matrices $2N_{ch} \times 2N_{ch}$ is smaller than the total number of transverse sites, but in our numerical simulations we will always take the transverse and longitudinal hopping in a way that N_{ch} is equal to the number of transverse sites $M_y \times M_z$. The imaginary part of the self energy Γ, due to the presence of the leads, reads

$$\Gamma_{ij}^{\sigma\eta} = \sum_n v_n \chi_{ni}^{\sigma} \chi_{nj}^{\eta\dagger}. \tag{4.13}$$

In a normal metallic lead an electron wave function has no spin dependence thus Γ has no spin degree of freedom: $\Gamma_{ij} = \sum_n v_n \chi_i^n \chi_j^{n*}$

In order to calculate $\hat{t}$ and $\hat{r}$ for a system we use Eqs.(4.11) and (4.12). An arbitrary element of $\hat{t}$ is given by:

$$T_{\sigma'\sigma\eta'\eta} = \frac{1}{N} \mathrm{Tr}_{Nch} \left(\Gamma G_{\sigma'\sigma} \Gamma G_{\eta'\eta}^{\dagger} \right). \tag{4.14}$$

Here the trace is taken over the transverse sites, N_{ch} is total number of channels in a lead, and $G_{\sigma'\sigma}$ is the Green function matrix with elements $G_{\sigma' i,\sigma j}$. In the same way we obtain elements of $\hat{r}$:

$$\begin{aligned} R_{\sigma'\sigma\eta'\eta} &= \delta_{\sigma\sigma'}\delta_{\eta\eta'} + \frac{i}{N}\delta_{\sigma\sigma'} \mathrm{Tr}\left(\Gamma G_{\eta'\eta}^{\dagger}\right) + \\ -\frac{i}{N}\delta_{\eta\eta'} &\mathrm{Tr}\left(\Gamma G_{\sigma'\sigma}\right) + \frac{1}{N}\mathrm{Tr}\left(\Gamma G_{\sigma'\sigma} \Gamma G_{\eta'\eta}^{\dagger}\right) \end{aligned} \tag{4.15}$$

These results show that Green function formalism and random matrix theory describe quantum transport in an equivalent way (for Ohmic conductors). Once one has computed the Green's function of a system, one can calculate the scattering matrix of the system, and obtain conductance and spin current in terms of hat matrices, as shown in Sec.(2.4.2) and (2.4.3).

4.4 Numerical study of multilayers within the TB model

Numerical simulations using the KNIT package [53, 80] are performed in the following way: first we create a network of sites with a given shape and connected to some leads, then we define the TB Hamiltonian of the system, and we compute the corresponding retarded Green's function using KNIT. Finally, conductance is calculated from hat matrices using the Fisher-Lee relation described in the previous section, and spin current is calculated using the fomulas described in section (2.5.2).

The KNIT package allows us to compute the properties of bulk, multilayers, and interfaces alone, and it can be used to describe quantum system for which CRMT is not adequate (such as tunnelling of electrons through an insulator separating two ferromagnets). It is also an excellent way to test the addition law of hat matrices defined in Sec.(2.4.1), and CRMT itself (since it comes from an application of the addition law). The standard way to test the addition law of hat matrices will be the following: first we use KNIT to compute the hat matrix of a given system (*i.e.* a FNF multilayer), and we get conductance and spin torque, then we divide the system into subblocks and we use KNIT to compute the hat matrices of each subblock. If we sum up these matrices using the addition law [Sec.(2.4.1)] we should obtain the spin current in both cases.

CRMT can be used to map the parameters of the TB model $t^{\sigma}_{\parallel,\perp}$, $W^{\uparrow,\downarrow}$, W^{so} and $\boldsymbol{b}$ onto Valet-Fert parameters ρ^{*}, β, l_{sf} and $l_{\perp}, l_{mx}$ for a given material. Both CRMT and KNIT have advantages and drawbacks: KNIT is more flexible and describes fully quantum effects in three dymensional systems, but is slow, the computation time scaling as $M_y \times M_Z$; on the other hand CRMT is fast (computation time proportional to the logarithm of the length of the system), but is semiclassical and completely one dimensional.

A real avantage in simulation performances can be achieved if *both CRMT and KNIT work together.* in what we use to call a multiscale approach to spin transport. The idea is the following: we use CRMT to compute the parts of the system that can be treated in a semiclassical way, while KNIT is used to compute the fully quantum parts of the system (tunnel junctions etc.). Since both KNIT and CRMT have a hat matrix as output, the hat matrix of the system as a whole is obtained additioning the hat matrices of each subblock according to the sum law described in section (2.4.1).

4.4.1 Numerical study of the bulk

Let us perform a numerical study of our TB model starting from the properties of the bulk. The quantity of interest are the intrinsic total resistance R^{σ}_{I} for spin σ,

$$\frac{R^{\sigma}_{I}}{\mathcal{R}_{\text{sh}}} = \frac{1}{T_{\uparrow\sigma} + T_{\downarrow\sigma}} - 1, \tag{4.16}$$

which is related to the transmission matrix $\hat{t}$ of the system via the Sharvin resistance $\mathcal{R}_{\text{sh}}$; and the polarization of the current transmitted P^{σ}_{I} upon sending polarized electrons along $\sigma = \uparrow, \downarrow$ direction:

$$P^{\sigma}_{I} = \frac{T_{\uparrow\sigma} - T_{\downarrow\sigma}}{T_{\uparrow\sigma} + T_{\downarrow\sigma}}, \tag{4.17}$$

the mixing transmission T_{mx} and the spin-flip probability $T_{\uparrow\downarrow}$. FIG.(4.2) and FIG.(4.3) show these quantities for two sets of parameters that correspond respectively to a normal (Au) and a magnetic (Py) material as a function of the thickness L of the sample. Together with the quantum calculations (symbols) we also plot the results of the CRMT calculations (lines). The latter is equivalent for this collinear case to the Valet Fert Ohmic theory.

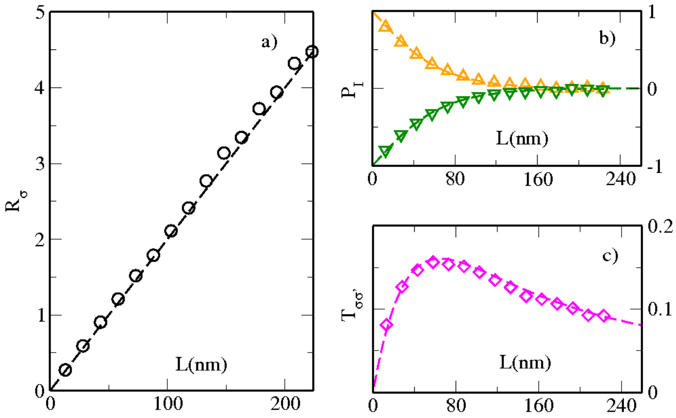

Figure 4.2: Comparison between TB (symbols) and CRMT (dashed lines) calculations for transport properties of a normal metal as a function of the thickness L of the sample. The parameters have been chosen to reproduce the properties of gold (Au). Left panel: intrinsic resistance $R_I^\uparrow(L) = R_I^\downarrow(L)$ in unit of the Sharvin resistance. Right upper panel: $P_I^\uparrow(L)$ (up triangles) and $P_I^\downarrow(L)$ (down triangles). Right lower panel: spin flip transmission probability $T_{\uparrow\downarrow}(L)$. These results have been averaged over 6 samples with different realizations of the disorder.

We find that our TB effective model reproduces extremely well the semi-classical results: the intrinsic resistance is indeed Ohmic ($R_I^\sigma = \rho^\sigma L$) and the polarization reaches its asymptotic value β_d after an exponential decay controlled by l_{sf}. Exact CRMT expressions for $P_I^\sigma(L)$ are cumbersome but amount with good precision to

$$P_I^\sigma(L) \approx \beta_d - (\beta_d \pm 1)e^{-L/l_{sf}} \tag{4.18}$$

which is well verified by the TB quantum data. For magnetic material, T_{mx} is also found to decay exponentially with a characteristic length of few nanometers, as expected. Such an agreement between the TB model and CRMT allows to use the experimentally measured CRMT (Valet Fert) parameters to tabulate the TB model. The corresponding parameters can be found in Table 4.4.1. We note that the polarization saturates towards β_d which differs slightly from the Valet-Fert definition of, due to the depolarizing role of the Sharvin resistances [Sec.(3.6)].

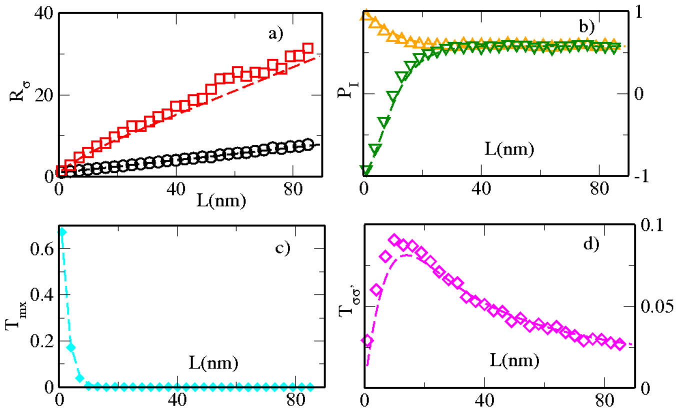

Figure 4.3: Comparison between TB (symbols) and CRMT (dashed lines) calculations for transport properties of a magnetic metal as a function of the thickness L of the sample. The parameters have been chosen to reproduce the properties of permalloy (Py). Left upper panel: intrinsic resistance $R_I^{\uparrow}(L)$ (circles) and $R_I^{\downarrow}(L)$ (squares) in unit of the Sharvin resistance. Left lower: mixing transmission $T_{mx}(L)$. Right upper panel: $P_I^{\uparrow}(L)$ (up triangles) and $P_I^{\downarrow}(L)$ (down triangles). Right lower panel: spin flip transmission probability $T_{\uparrow\downarrow}(L)$. These results have been averaged over 6 samples with different realizations of the disorder.

Material	$\rho*$	β	$1/l_{sf}$	$W_{\uparrow}$	$W_{\downarrow}$	W_{so}	$t_{\parallel\uparrow}$	$t_{\parallel\downarrow}$	$t_{\perp}$
Cu	5	0	0.002	0.45	0.45	0.0055	1	1	0.4
Au	20	0	0.033	0.7	0.7	0.042	1	1	0.4
Co	75	0.46	0.017	4.1	2.05	0.022	3	1	0.4
Py	291	0.76	0.182	3	4.6	0.11	2	1	0.4

Table 4.1: Bulk TB parameters for a few metals. Valet Fert resistivity ρ^* is measured in units $10^{-9}\Omega m$ and spin-flip length in nm. The discretization length b_z is equal to $1nm$. These parameters have been obtained averaging the calculation of the resistance over 6 samples with different realizations of the disorder.

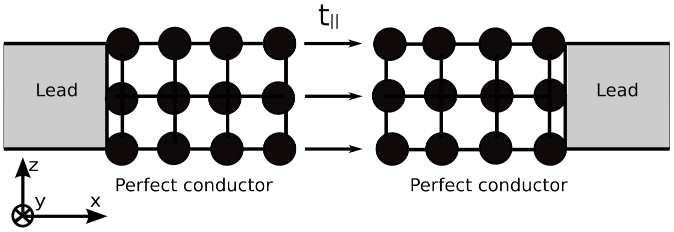

Figure 4.4: Schematic of two perfect conductors glued toghether with the hopping element $t_{||,ij}$, which connects sites i and j belonging to the left and right conductor correspondingly, that have the same y and z coordinates.

Interface	$r_b^*(10^{-15}\Omega m^2)$	γ	$t_\uparrow$	$t_\downarrow$
$Au\|Co$	0.5	0.77	1.257	2.2
$Cu\|Co$	0.51	0.77	1.253	2.21
$Cu\|Py$	0.5	0.7	0.99	2.17
$Au\|Py$	0.5	0.77	1.257	2.2
$Au\|Cu$	0.5	0	1.86	1.86

Table 4.2: TB parameters for a few Normal-Ferromagnetic interfaces. We find parameters of TB model using CRMT parameters for the interfaces Eq.(3.43). The discretization length b_z is equal to $1nm$.

4.4.2 Interface properties of the TB model

A similar study can be performed for interfaces properties. In this case, the quantity of interest is the interface resistance R^σ_{int} for spin σ,

$$\frac{R^\sigma_{int}}{R_{sh}} = \frac{1}{T_{\sigma\sigma}} - 1 \tag{4.19}$$

where $T_{\sigma\sigma}$ represents the transmission probability of the interface. An interface can be simulated as follows: we build two perfectly conducting systems and we "glue" them together via a hopping $t_{\uparrow(\downarrow)}$ [see FIG.(4.4)]. In this way the resistance of the system is determined only by the hopping, which describes the properties of the interface.

The resistance has been calculated as a function of $t_{\uparrow(\downarrow)}$ and fitted with simple functions[FIG.(4.5)]. Knowing how the interface resistance varies as a function of the hopping allows us to use the Valet Fert experimentally measured parameters to tabulate the TB model for the interfaces, as we have done with the bulk. The TB parameters calculated for some materials are shown in Table 4.4.2.

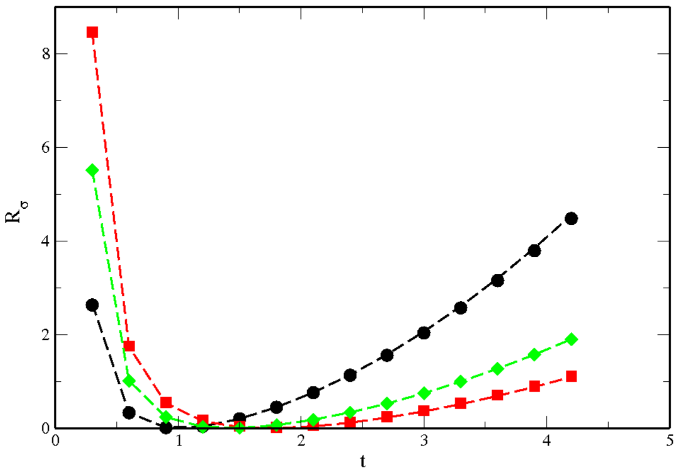

Figure 4.5: Resistance of the interface as a function of the hopping t between two adjacent materials, expressed in units of Sharvin resistance. The interface resistance is different if the adjacent materials have different hopping. Red squares represent the interface resistance for 'up' spin between two materials with $t_{\parallel\uparrow} = 3$ and $t_{\parallel\uparrow} = 1$ correspondingly. the points fit the function $R_{\uparrow} = 0.09 \times (t^2 - 3)^2/t^2$. Green diamonds represent the interface resistance for 'up' spin between two materials with $t_{\parallel\uparrow} = 2$ and $t_{\parallel\uparrow} = 1$ correspondingly. the points fit the function $R_{\uparrow} = 0.14 \times (t^2 - 2)^2/t^2$. Black circles represent the interface resistance for 'up' or 'down' spin between two materials with the same hopping $t_{\parallel\uparrow(\downarrow)} = 1$. the points fit the function $R_{\uparrow(\downarrow)} = 0.29 \times (t^2 - 1)^2/t^2$.

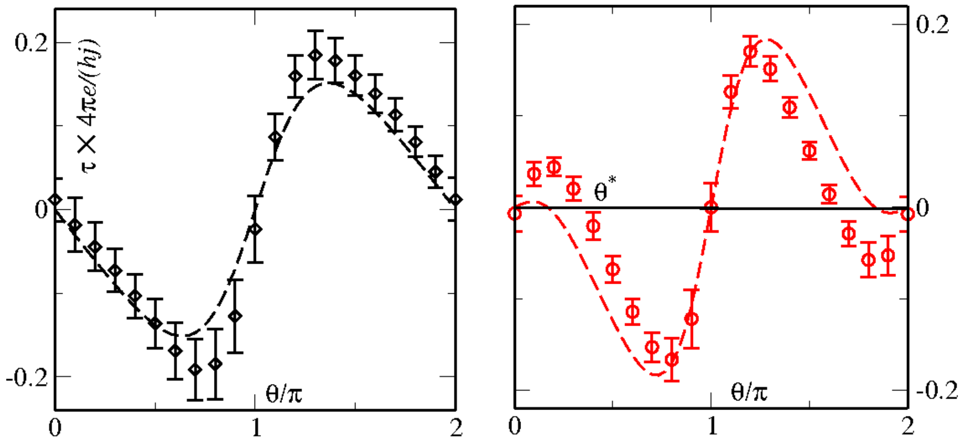

Figure 4.6: Comparison between TB (symbols) and CRMT (dashed lines) calculations for the angular dependence of the spin torque τ exerted on the ferromagnet at the right hand side of the stack. Left panel: $Cu_5Py_{20}Cu_5Py_{20}Cu_5$ multilayer (length in nm). Right panel: $Cu_{159}Co_8Cu_{10}Py_8Cu_4$ which shows a wavy behaviour.

4.4.3 Comparaison between CRMT and TB for a spin valve.

Now that our model is fully tabulated and that we have checked that all individual pieces (bulk and interfaces) agree with CRMT theory, we can go ahead and perform quantum calculation for entire spin valves. The results are presented in FIG.(4.6) where we calculate the spin torque τ (defined as the difference of spin current on the two sides of the free ferromagnet [88, 103]) as a function of the angle θ between the magnetization of the two magnetic layers. Two different stacks are presented (lengths in nm): $Cu_5Py_{20}Cu_5Py_{20}Cu_5$ (left panel) and $Cu_{159}Co_8Cu_{10}Py_8Cu_4$ (right panel). The first one is symmetric and shows a usual $\tau \propto \sin\theta$ torque. The CRMT and TB calculations are in close agreement. For the second stack which is assymetric, we find a good agreement of the torques, except at small angle where the the TB calculation shows a strong deviatin from the $\sin\theta$ behaviour. As a result, the TB torque vanishes for a finite value $\theta = \theta^*$ and the corresponding structure is wavy [See Sec.(3.7)]. The corresponding CRMT calculation is close, but below, to the wavy instability threshold. This small discrepancy already indicates a weakness of the effective TB approach as its physics is fairly sensitive to the choice of TB parameters.

To proceed further, we consider the symmetric $Cu_5Py_{20}Cu_5Py_{20}(\theta)Cu_5$ stack and compute the spin current inside the sample as a function of the position x along the stack. Once again, we observe a very good agreement between the two approaches. However, this new calculation points to another weakness of the TB approach: the error bars in the TB calcula-

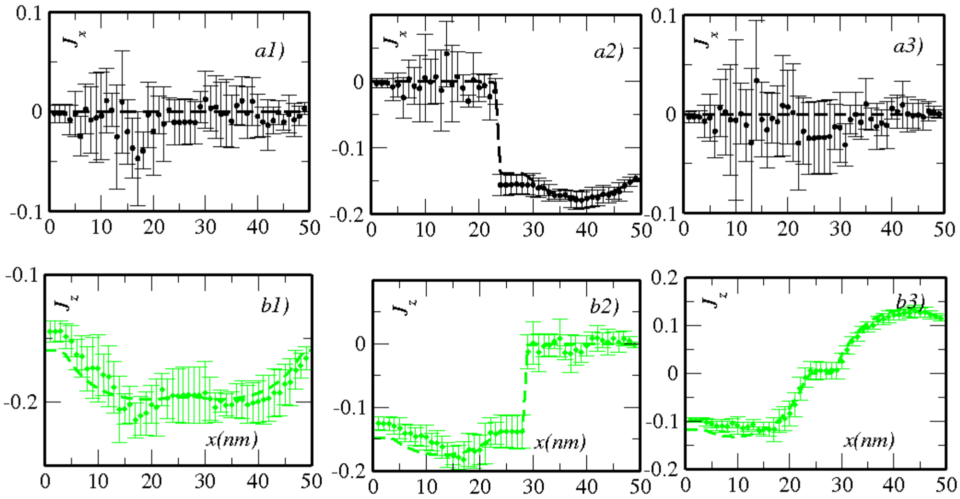

Figure 4.7: Comparison between TB (symbols) and C-RMT (dashed lines) calculations for the polarization of the spin current inside the $Cu_5Py_{20}Cu_5Py_{20}(\theta)Cu_5$ stack. Magnetization of the second Py layer is rotated around in XZ plane, while the first one point in the Z direction. Left, middle and right panels stand for $\theta = 0, \pi/2$ and π respectively. Upper (Lower) panels shows the spatial x dependence of the spin current $j_x = J_x/I$ ($j_z = J_z/I$) along the X (Z) direction.

tion correspond to the mesoscopic fluctuations upon averaging on different samples (typically 10 in those calculations). Real spin valves nano pillars typically have $N_{ch} \approx 10^4$ channels so that mesoscopic fluctuations $\approx 1/N_{ch}$ are negligeables. Our TB calculations are performed with typically $50 - 100$ channels, hence do show significant sample to sample fluctuations so that quantitative correspondance with CRMT calculations are only obtained after averaging over different disorder configurations.

To conclude this section, we have found an extremely good agreement between the TB approach and the CRMT approach even in regimes where it was not really expected: the derivation of CRMT assumes that the different channels are ergodically mixed, which is only achieved when the typical thickness of the layers is large compared to their mean free path. In that sense, the present TB results can be viewed as a proof of the robustness of the CRMT approach as good agreement is also obtained in fairly transparent regimes. On the other hand, as the TB calculations are numerically much more demending than CRMT, practical calculations are best performed with the latter approach which do not suffer from mesoscopic fluctuations. However, for certain systems (such as tunneling barriers) CRMT alone fails. In these cases, a multiscale combination of both approaches will be very effective.

Chapter 5

Magnetization Dynamics

5.1 Introduction

In the next two chapters we make a thorough attempt to perform SW spectroscopy inside a normally magnetized nano-pillar composed by the stack of two dynamically coupled magnetic disks. Its scope encompasses devices allowing transfer of spin angular momentum or electrical charge between the two magnetic layers by applying a current across the nano-pillar. Our main objective has been to provide a comprehensive identification of the SW eigen-modes inside a spin-transfer nano-oscillator but more generally to provide an experimental method to study the magnetization dynamics in spin-valve structures, where one expects the phenomenological Landau-Lifschitz-Gilbert equation to be complemented by the additional Slonczewski-Berger term. By using the CRMT model developed in the previous chapters and introducing it inside a micromagnetic simulation code, this allows to make simulations, where the 3D texturing of the transport and magnetization dynamics is taken on an equal footing.

From the experimental side, our study rely on independent method of detecting the magnetic resonance inside a spin-valve nanostructure. Our main tool has been a Magnetic Resonance Force Microscope (MRFM) [112, 101, 48, 23, 60], which detects *all* the excited SW modes independently of their phase [29, 70]. It has allowed us to perform SW spectroscopy in the exact normal configuration, which is the simplest possible geometry for a STNO as it coincides with the universal oscillator model [85]. It also illustrates the performance of this novel technique [32, 74, 75] to study the dynamics of small buried objects. The review actually permits a direct comparison of its sensitivity compared to voltage-FMR, where one detects the voltage drop produced across the STNO by SW excitations. It shows that the MRFM sensitivity allows the detection of precession angle as low as 1° in the thin layer, which is about the sensitivity achieved here by rectification effects.

In this chapter we shall describe the equation of motion of the magnetization, and the different terms that can be included in such equation to describe the effect of an external perturbation of the magnetization.

Sec.(5.2) gives a brief introduction to ferromagnets and to the Landau-Lifshitz-Gilbert (LLG) equation [62, 40], which describes the dynamics of the magnetization in ferromagnets. The terms of this equation that account for external perturbations of the magnetization are described in Sec.(5.3). In particular, we describe how to introduce the effect of rf field, rf current and dc current in the equation of motion. In the previous chapters we have seen how to calculate spin torque in a general way, here we see how spin torque acts on the magnetization, according to the Slonczewski-Berger model [88, 9].

Sec.(5.4) is devoted to the description of spin wave modes inside a perpendicularly magnetized cylindrical nanopillar. An analytical description allows to classify SW modes in this simple geometry. Spin torque effect and spin wave classification are the cornerstone on which next chapter is built: starting from this description, we are going to define selection rules for spin wave modes, based on the symmetry of the different excitations. Experiment and simulations of chapter 6 are devoted to the understanding of those rules.

5.2 The Landau-Lifshitz-Gilbert (LLG) equation

Ferromagnets are substances that contain elementary magnetic moments, which are spontaneusly ordered below a certain temperature called Curie Temperature T_C. The elementary magnetic moments in ferromagnets are due mainly to the electronic spins, and exchange interaction is responsible for the alignment of the spins in the same direction. This alignment may create a macrospopic magnetic field. Because of dipolar interaction, a magnetic material is usually divided into regions, called magnetic domains, where the magnetic moments point in the same direction. Usually the direction of the magnetic moments inside the domain varies from one domain to the other, so that the macroscopic magnetic stray field may vanish. A schematic of magnetic ordering and magnetic domains in a ferromagnet is shown in FIG.(5.1).

The local elementary magnetic moments $\mathcal{M}_S$ are associated to the spin operator $\boldsymbol{S}$ via the relation $\mathcal{M}_s = -(g\mu_B/\hbar)\boldsymbol{S}$, where g is the Lande factor, whose value for a free electron is close to 2, $\mu_B = e\hbar/2m_e$ is the Bohr magneton expressed in S.I. units, m_e is the electron mass, while the minus sign shows that magnetic moment and spin are antiparallel.

The collective precession of spins inside a ferromagnet involves a huge number of electrons in a small volume, and can be naturally described introducing a continuous magnetization vector field $\vec{M}(\boldsymbol{r}, t)$, instead of taking into account the individual atomic moments. The magnetization vector is

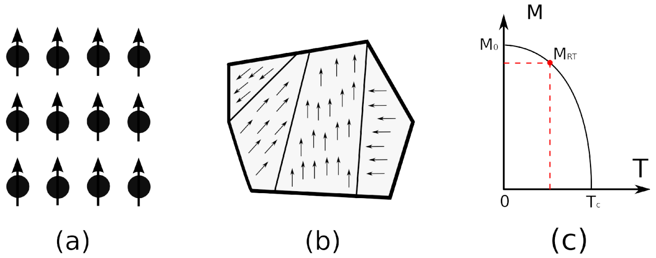

Figure 5.1: (a) Alignment of the localised spins of electron in a ferromagnet, due to exchange interaction. (b) Schematic of a ferromagnet divided in magnetic domains. (c) Spontaneus magnetization as a function of temperature. The magnetization decreases as a function of temperature, and vanishes at the Curie temperature T_C. Our experiments are performed at room temperature, where the saturation magnetization M_{RT} is smaller than a zero temperature.

defined considering an assembly of magnetic moments $\mathcal{M}$ averaged over a small volume ΔV of the sample:

$$\boldsymbol{M} = \frac{\sum_{\Delta V} \mathcal{M}}{\Delta V}. \tag{5.1}$$

In this definition, an assembly of magnetic moments pointing in the same direction is substituted by their spatial average $\boldsymbol{M}$. This makes sense at length scales of the exchange length, *i.e.* the length at which exchange energy is significant (around 5 nm in Py), so that the orientation of magnetic moments is uniform .

At equilibrium, the magnetization is oriented along the effective field H_{eff}, given by the interplay of all the forces acting on the individual atomic moments. At equilibrium, the effective field $\boldsymbol{H}_{\text{eff}}$ is defined as the functional derivative $\delta H_m / \delta \boldsymbol{M}$ of the magnetic energy H_m with respect to the magnetization $\boldsymbol{M}$. When such equilibrium is broken by an external perturbation (like an applied field or a spin polarized current), the magnetization evolves toward a new equilibrium position, that takes into account the contributions of the perturbation and of the different energies inside the ferromagnet. The effective field is a local quantity, defined on same lengthscale as the magnetization. The magnetic energy contains the following contributions:

1. Exchange energy $E_{ex} = \frac{2A}{M^2}(\vec{\nabla} \cdot \boldsymbol{M})^2$ (A being the exchange constant) which favors the alignment of the magnetic moments, and depends on the spatial inhomogeneity of the magnetization.

2. Zeeman energy $E_Z = -\boldsymbol{M} \cdot \boldsymbol{H}_{\text{ext}}$, which represents the interaction of the magnetization with the external field $\boldsymbol{H}_{\text{ext}}$, and depend on the angle between these vectors.

3. Demagnetizing energy $E_d = 2\pi(N_x M_x^2 + N_y M_y^2 + N_z M_z^2)$, which is a long range energy associated to the dipolar interaction between the individual magnetic moments, and tends to align them antiparallel to one another. This energy is written using the demagnetization factors (N_x, N_y, N_z), which depend on the shape of the sample.

4. Magnetocrystalline anisotropy energy (which in case of uniaxial anisotropy reads $E_k = K_1 \sin^2\theta + K_2 \sin^4\theta + ...$), the energy which facilitates the alignment of the magnetization with certain directions of the chrystal network, called *easy magnetization axes.*

5. Magnetoelastic energy, which tends to align the direction of the magnetization along the axis of deformation constraints and the surface energy, which introduces an anisotropy at the interface between magnetizd layers.

The reader can find a detailed description of the different energy contributions in Ref.[5].

When a uniform external magnetic field $\boldsymbol{H}_{\text{ext}}$ is applied to the sample, the magnetic moments of the various domains tend to align with the field, adding together to create a non vanishing average magnetization. The stronger the external magnetic field, the more the domains align, so that $\langle\boldsymbol{M}\rangle$ grows until *saturation* is attained: an increase of $\boldsymbol{H}_{\text{ext}}$ cannot increase $\langle\boldsymbol{M}\rangle$ further. The norm of the space average magnetization $\langle\boldsymbol{M}\rangle$ in a saturated ferromagnet is called *saturation magnetization.* The space averaged magnetization as a function of a (uniform and time independent) magnetic field is shown in the hysteretic curve FIG.(5.2)b. The saturation magnetization depends strongly on the temperature of the sample. At zero temperature, a ferromagnet reaches the state of lowest energy, in which all the magnetic moments point in the same direction. As the temperature increases, more and more spins deviate randomly from the common direction, increasing the internal energy and reducing the net magnetization, so that the saturation magnetization decreases with temperature. The saturation magnetization as a function of temperature in shown in FIG.(5.1). In this work we shall always consider the saturation magnetization at room termperature.

The local equation of motion of the magnetization in a ferromagnet was first proposed by Landau and Lifshitz in 1935 [62]. This equation describes the precession of the magnetization around the effective field at the lengthscale of exchange length, where the saturation magnetization M is a constant of motion. The derivation shown below starts considering the magnetic moments of the ferromagnet as a sum of classical tops. Let us consider an assembly of tops contained in a small volume V (the order of magnitude of exchange length), with angular momenta $\boldsymbol{J}$ and magnetic moments $\boldsymbol{\mathcal{M}}$. In

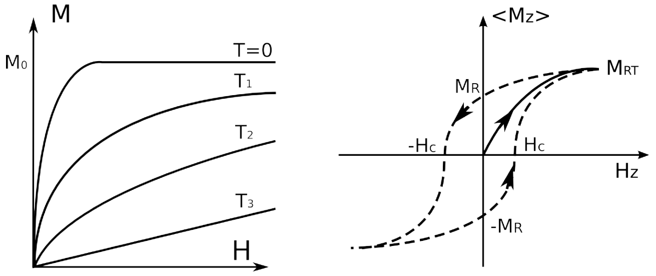

(a) (b)

Figure 5.2: Magnetization as a function of field and temperature. (a) Schematic of the magnetization as a function of applied field for different temperatures $T_1 < T_2 < T_3$. At high fields the magnetization saturates to a value that depends on the temperature. Due to thermal disorder, the higher is the temperature, the lower is the value of the saturation magnetization. (b) First magnetization graph (solid line) and hysteresis loop (dashed line) that show the magnetization as a function of applied field. The arrows show the direction in which the hysteretic loop is ranged. When the field is brought back to zero, the material has a remanent magnetization $\pm M_R$. Two critical values $\boldsymbol{H}_c$ corresponds to the values of the field that annihilate the magnetization.

such a volume the tops precess uniformly. The equation of motion of each top can be written as

$$\hbar \frac{\partial J}{\partial t} = \mathcal{M} \times \boldsymbol{H}_{\text{eff}}, \tag{5.2}$$

To make appear the magnetization, it is sufficient to multiply Eq.(5.2) by the number of tops per unit volume V:

$$\frac{\partial \boldsymbol{M}}{\partial t} = -\gamma \boldsymbol{M} \times \boldsymbol{H}_{\text{eff}}, \tag{5.3}$$

This term, called *adiabatic torque*, can be derived from quantum mechanics, and does not allow for energy dissipation. Solving the above ordinary differential equation leads for confined geometries to a series of discrete solutions. The different eigen-values ω satisfy the equality $\omega = \gamma H_{\text{eff}}$, where $\omega/(2\pi)$ represents the Larmor precession frequency and γ is the gyromagnetic ratio. In order to take into account dissipation, Landau and Lifshitz proposed to include in the equation of motion a phenomenological term:

$$\frac{\partial \boldsymbol{M}}{\partial t} = -\gamma \boldsymbol{M} \times \boldsymbol{H}_{\text{eff}} + \frac{\gamma \alpha_{LLG}}{M} \boldsymbol{M} \times (\boldsymbol{M} \times \boldsymbol{H}_{\text{eff}}) \tag{5.4}$$

where α_{LLG} is a dimensionless dissipation parameter. Gilbert [40] proposed

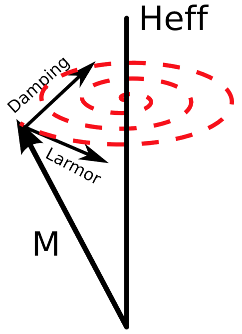

Figure 5.3: Schematic of the dynamics of the magnetization vector $\boldsymbol{M}$. The adiabatic torque (or Larmor term) $\boldsymbol{L} = -\gamma \boldsymbol{M} \times \boldsymbol{H}_{\text{eff}}$ is responsible for steady precession of $\boldsymbol{M}$ around $\boldsymbol{H}_{\text{eff}}$, while the damping $\boldsymbol{D} = \alpha \boldsymbol{M} \times \partial \boldsymbol{M}/\partial t$, is a viscous friction that tends to align $\boldsymbol{M}$ with $\boldsymbol{H}_{\text{eff}}$. The motion of the magnetization is a spiral around the effective field.

an equivalent form of the equation of motion, where the damping term is described as a viscous force:

$$\frac{\partial \boldsymbol{M}}{\partial t} = -\gamma \boldsymbol{M} \times \boldsymbol{H}_{\text{eff}} + \frac{alpha_{LLG}}{M} \boldsymbol{M} \times \frac{\partial \boldsymbol{M}}{\partial t} \tag{5.5}$$

In general we shall refer to Eqs.(5.4,5.5) as Landau-Lifshitz-Gilbert (LLG) equation. This equations predict that the magnetization precesses with a spiral around the effective field, and eventually aligns with it, with a characteristic time of $(\alpha_{LLG}\gamma H_{\text{eff}})^{-1}$ [see FIG.(5.3]. Developing the double cross product of the dissipation term of Eq.(5.4) one obtains

$$\frac{\gamma \alpha_{LLG}}{M} \boldsymbol{M} \times (\boldsymbol{M} \times \boldsymbol{H}_{\text{eff}}) = \frac{\gamma \alpha_{LLG}}{M} [\boldsymbol{M}(\boldsymbol{H}_{\text{eff}} \cdot \boldsymbol{M}) - \boldsymbol{H}_{\text{eff}} M^2], \tag{5.6}$$

which shows that the dissipation is equivalent to the relaxation of $\boldsymbol{M}$ towards $\boldsymbol{H}_{\text{eff}}$ with a caracteristic rate $1/\tau = \gamma \alpha_{LLG} \boldsymbol{H}_{\text{eff}}$.

The dimensionless *damping ratio* α_{LLG} represents the dissipation processes (coupling between magnons, phonons, electrons...) and governs the rate of approach to equilibrium.

The theoretical description of the magnetization dynamics of large samples is done through micromagnetic simulations, where the sample is modeled through a lattice of sites, each site representing a magnetic domain with uniform magnetization. In this picture, the magnetization in each site obeys the LLG equation, and the sites are coupled through exchange interaction. The quantity of interest in these simulations is the space-averaged magnetization, that take into account the contribution of each site. This description is coherent with the experimental technique described in the following chapter, where only the space-averaged magnetization can be detected.

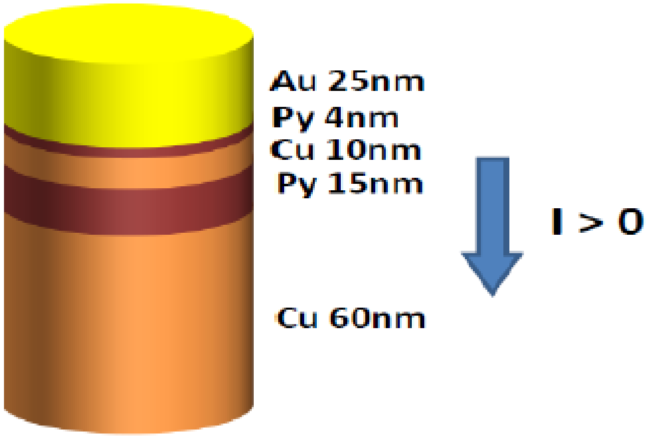

Figure 5.4: Cartoon of the multilayer studied in this work. Two permalloy layers with different thickness (thin=4 nm, thick=15 nm), and with a radius R=125 nm are separated by a Cu spacer of 10 nm, and connected to two contacts. An homogeneus field applied along the axis of the cylinder saturates the magnetization of both layers. The dynamics of the magnetization can be excited by various means (dc or rf current, rf field).

5.3 Excitation of the magnetization dynamics

5.3.1 Dynamics inside a normally magnetized system

Excitations that compensate the damping and lead to stable precession of the magnetization can be described adding supplementary terms to the LLG equation. In particular, we shall describe the role of spin torque in the excitation of the dynamics. We focus on the dynamics inside a multilayer like the one shown in FIG.(5.4), which corresponds to the system that we shall study through experiments and simulations in the next chapter.

In such a system, the dynamics of the magnetization occurs inside thin and thick layer (labeled layer 1 and 2), with magnetization $\boldsymbol{M}_1$ and $\boldsymbol{M}_2$ correspondingly, and both layers are saturated by an external field parallel to the the axis of the cylinder $\hat{\boldsymbol{e}}_z$. In this system, steady precession is circular at fixed angle θ, and the equilibrium axis corresponds to the direction of the applied field $\boldsymbol{H}_{\text{ext}}$ (in general this is not the case). The magnetization can be divided into a static (longitudinal) component and an oscillating (transverse) component. This subdivision allows to describe the energy absorbed and released by the system in terms of changes of the longitudinal component.

The LLG equation of a ferromagnetic layer, in presence of an external periodic excitation field $\boldsymbol{f}$, can be written as

$$\frac{-1}{\gamma}\partial_t \boldsymbol{M} \approx \boldsymbol{M} \times \boldsymbol{H}_{\text{eff}} + \boldsymbol{M} \times \boldsymbol{d} + \boldsymbol{M} \times \boldsymbol{f} \exp^{-i\omega t}. \tag{5.7}$$

The second term and third torque terms of Eq.(5.7) describe two energy non-conservative process which are respectively the dissipative field $\boldsymbol{d}$ and the external periodic driving field $\boldsymbol{f}$. An oscillating forced motion at one of the eigen-frequency of the system, leads to a steady state precession of $\boldsymbol{M}$, whose oscillating component expresses the equilibrium between $\boldsymbol{f} = \boldsymbol{d}$, where

$$\boldsymbol{d} = -\alpha_{\text{LLG}} \left[\hat{\boldsymbol{e}}_M \times \boldsymbol{H}_{\text{eff}}\right], \tag{5.8}$$

We have introduced here the notation $\boldsymbol{M} \equiv M\hat{\boldsymbol{e}}_M$, with M the norm of the magnetization (a constant of the motion) and $\hat{\boldsymbol{e}}_M$ a unit vector in the direction of the magnetization.

5.3.2 rf field, rf current and spin torque excitations

The external excitation $\boldsymbol{f}$ is decomposed in three different contributions

$$\boldsymbol{f} = \boldsymbol{f}_u + \boldsymbol{f}_o + \boldsymbol{f}_s, \tag{5.9}$$

which correspond to different excitations.The first type of excitation field corresponds to a uniform RF magnetic field applied perpendicularly to the effective field $\boldsymbol{H}_{\text{eff}}$. This configuration corresponds to the conventional mean of performing FMR spectroscopy. The force field then reduces to the expression:

$$\boldsymbol{f}_u = h_{\text{rf}}\hat{\boldsymbol{e}}_x. \tag{5.10}$$

where $\hat{\boldsymbol{e}}_x$ is a unit vector in the in-plane direction, assuming from now on that the sample is uniformly magnetized along the pillar axis $\hat{\boldsymbol{e}}_z$.

In this work, SW spectroscopy is also performed by injecting a uniform RF charge current i_{rf} across the nano-pillar (*i.e.* along the pillar axis $\hat{\boldsymbol{e}}_z$). First this produces an ortho-radial RF Oersted field

$$\boldsymbol{f}_o = \left[\frac{4\pi}{10}\right] \frac{i_{\text{rf}}}{2\pi R} \left[r\hat{\boldsymbol{e}}_r \times \hat{\boldsymbol{e}}_z\right], \tag{5.11}$$

where R is the radius of the pillar and $\hat{\boldsymbol{e}}_r$ is a unit vector along the radial direction. The prefactor between the square brackets is here for consistency purpose with the cgs unit system. In this formula the current should be expressed in A (instead of esu/sec) and the quantity between the square bracket in the prefactor converts A/cm into Oe.

In this case a second contribution comes from RF Slonczewski-Berger [88, 9] term:

$$\boldsymbol{f}_s = \frac{i_{\text{rf}}}{2\pi\lambda} \left[\hat{\boldsymbol{e}}_M \times \hat{\boldsymbol{e}}_P\right], \tag{5.12}$$

where $\hat{\boldsymbol{e}}_P$ is a unit vector in the direction of the spin polarization of the current, which coincides with the direction of magnetization of the so-called fixed layer $\boldsymbol{P}$ (in our case the thick layer M_2), the proportionality coefficient being

$$\frac{1}{\lambda} = \frac{\eta h}{2eMV}, \tag{5.13}$$

where λ has the dimension of a distance (*i.e.* the product i_{rf}/λ is equivalent to a magnetizing field). The value of λ depends on η the degree of spin polarization of the current, h the Planck constant, e the modulus of the electron charge, and V the volume of the layer.

If one assumes that there is no direct spin current flowing through the layers ($I_{\mathrm{dc}} = 0$), $\boldsymbol{d}$ in Eq.(5.8) reduces to the natural dissipation term written in the Landau-Lifshitz form, which is proportional to the Gilbert damping constant α_{LLG}. The quantity measured experimentally is usually the full linewidth $\Delta H = 2d$. The damping ratio $\gamma \Delta H/\omega$ reduces to α_{LLG} only in the case of samples homogeneously magnetized and when the precession is circular (as opposed to elliptic). If direct spin polarized current I_{dc} flows through the layers, spin transfer effects opposes to $\boldsymbol{d}$ and compensates it at threshold current

$$I_{th} = 2\pi\lambda\alpha_{LLG}H_{\mathrm{eff}}, \tag{5.14}$$

the result is a steady state precession of the magnetization above critical current. We remark that spin torque has an influence on both layers, which depends on the direction of the current, as described in Sec.(2.2.3). In this work we focus on the case where the current decreases the damping of thin layer and increases the damping of fixed layer, so that it induces a precession in the thin layer.

For circular precession, one can define a longitudinal and transverse component of the magnetization in the steady-state regime, respectively the component parallel and perpendicular to the precession axis [FIG.(5.5)]:

$$\boldsymbol{M}_{\parallel} = \overline{\boldsymbol{M}} \equiv \overline{M}\hat{\boldsymbol{e}}_{\overline{M}} \tag{5.15}$$

$$\boldsymbol{M}_{\perp} \approx \frac{1}{\omega}\partial_t \boldsymbol{M} \times \hat{\boldsymbol{e}}_{\overline{M}} \tag{5.16}$$

where the overline typography expresses the time averaged quantity (here the magnetization) over a precession period. In this sense, $\hat{\boldsymbol{e}}_{\overline{M}}$ is a unit vector parallel to $\boldsymbol{H}_{\mathrm{eff}}$, the precession axis. M being a constant of the motion, the two components are related through the equality $M_{\parallel}^2 = M^2 - M_{\perp}^2$, which reduces to $M_{\parallel} \approx M - M_{\perp}^2/(2M)$ for small oscillation $M_{\perp} \ll M_{\parallel}$. At steady state, the precession angle θ between the $\boldsymbol{H}_{\mathrm{ext}}$ and $\boldsymbol{M}$ is constant.

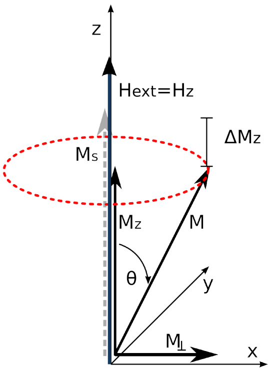

Figure 5.5: An excitation (typically an RF field or a spin polarized current) opens a precession angle θ between the magnetization $\boldsymbol{M}$ and the effective field $\boldsymbol{H}_{\text{eff}}$, which reduces the longitudinal component M_z of ΔM_z. At fixed angle θ, M_z is static while the transverse part $M_\perp$ precesses at the Larmor frequency. the angle θ increases when some energy is absorbed and decreases when is dissipated.

When some energy is absorbed (released), the precession angle increases (decreases), so that the value of $M_\parallel$ decreases (increases). The energy absorbed (or released) by the system in such process depends only on the variation $\Delta M_\parallel$ of the longitudinal magnetization:

$$E = \int_V \delta \boldsymbol{M}(\boldsymbol{r}) \cdot \boldsymbol{H}_{\text{eff}}(\boldsymbol{r}) = \hbar\omega_0 \frac{\Delta M_z}{\gamma\hbar}. \tag{5.17}$$

Within a particle-like intepretation, this means that a photon absorbed by the system lowers the magnetization of a quantity $\gamma\hbar$ (a magnon is created), and the energy stocked by the system corresponds to the number of photons necessary to lower the magnetization of $\Delta M_\perp$, multiplied by the energy of a photon $\hbar\omega_0$.

To gain further insight about the dynamics, it is useful to decompose the instantaneous magnetization vector in respectively a static and dynamic component.

$$\hat{\boldsymbol{e}}_M \approx \hat{\boldsymbol{e}}_{\overline{M}} + \boldsymbol{\varepsilon}_M \exp^{-i\omega t} \tag{5.18a}$$

$$\hat{\boldsymbol{e}}_P \approx \hat{\boldsymbol{e}}_{\overline{P}} + \boldsymbol{\varepsilon}_P \exp^{-i\omega t} \tag{5.18b}$$

where $\boldsymbol{\varepsilon}_M \exp^{-i\omega t} \equiv \boldsymbol{M}_\perp / M \ll 1$ represents the dynamic part of the magnetization renormalized by M and it is perpendicular to $\hat{\boldsymbol{e}}_{\overline{M}}$. We have also included in the equation of motion the existence of coupled dynamics, with the excitation of both the "free" layer and the "fixed" (polarizer) layers $\boldsymbol{\varepsilon}_P$. The case of couple dynamics, relevant for our system, will be described in

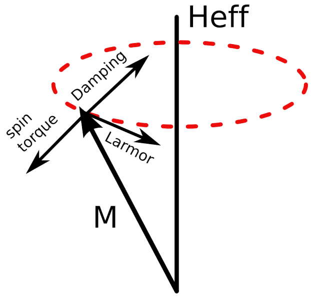

Figure 5.6: Effect of spin torque $\boldsymbol{\tau}$ on the dynamics of the magnetization. When $\boldsymbol{\tau}$ compensates damping it induces a stable precession of the magnetization at fixed angle θ.

details in the following of this chapter. Using this notation, we can now rewrite the equation of motion shown in the introduction by collecting the time dependent fields in two terms:

$$\boldsymbol{d} = -\alpha_{\mathrm{LLG}}\left[\boldsymbol{\varepsilon}_M \times \boldsymbol{H}_{\mathrm{eff}}\right] + \frac{I_{\mathrm{dc}}}{2\pi\lambda}\left[\boldsymbol{\varepsilon}_M \times \hat{\boldsymbol{e}}_{\overline{P}} + \hat{\boldsymbol{e}}_{\overline{M}} \times \boldsymbol{\varepsilon}_P\right]. \tag{5.19a}$$

$$\boldsymbol{f} = \boldsymbol{h}_{\mathrm{rf}} + \frac{i_{\mathrm{rf}}}{2\pi\lambda}\left[\hat{\boldsymbol{e}}_{\overline{M}} \times \hat{\boldsymbol{e}}_{\overline{P}} + \boldsymbol{\varepsilon}_M \times \boldsymbol{\varepsilon}_P\right]. \tag{5.19b}$$

where we have added the possibility of adding a I_{dc} excitation. The different cross terms have been divided in two separate contributions: one proportional to the periodic external drive signal and another proportional to the dynamic magnetization. The static mixed terms corresponds to a change of the precession axis are collected inside the static field $\boldsymbol{H}^\star$

$$\begin{aligned}\boldsymbol{H}^\star = {} & \boldsymbol{H}_{\mathrm{eff}} + \frac{I_{\mathrm{dc}}}{2\pi\lambda}\left[\hat{\boldsymbol{e}}_{\overline{M}} \times \hat{\boldsymbol{e}}_{\overline{P}}\right] + \\ & \frac{i_{\mathrm{rf}}}{2\pi\lambda}\left[\boldsymbol{\varepsilon}_M \times \hat{\boldsymbol{e}}_{\overline{P}} + \hat{\boldsymbol{e}}_{\overline{M}} \times \boldsymbol{\varepsilon}_P\right]\end{aligned} \tag{5.20a}$$

The additional contributions to $\boldsymbol{H}_{\mathrm{eff}}$ can potentially change the nature of the normal modes inside the system. In our case, they are small compared to H_{eff} and we can make the approximation $\boldsymbol{H}^\star \approx \boldsymbol{H}_{\mathrm{eff}}$ and thus the nature of $\boldsymbol{\varepsilon}_M$ and $\boldsymbol{\varepsilon}_P$ do not change with the dc current.

5.4 Spin waves

So far our description of the dynamics of the magnetization has been local, in the sense that we haven't taken into account how the precession profile of the magnetization varies inside the sample. In the most general case

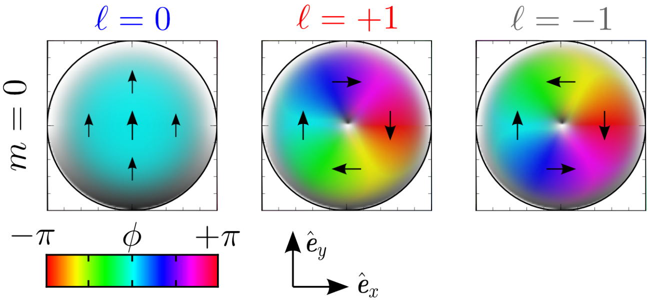

Figure 5.7: (Color online) Color representation of the spin-wave normal mode inside a disk as a function of the azimuthal mode index ℓ with fixed radial index $m = 0$. In our color code, the hue indicates the phase (or direction) of the transverse component of the magnetization $M_\perp$, while the brightness indicates the amplitude diminution of the longitudinal (static, normal to the plane) component, $M_\parallel$. Thus the nodal positions are marked on the figure in white. Nodes are regions where $M_\perp$ vanishes (no precession). A shadow effect has been added to visually enhance the precession regions. The arrows are a snapshot of $M_\perp$ inside the disk. All vectors are rotating synchronously in-plane at the Larmor frequency.

the dynamics of the magnetization is described by the vector field $\boldsymbol{M}(\boldsymbol{r}, t)$, and an excitation of the magnetization propagates as a *spin wave* inside the sample. In particular, one has to take into account the geometry of the sample, and the fact that thin and thick layers are coupled via dipolar interaction and possibly by spin torque. Strictly speaking, the picture of fixed and free layer does not hold, since the dynamics inside the two layers is coupled.

In this section, we discuss the boundary-value problem for spin-wave propagation inside normally magnetized structures. We describe the normal mode representations for axially symmetric geometries both for the single and the bi-layer case. In particular, we classify their symmetries, which point the way to the possible selection rules for spin-wave coupling in spin-valve nano-pillars.

The essential point that we shall discuss below is that in our case, the dynamics inside the two ferromagnetic layers is coupled via dipolar interaction.

5.4.1 Spin waves inside a single disk

FIG.(5.7) shows a generic representation of the magnetization dynamics inside a normally magnetized sample. The precession movement of the local magnetization vector $\boldsymbol{M}_s$ is decomposed in $\boldsymbol{M}_\parallel$, a large static component, and in $\boldsymbol{M}_\perp$, a small oscillating component rotating at the Larmor frequency.

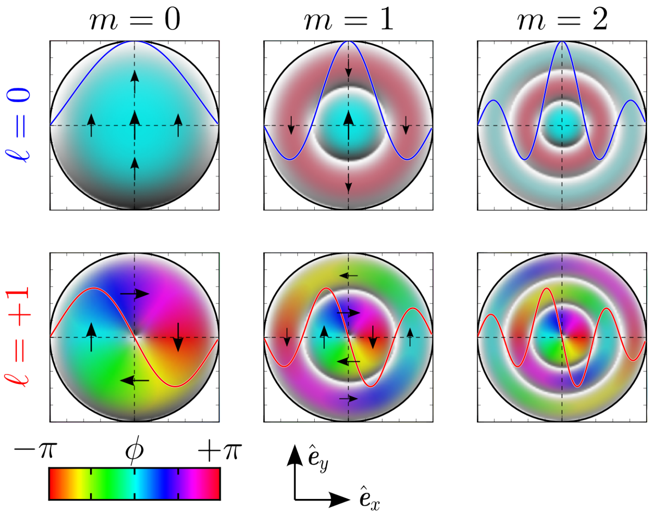

Figure 5.8: (Color online) Same color representation of the normal mode spin-wave basis as a function of the radial mode index m with fixed azimuthal index $\ell = 0$ or $\ell = +1$. The blue and red traces superposed show the precession profile along a median axis.

These two components are respectively longitudinal and transverse to the local precession axis. The longitudinal component is static only because $\boldsymbol{M}_s$ precesses regularly along a circular orbit, a unique feature of the normal configuration. For perpendicularly magnetized samples, the uniform magnetic state is only approached asymptotically and the magnetization at the periphery is always slightly canted along the edge as it forms a so-called cone state. At first, we shall assume that the local precession axis is uniformly defined by the unit vector $\hat{\boldsymbol{e}}_z$ in the direction normal to the plane layers and thus $\boldsymbol{M}_\parallel$ reduces to M_z. In the following, we shall restrict further our study to the case of thin layers (less than 15nm in thickness) so that one can assume hereafter that the magnetization dynamics is uniform along the thickness. In this approximation, the linearized Landau-Lifshitz equation about the equilibrium orientation, simplifies to two equations describing the circular precession of the transverse magnetization projections M_x and M_y, which itself depends only on only two spatial variables x and y (two-dimensional model). In general the diagonalization of the Landau-Lifshitz equation restricted to the adiabatic term (see appendix) inside a confined geometry lead to a discrete series of normal modes each having a different eigen-value, $\omega/(2\pi)$, the so-called Larmor precession frequency. The two real equations can be rewritten as one complex equation for the dimensionless complex variable

$$c = \frac{M_x + iM_y}{2M_s} \tag{5.21}$$

that depends on the spatial position

$$p = r \exp^{+i\phi}, \tag{5.22}$$

where we introduced here the two polar coordinates (r, ϕ). For disk geometries, the solutions are known and have the following analytical expression [51, 45].

$$c(p,t) = J_\ell(k_{\ell,m} r) \exp^{+i\ell\phi} \exp^{-i\omega t}, \tag{5.23}$$

where J_ℓs are the Bessel functions of the first kind and $k_{\ell,m}$ is the modulus of the in-plane SW wave vector, which depends on the boundary conditions. In this notation, ℓ and m represent respectively the azimuthal and radial mode index *i.e.* the number of zeroes in the circumferential and radial directions.

Such solutions to the boundary-value problem leave one adjusting parameter, which is the ratio of precession between the center and the edge of the disk, a quantity associated to pinning phenomena. The amount of pinning should be in principle identical for all eigen-modes. Hereafter we shall assume that all the modes satisfy the dipolar pinning condition [45], which corresponds to $k_{\ell,m} \approx \kappa_{\ell,m}/(R+t)$, where $\kappa_{\ell,m}$ is the $(m+1)^{\text{th}}$ root of $J_\ell(x)$, R is the radius of the disk and t its thickness. The dipolar pinning condition can be viewed as equivalent to the total pinning condition at the periphery of a virtual disk, whose radius as been augmented by the disk thickness $M_\perp(R+t) \approx 0$.

FIG.5.7 shows a color representation of the normal modes spatial pattern for three values of the azimuthal mode index $\ell = 0, +1, -1$ with the radial index being fixed at $m = 0$. In our color code, the hue indicates the phase (or direction) of the transverse component of the magnetization $M_\perp$, while the brightness indicates the amplitude of the longitudinal component, $M_\parallel$. Thus the nodal positions are marked on the figure in white. A node is a location where the transverse component vanishes and the magnetization vector is aligned along the equilibrium axis. This coding scheme allows us to visualize distinctly the phase and amplitude of the signal. The black arrows are a snapshot of the orientation of $M_\perp$ inside the disk. All arrows are rotating synchronously in-plane at the Larmor frequency.

The first panel on the left shows the $\ell = 0$ mode, also called the uniform mode. It usually corresponds to the lowest energy mode since all the vectors are pointing in the same azimuthal direction at all time. The middle panel is the $\ell = +1$ mode. It corresponds to spin-waves that are rotating around the disk in the same direction as the Larmor precession. The corresponding phase of the signal is in quadrature between two consecutive quadrant positions. The obtained spatial pattern of $M_\perp$ preserves the rotation invariance symmetry. Another property of this mode, is that it has a node at the center of the disk. We have also put on the figure the $\ell = -1$ mode in the right panel. This mode describes spin-waves that are rotating around the disk in the opposite direction as the Larmor precession. The resulting pattern has a contra-rotational invariance. Another way to differentiate it from the $\ell = +1$ is to use a concept developed in fluid dynamics, where the two cases are separated by an opposite vorticity. We mention that in the magneto-exchange approximation, the two $\ell = \pm 1$ modes are degenerate in energy.

The upper row of FIG.(5.8) shows a color representation of the same orthogonal functions for three values of the radial mode index $m = 0, 1, 2$, with the azimuthal index being fixed at $\ell = 0$. They represent clearly higher harmonics with increasing number of nodal rings in the radial direction. Each ring separates region of opposite phase along the radial direction. For completeness purpose, the representation in FIG.(5.8) is repeated below for another values of the azimuthal index $\ell = +1$. It is worth to mention at this point that the ℓ-index usually carries the discriminant symmetry for the coupling to an external coherent source. The obtained spin-wave spectrum represents then a probing of the magnetization dynamics along one particular value of the ℓ-index. One example is the case of conventional FMR, which uses a uniform RF magnetic field to excite the disk. Only modes which have non-zero spatial average couple to the excitation field. Therefore all the normal modes having $\ell \neq 0$ are invisible because they have no overlap with the RF magnetic field excitation. Conventional FMR spectrum is a partial representation of the eigen-modes as a function of the m-index projected upon $\ell = 0$-index value.

5.4.2 Spin waves inside two mutually coupled disks

In this section, we review the diagonalization process to describe the dynamics of two mutually coupled magnetic layers. The dynamical coupling considered here is the dipolar interaction mediated by the bi-layer tensor element $N_{xx}^{(j,j')}$, which represents the in-plane contribution of the dipolar field inside layer $j = 1, 2$ produced by the in-plane component of the magnetization of layer $j' = 2, 1$. The mathematics of the exact diagonalization procedure is tedious and it leads to very complex analytical expressions. To simplify the problem, we shall retain only the first order term in the decomposition of the solutions using the SW normal basis expressed by the Bessel functions. In other words, we shall assume that the shape of the precession profiles of the modes in each layer are unperturbed by the dynamical coupling. The equations of motion of $\langle c_j \rangle$ and $\langle c_{j'} \rangle$, the spatial average dimensionless complex variables attached respectively to the reduced transverse magnetization

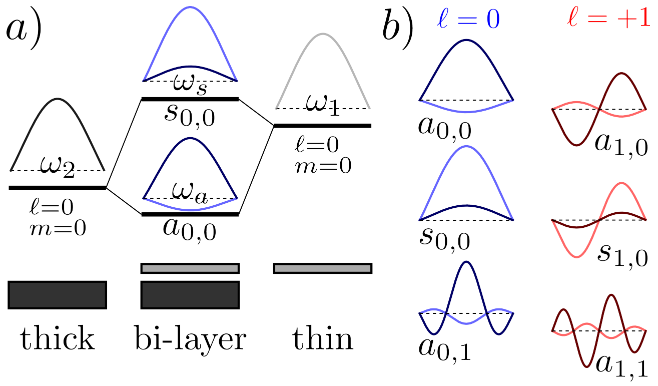

Figure 5.9: (Color online) a) Schematic representation of the mutually coupled dynamics of two dislike magnetic disks. When the two disks are apart, the uniform mode of the thick layer resonates at a lower frequency than the uniform mode in the thin layer. When the two disks are coupled by the dipolar interaction, the binding state corresponds to having the two layers oscillating in opposition of phase a, while the anti-binding state corresponds to having the two layers oscillating in phase s. This is shown schematically by displaying the precession profile of each layer, where light-colors represent the contribution of the thin layer, while dark-colors represent the contribution of the thick layer. b) We propose to describe the dynamics of the bi-layer system by adding a new index a or s indicating if the precession occurs mostly in the thick or in the thin layer respectively.

in each layer, are coupled

$$\partial_t \langle c_j \rangle = -i\omega_j \langle c_j \rangle - \eta^{(j,j')} \langle c_{j'} \rangle \tag{5.24}$$

The coupling term

$$\eta^{(j,j')} = 4\pi\gamma \left\{\!\!\left\{ N_{xx}^{(j,j')} \right\}\!\!\right\} M_{j'} \tag{5.25}$$

represents the overlap integral through $N_{xx}^{(j,j')}$ between the oscillatory modes in each layer. The overlap is expected to be maximum between two modes bearing similar wave numbers. We thus simplify further the problem by reducing the number of coupled modes to a pair of same index. Concentrating on the coupled dynamics between uniform modes ($\ell = 0$ and $m = 0$), the coupling takes the form:

$$\begin{aligned} \left\{\!\!\left\{ N_{xx}^{(j,j')} \right\}\!\!\right\} = & \frac{1}{\langle J_0 \rangle^2} \int_{V_j} d^2\boldsymbol{r} dz J_0(k_0 \boldsymbol{r}) \\ & \int_0^R dr' J_0(k_0 r') \frac{\partial N_{xx}\left[r'\right](\boldsymbol{r}, z)}{\partial r'} \end{aligned} \tag{5.26}$$

where the quantity under the integral operand, $dr' \partial N_{xx}\left[r'\right](\boldsymbol{r}, z)/\partial r'$, represents the stray field produced by a ring of width dr', radius r', and thickness $t_{j'}$ at the position $(\boldsymbol{r}, z)$. This term uses the known analytical expression for $N_{xx}\left[r'\right]$ [91], which is defined as the depolarization tensor of a full disk of radius r'. One can generalize the coupling integral introduced in Eq.5.26 to any arbitrary modes and show that the coupling strength is maximum if c_1 and c_2 have the same ℓ and m indices.

We resolve the two differential equations above by making an analogy to two coupled harmonic oscillators in the weak coupling approximation $\eta \ll \omega$. Making the scale transformation:

$$C_1 = \sqrt{\frac{\eta^{(12)}}{\eta^{(21)}}} \langle c_1 \rangle \tag{5.27}$$

$$C_2 = \sqrt{\frac{\eta^{(21)}}{\eta^{(12)}}} \langle c_2 \rangle \tag{5.28}$$

$$\tag{5.29}$$

the sum of the two equations simplifies to

$$(\partial_t C_1)^2 + (\partial_t C_2)^2 \approx -\omega_1^2 C_1^2 - \omega_2^2 C_2^2 - \Gamma^2 C_1 C_2 \tag{5.30}$$

where

$$\Gamma^2 = 2\left(\eta^{(12)}\omega_2 + \eta^{(21)}\omega_1\right) \tag{5.31}$$

The solutions of the above equation are well known and can be formulated into a problem of a quadratic equation with two variables. The diagonalization of the quadratic form includes a rotation of the coordinate system,

$$\begin{pmatrix} C_s \\ C_a \end{pmatrix} = \begin{pmatrix} +\cos\varphi & +\sin\varphi \\ -\sin\varphi & +\cos\varphi \end{pmatrix} \begin{pmatrix} C_1 \\ C_2 \end{pmatrix} \tag{5.32}$$

where the angle φ satisfies the equality $\tan 2\varphi = \Gamma^2/(\omega_1^2 - \omega_2^2)$. The new variable C_a and C_s corresponds to a collective dynamics (anti-symmetric and symmetric) involving a contribution of both oscillators. The decoupled Hamiltonian obtained by the rotation of coordinates has two normal frequencies:

$$\omega_s^2 = \frac{1}{2}\left(\omega_1^2 + \omega_2^2 + \sqrt{(\omega_1^2 - \omega_2^2)^2 + \Gamma^4}\right) \tag{5.33a}$$

$$\omega_a^2 = \frac{1}{2}\frac{4\omega_1^2\omega_2^2 - \Gamma^4}{\omega_1^2 + \omega_2^2 + \sqrt{(\omega_1^2 - \omega_2^2)^2 + \Gamma^4}} \tag{5.33b}$$

It is useful to introduce the frequency quantity $\Omega = \frac{1}{8}\Gamma^2 \tan 2\varphi/\overline{\omega}$, where $\overline{\omega} = (\omega_1 + \omega_2)/2$ is the average of the two eigen-values in the absence of coupling. As shown below, $\Omega \approx \eta^{(12)}\eta^{(21)}/(\omega_1 - \omega_2)$ represents the amount of frequency shift induced by the dynamical coupling (about 0.17 GHz). For our nano-pillar Ω is small compared to $\overline{\omega}$ (about 10 GHz). It implies that the angle φ is small and the nature of the collective mode defined in Eq.5.32 will bear mostly the dynamical characteristics of the separated structure. A numerical application with the characteristics of our sample, leads to an amount of mixing between the two modes, which is about $\varphi = +13°$. We mention that the sign of φ is positive meaning that the dynamical dipolar coupling between the two disks is binding when both layers vibrate in antiphase. Thus, the fundamental mode is the collective mode C_a with eigen-frequency $\omega_a \approx \omega_2 - \Omega\overline{\omega}/\omega_2$,. It corresponds to having a collective motion, where the precession is mostly located in the thick layer $c_2 > c_1$ but with the thin layer also precessing in antiphase. It is easy to show that in this case $c_2/c_1 = (\omega_1 - \omega_a)/\eta^{(12)}$. Reciprocally, the excited state is the collective mode C_s, whose eigen-frequency is $\omega_s \approx \omega_1 + \Omega\overline{\omega}/\omega_1$. It corresponds to a collective motion, where the precession is mostly located in the thin layer $c_1 > c_2$, but with the thick layer also precessing in phase. in this case $c_1/c_2 = \eta^{(12)}/(\omega_s - \omega_1)$.

The important parameter that determines the coupling regime pertinent to our system, is the ratio of the dynamical coupling strength to the difference of eigen-frequencies of each separate oscillator. A common characteristic of spin-valve structures is that they usually consist of different magnetic layers. In our case the spin-valve comprise two different Permalloy thickness: a thin layer, labeled 1, and a thick layer, labeled 2. Thus the normal modes with the same indices will resonate at different frequencies depending whether they occur in the thin or thick layer. The difference of eigen-frequency will have two origins: i) the difference in internal demagnetizing field (intra-layer static dipolar coupling) and ii) the difference of stray field of one layer on the other (inter-layer static dipolar coupling). We concentrate first on the coupled dynamics between the uniform modes, which bears the index $\ell = 0$ and $m = 0$. Cavity-FMR spectroscopy performed at fixed frequency on the reference film in the perpendicular configuration find the magnetic field position of the resonance of the thin layer, H_1, is 1.4 kG lower in field (higher in energy) than the position of the resonance of the thick layer, H_2. The difference $H_2 - H_1 > 0$ is ascribed to a difference of magnetization inside the layers: $M_1 < M_2$. After the patterning into a nano-pillar, one expects that the resonance value of the uniform mode, that we continue to label H_1 and H_2, further decreases due to a decrease of the depolarization tensor N_{zz} inside both disks. This decrease should affect, however, more strongly the thick layer, so that the difference $H_2 - H_1$ decreases. The amount of decrease is however small compared to the difference of magnetization $4\pi(M_2 - M_1)$, which remains the dominant contribution. Furthermore, this decreases is partially compensated by the difference of stray field produced by the nearby layer. The effect of the stray field is to further lower the resonance field of both layers. But the thick layer produces a stronger stray field on the thin than reciprocally. In consequence, in order to reach the same value of the total effective magnetic field, a smaller additional external applied magnetic field should be required to excite the resonance of the thin layer compared to the thick. To summarize this, we have displayed schematically on FIG.5.9a the relative position between the two eigen-values in the absence of dynamical coupling. On both side of the bi-layer diagram we have reported on an energy scale their relative position, where the eigen-frequency of the thick layer (dark grey) ω_2 is put below the eigen-frequency of the thin layer (light grey) ω_1.

The above energy difference needs now to be compared with the strength of the dynamical dipolar coupling between the layer. The later quantity depends on the inter-layer tensor $N_{rr}^{(jj')}$ representing the in-plane contribution of the dipolar magnetic field inside layer $j = 1, 2$ produced by the in-plane component of the magnetization of layer $j' = 2, 1$ (see more details below). In our case the strength of this effect is weak compared to the difference in static dipolar coupling: $N_{rr} M_2 \ll M_2 - M_1$. This implies that the nature of the collective mode will bear mostly the dynamical characteristics of the separated structure. Because, we are in a perpendicular geometry, the dynamical dipolar coupling between the two disks is attractive (lower in energy) when both layers vibrate antisymmetrically. Thus the binding state corresponds to a collective motion where the two layers vibrate antisymmetrically. Since we have identified above the uniform mode of the thick layer as the lowest energy mode of the system, this binding mode will bear approximately the characteristic of the thick layer with the eigen-frequency $\omega_a \approx \omega_2$. This collective mode will be labeled $a_{0,0}$. Reciprocally the antibiding state corresponds to a collective motion where the two layers vibrate symmetrically. The associated collective mode will have thus the characteristic of the thin layer with the eigen-frequency $\omega_s \approx \omega_1$. This collective mode will be labeled $s_{0,0}$. FIG.5.9a gives a schematic representation of this coupled dynamics. We have superposed on the figure the precession profile of each layer as defined in FIG.5.8 adopting a color code, where light-colors represent the contribution of the thin layer, while dark-colors represent the contribution of the thick layer. The anti-symmetric state is represented in the form of two profiles having opposite polarity and dominated by the profile of the thick layer, while the symmetric state is represented by two profiles having the same polarity and dominated by the profile of the thin layer.

FIG.5.9b shows the extension of this concept of collective motion on modes of other indices. We propose to describe the dynamics of the bi-layer system to add a new index a or s indicating if the precession occurs mostly in the thick or in the thin layer respectively. We thus have three indices to label the observed eigen-modes: the usual azimuthal and radial indices for a single disk (ℓ, m), plus an additional index referring to the antisymmetrical or symmetrical (a or s) coupling between both layers.

To conclude this discussion about dynamical coupling, we would like to emphasize that, although the spectral distortions are small in our geometry, the symmetry of the collective motion and the synchronous excitation of the adjacent magnetic layer bears some important consequence in regards to spin transfer effects. There it is the relative difference of the dynamics at the interface that matters and small change of the relative angles between the two layers can play an important role.

Chapter 6

Current driven dynamics inside a nanopillar: experiments and simulations

6.1 Introduction

In this chapter we shall discuss in details the dynamics of the magnetization in a spin torque nano oscillator, both on an experimental and theoretical viewpoint.

In this study, we have compared the SW spectra excited by a uniform in-plane RF magnetic field and by an RF current flowing perpendicularly through the layers. By studying the influence of a spin polarized dc current on the magnetization dynamics and by comparing mechanical-FMR to voltage-FMR spectra, some insight on which magnetic layer contributes mostly to the different SW modes has been obtained. From the theoretical side, a comprehensive labeling of the SW eigen-modes in the studied geometry, which preserves the axial symmetry, has been introduced. Three indices are required to identify the SW modes in the nano-pillar, the usual azimuthal and radial indices for a single disk (ℓ, m), plus an index referring to the anti-symmetrical or symmetrical (a or s) coupling between the two magnetic layers. By confronting the experimental SW spectra to 3D micromagnetic simulations, the observed SW modes have been identified according to this labeling.

Two main results have been deduced from this extensive study. Firstly, we have derived the selection rules that apply to the RF field and to the RF current excitations. Indeed, in the normal configuration, these two excitations lead to SW spectra having mutually exclusive symmetries. Only $\ell = 0$ modes are excited by a uniform RF magnetic field, while only $\ell = +1$ modes are excited by an RF current flowing through the nano-pillar, due to the orthoradial symmetry of the induced Oersted field. Thus, the ℓ-index, related to the azimuthal symmetry of the SW modes, is the discriminating parameter for the selection rules. Moreover, we have shown how these selection rules are affected by breaking the axial symmetry of the exact normal configuration. Namely, $\ell = 0$ modes can also be excited by an RF current owing to the non zero ST-FMR excitation if the magnetizations in the two layers are not collinear. Secondly, the importance of the dynamical dipolar interaction, which couples the magnetization dynamics in both layers, has been pointed out. By analyzing the experimental SW spectra in the frameworks of a 2D analytical model and of full 3D micromagnetic simulations, it was demonstrated that the collective character of the SW eigen-modes in the nano-pillar cannot be disregarded, although the corresponding spectroscopic shifts might be small in the FMR spectra. In fact, we have shown that the SW modes dominated by the thick layer always involve a precession of the thin layer in anti-phase, and reciprocally, the SW modes dominated by the thin layer also involve an in phase precession of the thick layer.

This chapter is organized as follows: In Sec. 6.2 We describe composition and geometry of the sample used in this spectrosopic study. Then we describe the Magnetic Resonance Force Microscope (MRFM) setup used for the spectroscopic characterization of the normally magnetized nano-pillar. MRFM has been used to measure the excitation spectra obtained using an RF current flowing through the nano-pillar perpendicularly to plane (the configuration used in transport characterization) and a uniform RF magnetic field applied parallel to the layers (the configuration used in conventional ferromagnetic resonance). At last, MRFM has been used to study spin transfer effect on the observed spectra, injecting a CPP continuous current through the nanopillar. The studies presented in this section are limited to a dc current up to the threshold current for auto-oscillations in the thin layer.

In Sec. 6.3 we provide a theoretical characterization of the spectra (at zero dc current) using Nmag [37], a micromagnetic simulation package based on finite element discretization of the pillar. In this way we have interpreted the spectrum and identified the spin-wave modes of the nanopillar, according to the classification given in chapter 5.

Sec. 6.4 contains the main results of this work. We have coupled Nmag to CRMT, in order to perform micromagnetic simulations that include spin transfer effect. The approach described in this chapter allows to take into account the spatial variation of magnetization and spin tranfer in a realistic way. In this way we have performed a comprehensive theoretical study of current drivend dynamics near (and above) the critical threshold. In particular, we have described selection rules for spin torque excitation in agreement with experimental results.

6.2 Ferromagnetic resonance force spectroscopy

6.2.1 The litographically patterned nano structure

The spin-valve structure used in this study is a standard Permalloy (Py) bilayer structure sandwiching a 10 nm Copper (Cu) spacer: the thicknesses of the thin and thick layers are respectively t_1 = 4 nm and t_2 = 15 nm. Special care has been put in the design of the microwave circuit around the pillar. FIG.(6.1a) shows a scanning electron microscopy top view of this circuit. The nano-pillar is located at the center of the cross-hair, in the middle of a highly symmetric pattern designed to minimize cross-talk effects between both RF circuits shown in blue and red, which provide two independent excitation means.

The nanopillar is patterned by standard e-beam lithography and ion-milling techniques from the extended film, (Cu60 | $\text{Py}_2$15 | Cu10 | $\text{Py}_1$4 | Au25) with thicknesses expressed in nm, to a nano-pillar of nominal radius 100 nm. Precise control allows for stopping the etching process exactly at the bottom Cu layer, which is subsequently used as the back contact electrode. A planarization process of a polymerized resist by reactive ion etching enables to uncover the top of the pillar and to establish the top contact electrode [see FIG.(6.1b)]. The top and bottom contact electrodes that sandwich the nano-pillar are shown as red pads in FIG.(6.1a). These pads are impedance matched to allow for high frequency characterization by injecting an RF current through the device. The bottom Cu electrode is grounded and the top Au electrode [red dot on the central pad at the bottom of FIG.(6.1a)] is wire bonded to the central pin of a microwave cable. Hereafter, spectra associated to SW excitations by this part of the microwave circuit will be displayed in red tone. The nano-pillar is also connected through a bias-T to a dc current source and to a voltmeter through the same contact electrodes, that can be used for standard current perpendicular to the plane (CPP-GMR) transport measurements. In our circuit, a positive current corresponds to a flow of electrons from the bottom Py_2 thick layer to the top Py_1 thin layer and stabilizes the parallel configuration due to the spin transfer effect.

The originality of our design is the addition of an independent top microwave antenna, whose purpose is to produce an in-plane microwave magnetic field at the nano-pillar location. In FIG.(6.1a) this part of the microwave circuit is shown in blue. The broadband strip-line microwave antenna consists of a 300 nm thick Au evaporated on top of an insulating layer of polymer that provides electrical isolation from the rest of the structure [see FIG.(6.1b)]. The width of the antenna constriction situated exactly above the nano-pillar is 10 μm. Injecting a microwave current from a synthesizer inside the top antenna produces an homogeneous in-plane linearly polarized microwave magnetic field, oriented perpendicular to the stripe di-

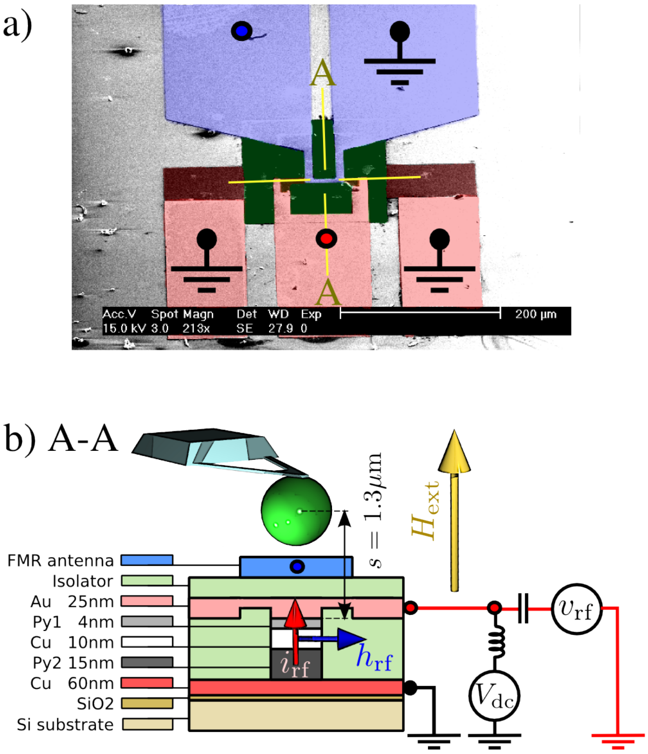

Figure 6.1: (Color online) a) Top view SEM image of the microwave circuit developed for this comparative study about the dynamical behavior of a spin transfer nano-oscillator (STNO). The two independent excitation schemes are shown in different colors. The electrodes in the bottom (red) allow for injecting an RF current perpendicular-to-plane through the nano-pillar. The electrode in the top (blue) enables to produce an RF in-plane magnetic field for standard FMR spectroscopy. The $Py_2/Cu/Py_1$ nano-pillar itself is placed at the center of the cross-hair. b) Section view of the nano-pillar along the A-A axis of the cross-hair. The external magnetic field is applied perpendicularly to the magnetic layers plane. The red and blue arrows show the orientation of respectively the RF current and the RF magnetic field excitations. The mechanical-FMR is inserted above to monitor the dynamics of the buried structure.

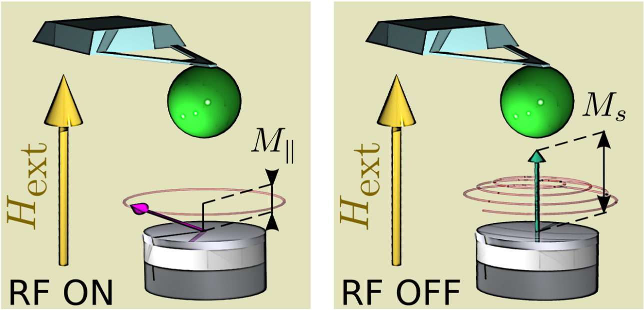

Figure 6.2: (Color online) Schematic representation of the source modulation sequence. The mechanical-FMR measures the change in the time averaged component of the magnetization when the RF is ON ($\overline{M} = M_\parallel$, left) and OFF ($\overline{M} = M_s$, right).

rection [cf. FIG.(6.1b)]. Hereafter, spectra associated to SW excitations by this part of the microwave circuit will be displayed in blue tone.

One parameter that will be important for the indexation of the SW spectra is the radius of the nano-pillar. The nominal value set during the e-beam process is 100 nm, but the exact lateral size obtained at the end of the nano-fabrication process cannot be measured easily, as the nano-pillar is buried under several layers whose total thickness is larger than its diameter. We have therefore used the radius R as the only adjustable parameter in our simulations (see section 6.3). As will be shown below, the best fit value is obtained for $R = 125$ nm, which we will consistently refer to as the radius of our nano-pillar. The discrepancy with the nominal value is within the uncertainty of the nano-fabrication process. Another point is that this parameter represents a dynamical size, which also incorporates the issue of the pinning at the edge of the disk. Because we make no attempt to fit the pinning (we assume that the edge is a node) the fitted value of R represents an effective dynamical radius valid for both disks.

6.2.2 Mechanical-FMR

The nano-fabricated sample is then mounted inside a Magnetic Resonance Force Microscope (MRFM), hereafter named mechanical-FMR [60]. The whole apparatus is placed inside a vacuum chamber (10^{-6} mbar) operated at room temperature. The external magnetic field produced by an electromagnet is oriented out-of-plane, *i.e.*, along the pillar axis $\hat{\boldsymbol{e}}_z$. The mechanical-FMR setup allows for a precise control, within 0.2°, of the polar angle between the applied field and the nanopillar axis. In our study, the strength of the applied magnetic field shall exceed the saturation field (≈ 0.8 T), so that the nano-pillar is studied in the saturated regime. Thus, the local precession axis of the SW excitations is uniformly defined by the unit vector $\hat{\boldsymbol{e}}_z$.

The mechanical detector is an ultra-soft cantilever, an Olympus Biolever having a spring constant $k \approx 5$ mN, with a 800 nm diameter sphere of soft amorphous Fe (with 3% Si) glued to its apex. Standard piezo displacement techniques allows for positioning the magnetic spherical probe precisely above the center of the nano-pillar, so as to retain the axial symmetry. This is obtained when the dipolar interaction between the sample and the probe is maximal, by searching to minimize the cantilever frequency [32].

The mechanical oscillator is insensitive to the rapid oscillation of the transverse component in the sample, which occurs at the Larmor precession frequency, *i.e.*, several orders of magnitude faster than its mechanical resonances. The dipolar force on the cantilever probe is thus proportional to the static component of the magnetization $\overline{M}$ inside the sample, where the overline symbol expresses the time averaged quantity. The latter is equal to the longitudinal component $M_\parallel$ of the magnetization, which for our normally magnetized sample reduces to M_z. We emphasize that for a bi-layer system, the force signal integrates the contribution of both layers. Moreover, the local $M_z(\boldsymbol{r})$ in the two magnetic layers is weighted by the distance dependence of the dipolar coupling to the center of the sphere. In our case this weight is constant because the separation between the sphere and the sample is much larger than the sample dimensions. Hence, the measured quantity is $\langle M_z \rangle$, where the chevron brackets express the spatial average over the full sample volume.

The mechanical-FMR spectroscopy presented below consists in recording by optical means the vibration amplitude of the cantilever as a function of the bias out-of-plane magnetic field at a fixed microwave excitation frequency. This type of spectroscopy is also called cw, for continuous wave, as it monitors the magnetization dynamics in the sample under a forced regime. Actually, a source modulation is applied on the cw signal. It consists in a cyclic absorption sequence, where the microwave power is switched ON and OFF at the cantilever resonance frequency, $f_c \approx 11.85$ kHz. The resulting periodic force signal produces a cantilever vibration amplitude proportional to

$$4\pi\langle \Delta M_z \rangle = 4\pi\langle M_z \rangle_{\mathrm{OFF}} - 4\pi\langle M_z \rangle_{\mathrm{ON}} \tag{6.1}$$

where $\langle M_z \rangle_{\mathrm{OFF}} = M_s$. Thus the signal, recorded by a lock-in detection, is enhanced by the quality factor $Q \approx 2000$ of the mechanical oscillator (see FIG.(6.2). Note that this modulation technique does not affect the line shape in the linear regime, because the period of modulation $1/f_c$ is very large compared to the relaxation times of the studied ferromagnetic system [58, 59]. Since the mechanical-FMR signal originates from the cyclic diminution of the spatially averaged value of the magnetization inside the whole nano-pillar synchronous with the absorption of the microwave power, it detects all possible modes without any selection rules [29]. The force

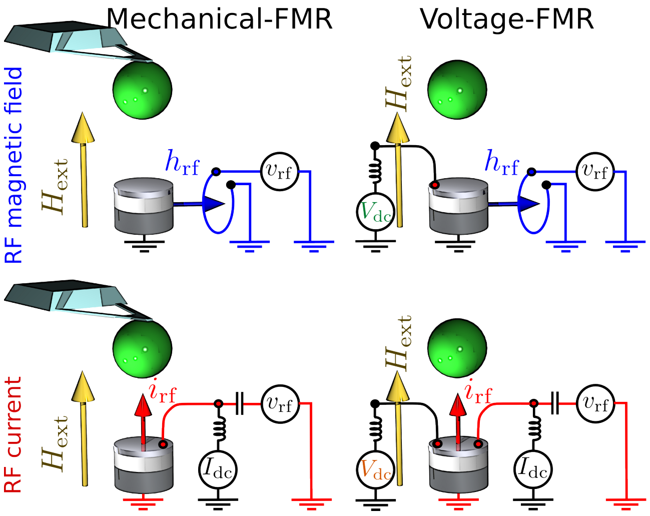

Figure 6.3: (Color online) Schematic representation of the different spectroscopy configurations available with our setup. On the excitation side (arranged by row), two different means are available to put the system out-of-equilibrium: an RF magnetic field applied parallel to the layers (blue arrow) and an RF current flowing perpendicularly to the layers (red arrow). On the detection side (by column), our experimental setup can measure the excitation spectrum by mechanical-FMR (see text) and by voltage-FMR (dc voltage across the pillar). Both detections can be acquired simultaneously, under the exact same bias conditions.

sensitivity of our mechanical-FMR setup is better than 1 fN, corresponding to less than 10^3 Bohr magnetons in a bandwidth of one second for the perpendicular coupling geometry [60].

Finally, we mention that in mechanical-FMR, the magnetic stray field produced by the magnetic sphere modifies the FMR spectra of the sample. In our regime of weak coupling, it simply leads to an overall shift of the full FMR spectra towards lower field [22]. This is in contrast with the strong coupling regime, where the stray field of the magnetic probe can be used to localize SW modes below the MRFM tip [63]. Here, the separation between the center of the spherical probe and the nano-pillar is set to 1.3 μm [see FIG.(6.1b)], which represents an optimum between sensitivity and spectral distortion [60]. The perturbation produced by the sphere is weak as it does not affect the profiles of the intrinsic SW modes in the sample. It reduces to a shift of the peak position by $-\left\{H_{\rm sph}\right\}$, where the curly brackets express a spatial average over the sample volume weighted by the precession profile of the SW mode [60].

In the following, all the mechanical-FMR spectra are recorded with the

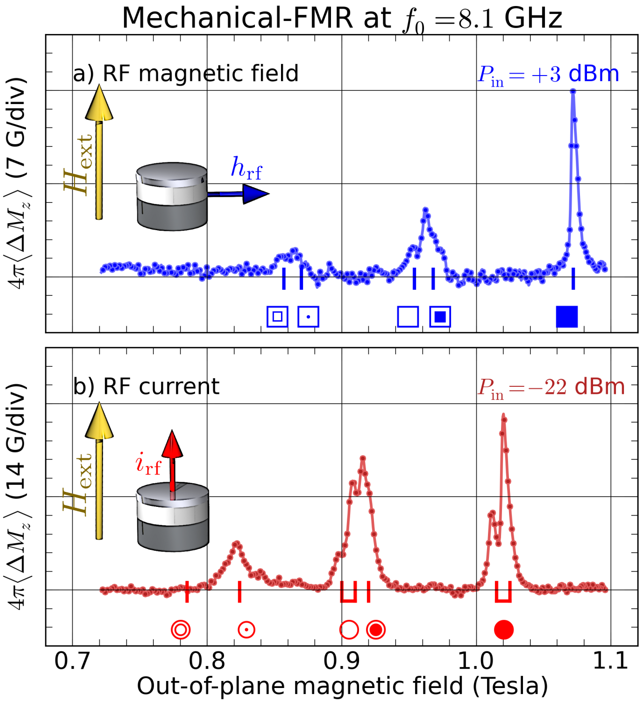

Figure 6.4: (Color online) Comparative spectroscopic study performed by mechanical-FMR at f_0 = 8.1 GHz on the normally magnetized spin-valve nano-pillar. The upper panel (a) shows the SW spectrum excited by a uniform in-plane RF magnetic field. The bottom panel (b) shows the SW spectrum excited by an RF current flowing perpendicularly through the nano-pillar. Blue squares (upper panel) and red dots (lower panel) correspond to the value of the fields at which resonance occurs. The positions of the peaks are reported in Tables 6.2 and 6.3.1.

magnetic sphere at the same exact position above the nano-pillar. To allow for direct comparison, this is also the case for the voltage-FMR spectra, in which the dc voltage produced by the magnetization dynamics accross the nano-pillar is monitored. To symbolize this, we have represented the sphere above the nano-pillar for the voltage-FMR measurement sketched in FIG.(6.3). The shift $-\left\{H_{\rm sph}\right\}$ induced by the probe on the SW spectra can actually be directly measured in the voltage-FMR configuration by removing it from the vicinity of the nano-pillar. This enables to record the intrinsic spectrum and to measure the shift induced by the spherical magnetic probe, found to be $-\left\{H_{\rm sph}\right\} = -190$ Oe.

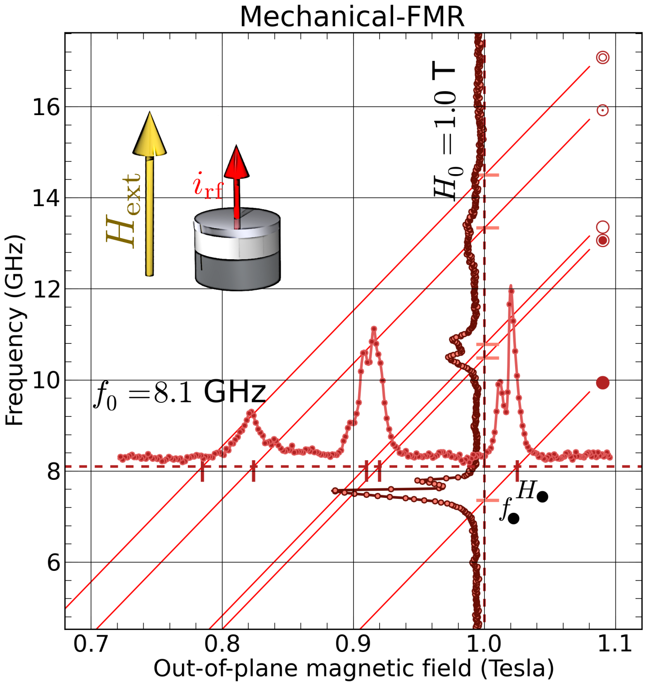

Figure 6.5: (Color online) Frequency-field dispersion relation of $\ell = +1$ modes in the nano-pillar. The horizontal spectrum is the same as in FIG.6.4b, *i.e.*, it is obtained by sweeping the magnetic field at fixed frequency $f_0 = 8.1$ GHz of the RF current $i_{\rm rf}$ through the nano-pillar. The vertical spectrum is obtained at constant bias field $H_0 = 1$ T by sweeping the frequency of $i_{\rm rf}$.

6.2.3 RF magnetic field vs. RF current excitations

The comparative spectroscopic study performed by mechanical-FMR at f_0 = 8.1 GHz on the normally magnetized spin-valve nano-pillar is presented in FIG.(6.4). In these experiments, there is no dc current flowing through the device, and the spectra are obtained in the small excitation regime, *i.e.*, they show the linear response of the magnetic system (precession angles less than 5°) The upper panel (a) shows the SW spectrum excited by a uniform RF magnetic field applied in the plane of the layers, while the lower panel (b) displays the SW spectrum excited by an RF current flowing perpendicularly through the magnetic layers. The striking result is that these two spectra are different: none of the SW modes excited by the homogeneous RF field are present in the spectrum excited by the RF current flowing through the nano-pillar, and vice versa.

Let us first focus on FIG.(6.4a), where the obtained absorption spectrum corresponds to the so-called standard FMR spectrum. Here, the output power of the microwave synthetizer at 8.1 GHz is +3 dBm, which corresponds to a linear amplitude of the uniform RF magnetic field $h_{\mathrm{rf}} \simeq 2.1$ G produced by the antenna. In this standard FMR spectrum, only SW modes with the azimuthal index $\ell = 0$ should appear, as the $\ell \neq 0$ modes cannot couple to a homogeneous RF field excitation due to their vanishing spatial average. In field-sweep spectroscopy, the lowest energy mode occurs at the largest magnetic field. So, the highest field peak at $H_{\blacksquare} = 1.072$ T should be ascribed to the uniform mode, whose indices are $\ell = 0$ and $m = 0$. Since this peak is also the largest of the spectrum, it corresponds to the precession of a large volume in the nano-pillar, *i.e.*, the thick layer is dominating in the dynamics. In mechanical-FMR, a quantitative measurement of the longitudinal magnetization is obtained [69, 29]. For the power level used here, the amplitude of the peak at $H_{\blacksquare}$ corresponds to $4\pi\langle \Delta M_z \rangle \simeq 14$ G, which represents a precession angle $\langle \theta \rangle \simeq 3.1°$. This sharp peak is followed by a broader peak with at least two maxima at $H_{\text{▣}} = 0.968$ T and $H_{\square} = 0.954$ T, and at lower field, by two smaller resonances around $H_{\boxdot} = 0.870$ T and $H_{\text{⧈}} = 0.857$ T. Among these other peaks, there is the uniform mode dominated by the thin layer, which has to be identified and distinguished from higher radial index SW modes. Also, one can notice that the lower field modes are broader than the peak at $H_{\blacksquare}$, suggesting that the higher harmonics modes are subject to some form of inhomogeneous broadening [30]

Let us now turn to FIG.(6.4b), corresponding to the spectroscopic response to an RF current of same frequency 8.1 GHz flowing perpendicularly through the nano-pillar. Here, the output power of the microwave synthetizer is −22 dBm, which corresponds to an rms amplitude of the RF current $i_{\mathrm{rf}} \simeq 170$ μA The SW spectrum is acquired under the *exact same conditions* as for standard FMR, *i.e.*, the spherical magnetic probe of the mechanical-FMR detection is kept at the same location above the sample. The striking result is that the measured spectrum in FIG.(6.4b) is shifted down in field by about half a kilo-Gauss compared to the one in FIG.(6.4a). The lowest energy mode in the RF current spectrum occurs at $H_\bullet = 1.025$ T. This is again the most intense peak, suggesting that the thick layer contributes to it. At this power, $4\pi\langle\Delta M_z\rangle \simeq 26$ G, which represents a precession angle $\langle\theta\rangle \simeq 4.2°$. But the main resonance line is now split in two peaks, with a smaller resonance in the low field wing of the main peak, about 100 G away. At lower field, two distinct peaks appear at $H_{\circledcirc} = 0.920$ T and $H_{\bigcirc} = 0.910$ T and another peak is visible at $H_{\odot} = 0.824$ T.

The fact that the position of the peaks in FIG.(6.4a) and (6.4b) do not coincide implies that the two spectra have a different origin. This is due to the difference in the two methods of excitation, which probe two different ℓ-index symmetries, as it will be confirmed in the next section. In the first experiment, $\ell = 0$ modes are excited by the uniform RF magnetic field of amplitude 2.1 G, whereas in the second experiment, $\ell = +1$ modes are excited by the RF Oersted field induced by the RF current flowing through the nano-pillar, which is about 3.8 G at the periphery and has the appropriate orthoradial symmetry. The uniform and orthoradial RF field symmetries are mutually exclusive, therefore the observed SW modes in the two different cases have no overlap. Still, the two spectra are somewhat in translational correspondence with each other, even though the relative amplitudes between the resonance peaks are different. We shall demonstrate that the reason behind the similarity between the two spectroscopic signatures is that the peaks in translational correspondence bear the same m and a/s indices.

Notice that one can perform spectroscopy at fixed field, to obtain resonance peaks as a function of frequency. The evolution of the $\ell = +1$ modes is presented in FIG(6.5). Here, we took the advantage of the broadband design of the electrodes that connect the nano-pillar to measure the FMR spectrum at a fixed bias magnetic field H_0, by sweeping the frequency of the RF current through it. It allows for a direct check of the equivalence between frequency and field sweep experiments in the normally saturated state. (We note that the same frequency-sweep experiment cannot be performed as cleanly with the RF field excitation due to the high power that has to be injected in the microwave antenna and to some impedance mismatch). In our micromagnetic simulations resonance peaks are calculated as a function of frequency.

6.2.4 Direct bias current

To gain further insight about the peak indexation, we have measured the spectral deformations produced on the SW spectra of FIG.6.4 when a finite dc current $I_{\mathrm{dc}} \neq 0$ is injected in the nano-pillar. We recall that for our sign convention, a positive dc current stabilizes the thin layer and destabilizes

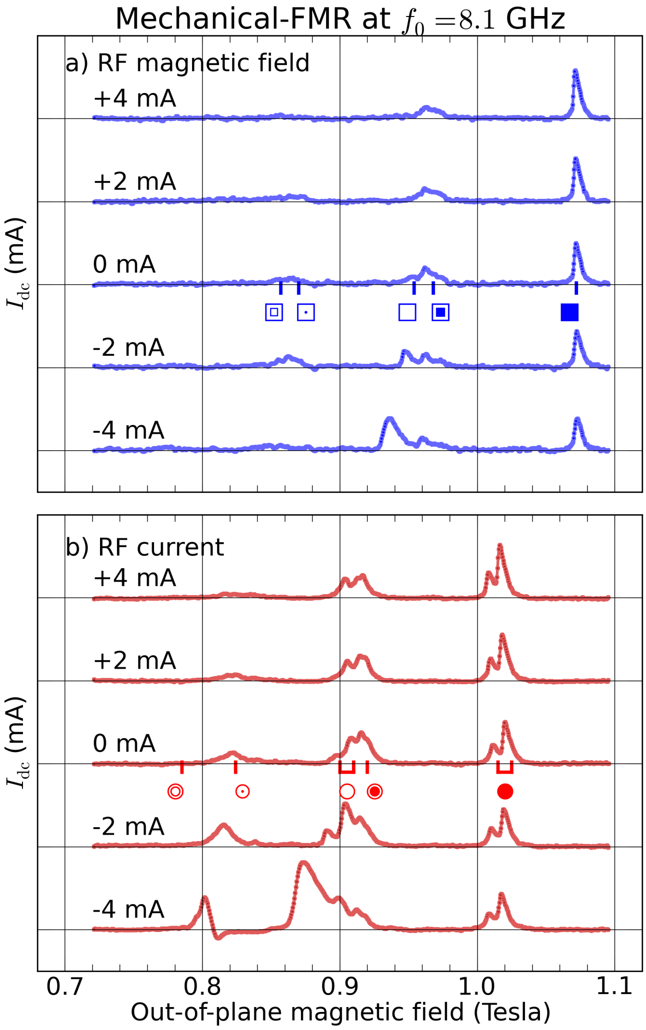

Figure 6.6: (Color online) Evolution of the SW spectra measured at f_0 = 8.1 GHz by mechanical-FMR for different values of the continuous current I_{dc} flowing through the nano-pillar. The upper panel (a) corresponds to excitation by a uniform RF magnetic field [as in FIG.(6.4a)], and the lower panel (b) to excitation by an RF current through the sample [as in FIG.(6.4b)]. Blue squares (upper panel) and red dots (lower panel) correspond to the value of the fields at which resonance occurs.

the thick one due to the spin transfer torque, and vice versa [88, 9]. The results obtained by mechanical-FMR are reported in FIG.6.6.

Let us first concentrate on FIG.(6.6a), in which the excitation that probes the different SW modes is the same as in FIG.(6.4a), *i.e.*, a uniform RF magnetic field $h_{\mathrm{rf}} \simeq 2.1$ G. Two main features can be observed in the evolution of the SW spectra as I_{dc} is varied. First, the amplitude of the peak at $H_{\blacksquare}$ smoothly increases with the positive current and smoothly decreases with the negative current. At the same time, the peak at $H_{\square}$, which is about five times smaller than the peak at $H_{\blacksquare}$ when $I_{\mathrm{dc}} = 0$ mA, almost disappears for positive current and strongly increases at negative current, until it becomes larger than the peak at $H_{\blacksquare}$ when $I_{\mathrm{dc}} = -4$ mA. These two features are consistent with the effect of spin transfer if we ascribe the peak at $H_{\blacksquare}$ to the uniform mode of mostly the thick layer and the peak at $H_{\square}$ to the one of mostly the thin layer. More precisely, it is expected that in the sub-critical regime ($I_{\mathrm{dc}} < I_{\mathrm{th}}$, where I_{th} is the threshold current for auto-oscillations, $I_{\mathrm{th}} < 0$ for the thin layer and $I_{\mathrm{th}} > 0$ for the thick layer), the effective damping d scales as $\alpha_{\mathrm{LLG}}(1 - I_{\mathrm{dc}}/I_{\mathrm{th}})$ [82, 24]. It means that the linewidth of a resonance peak that is favored by spin transfer should decrease as the current gets closer to I_{th}, and that its amplitude, which scales as $1/d$, should increase.

Although the effect on the peak amplitude noted above is clear in FIG.(6.6a), it is not on the linewidth. The reason is that in this experiment, the strength of the driving RF magnetic field is kept constant to 2.1 G. As a result, the shape of the growing peaks in FIG.(6.6a) becomes quite asymmetric, which is a signature that the driving field is strong enough to change the internal field by an amount of the order of the linewidth. This leads to some foldover of the resonance line [4, 83]. In other words, the distortion of the line shape as the peak amplitude increases prevents to see the diminution of its linewidth [25]. It would be necessary to decrease the excitation amplitude as the threshold current is approached [24] so as to maintain the peak amplitude in the linear regime in order to reveal it.

The opposite signs of the spin transfer torques which influence the dynamics in the thin and thick layers are clearly seen in FIG.(6.6a). Their relative strengths can also be determined, as the efficiency of the spin transfer torque is inversely proportional to the thickness of the layer. In fact, the amplitude of the peak at $H_{\square}$ grows much faster with the negative current than the one of the peak at $H_{\blacksquare}$ with the positive current. Whereas the precession angle in the thick layer does not vary much with I_{dc} (from $\approx 2.5°$ at -4 mA to $\approx 3.5°$ at $+4$ mA), the precession angle that can be deduced from $\langle \Delta M_z \rangle$ in the thin layer grows from almost zero at $I_{\mathrm{dc}} = +4$ mA to more than $11°$ at $I_{\mathrm{dc}} = +4$ mA. Moreover, the peak position $H_{\square}$ shifts clearly towards lower field as the negative current is increased. This is due to the onset of spin transfer driven auto-oscillations in the thin layer, which occurs at a threshold current $-4 < I_{\mathrm{th}} < -3$ mA, and that produces this non-linear shift

[85].

Let us now briefly discuss FIG.(6.6b), which shows the same dependence on I_{dc} of the mechanical-FMR spectra excited by an RF current excitation of rms amplitude $i_{\mathrm{rf}} \simeq 170\ \mu\mathrm{A}$ [same as in FIG.(6.4b)]. Here again, a clear asymmetry is revealed depending on the polarity of I_{dc} and on the SW modes. The double peak at $H_{\bullet}$ is favored by positive currents, hence it should be ascribed to mostly the thick layer precessing, while the double peak at $H_{\bigcirc}$ is strongly favored by negative curents, hence it should be ascribed to mostly the thin layer precessing.

To summarize, the passage of a dc current through the nano-pillar enables to determine which layer mostly contributes to the observed SW modes, owing to the asymmetry of the spin transfer effect. However, the detailed understanding of the coupling between the two layers requires micromagnetic simulations, which will be presented in the next two sections. At first we will focus on micromagnetic simulations without taking into account spin transfer, then we shall add spin torque coupling CRMT to the micromagnetic software. This shall lead to a precise identification of the modes excited by spin torque and of their critical current.

6.3 Micromagnetic simulations at $I_{\mathrm{dc}} = 0$

We have performed below a more complete calculation of the predicted SW spectrum inside our sample with $I_{\mathrm{dc}} = 0$ using an open source micromagnetic simulation package: Nmag [37]. Nmag is a finite element solver based on the general purpose multi-physics library Nsim. It is developed by the group of Hans Fangohr and Thomas Fischbacher in the School of Engineering Sciences at the University of Southampton.

In this simulation, the full three-dimensional dynamics of the bi-layer system is calculated. The thin layer is discretized with a mesh size equal to 4 nm (its thickness) while the thick layer is discretized with a mesh of 3 nm. The numbers of nodes used in the simulation are respectively 6135 in the thin layer and 37598 in the thick layer. The magnetic parameters introduced in the code are the ones extracted in FMR experiment (Table 6.1). The magnetization vector is assumed to be uniform inside each cell. This approximation is valid because the cell size is smaller than the exchange length $\Lambda = 5$ nm in Permalloy. The simulation incorporates the perturbing presence of the sphere attached on the cantilever. In this first part we neglect any spin-diffusion effects between the layers: the 10 nm thick Copper layer is replaced in the simulation by a vacuum spacer. Below we shall describe how to simulate the presence of the Cu spacer using CRMT.

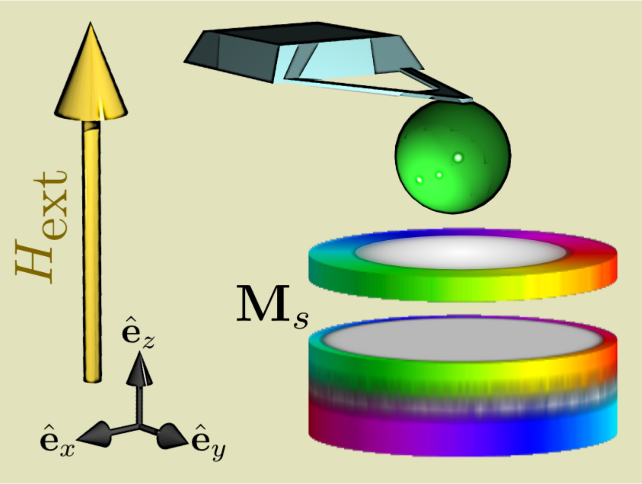

Figure 6.7: (Color online) Color representation of the static configuration of the magnetization inside the nano-pillar. In this micromagnetic simulation, the external magnetic field $H_{\mathrm{ext}} = 1$ T is applied along the normal $\hat{\boldsymbol{e}}_z$, and the magnetic spherical probe is taken into account. The white regions at the center of each disk correspond to the magnetization being aligned along the normal within 0.05°. In the colored regions at the periphery, the magnetization is twisted, with the hue indicating the direction of the static transverse component.

$4\pi M_1$ (G)	α_{LLG1}	$4\pi M_2$ (G)	α_{LLG2}	γ (rad.s^{-1}.G^{-1})
8.0×10^3	1.4×10^{-2}	9.6×10^3	0.85×10^{-2}	-1.87×10^7

Table 6.1: Physical parameters of the thin (1) and thick (2) Permalloy layers measured by mechanical-FMR in the nano-pillar.

$H_{\blacksquare}$	$H_{▣}$	$H_{\square}$	$H_{\boxdot}$	$H_{⧈}$
1.072 T	0.968 T	0.954 T	0.870 T	0.857 T
$a_{0,0}$	$a_{0,1}$	$s_{0,0}$	$s_{0,1}$	$a_{0,2}$
5.96 GHz	8.89 GHz	9.77 GHz	11.91 GHz	12.15 GHz
1.072 T	0.973 T	0.944 T	0.872 T	0.864 T

Table 6.2: Comparative table of the resonance fields of the $\ell = 0$ SW modes. Top are the peak locations measured experimentally in the SW spectrum excited by a uniform RF field at $f_0 = 8.1$ GHz [see FIG.(6.4a)]. Middle are the eigen-frequencies extracted from the simulation at $H_0 = 1$ T. Bottom are the corresponding fields through the affine transformation Eq.(6.4).

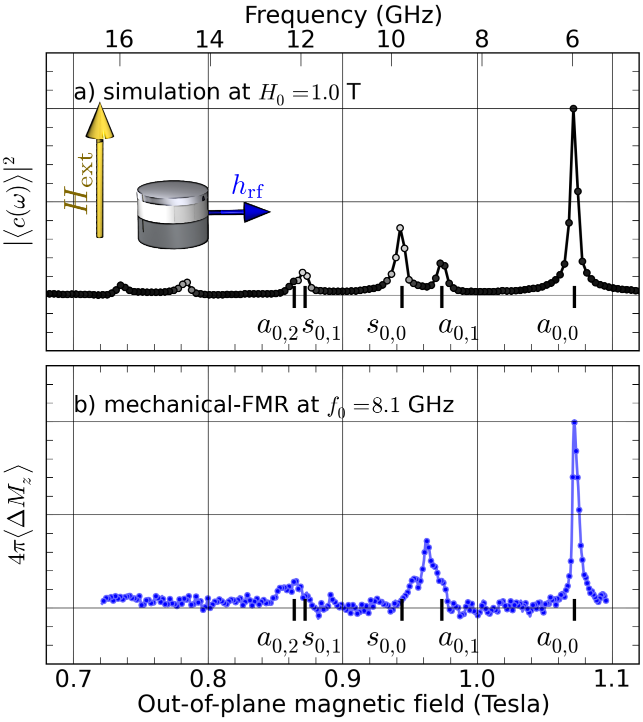

Figure 6.8: (Color online) Comparison between the simulated dynamics with the $\ell = 0$ symmetry at $H_0 = 1$ T (a) and the experimental SW spectrum excited by a uniform RF magnetic field at $f_0 = 8.1$ GHz (b). The simulated spectrum is the Fourier transform of the time evolution of $\langle c(t)\rangle = (\langle M_x - iM_y\rangle)/(2M_s)$ averaged over the whole sample volume [the frequency is convered into field through the affine transformation Eq.(6.4)]. The contribution of each layer is displayed by the contrast of the circle symbols in the plot: a light (dark) circle indicates that the dynamics mostly occurs in the thin (thick) layer. The peaks are labeled according to their precession profiles shown in FIG.(6.9).

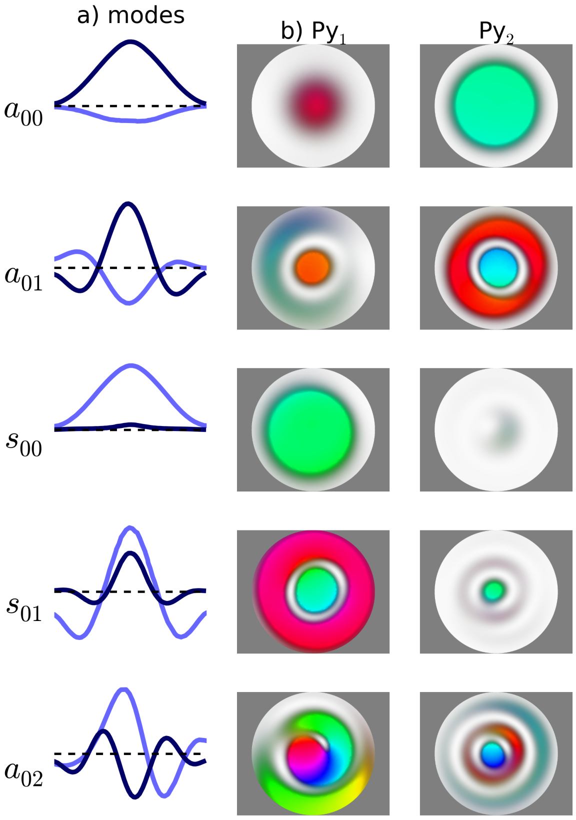

Figure 6.9: (Color online) Simulated precession patterns at the eigen-values displayed in FIG.(6.8a). Column (a) shows the precession profiles across the thin (light blue) and thick (dark blue) layer. Columns (b) and (c) show the dynamics in respectively the thin and thick layers, with the same color code as FIG.(5.7).

6.3.1 Identification of the SW modes

Our first step is to calculate the equilibrium configuration of the normally magnetized nano-pillar with the added presence of a spherical probe carrying the magnetic moment 2×10^{-10} emu and placed at a separation distance 1.3μm above the upper surface of the nano-pillar on the axis center [see FIG.(6.1b)]. The calculation is done in an external bias magnetic static field of $H_0 = 1$ T applied exactly along the disk axis. The convergence criteria introduced in the code was that $dm/dt < 1°/$ns. The result is shown in FIG.(6.7) revealing the twisted state at the periphery. The amount of tilt is less than 0.5 degree compared to the normal and the most tilted region is located at the bottom interface of the thick layer.

Starting from the equilibrium state, we then calculate the time decay response of the local magnetization to a small perturbation of the magnetic configuration. Two different initial conditions are simulated. In the first case, we have used the following perturbation vector field:

$$\boldsymbol{\varepsilon}_M(r,z) = \vartheta \sum_{m<6} J_0(k_{0m} r)\hat{\boldsymbol{e}}_x \qquad (6.2)$$

This form corresponds to an excitation that put the same energy in the lowest 6 m-index modes. At instant $t = 0$, we add, at every mesh, to the local unit vector along the equilibrium magnetization, the small perturbation vector defined in Eq.(6.2) and the initial condition becomes $\hat{\boldsymbol{e}}_M = \hat{\boldsymbol{e}}_{\overline{M}} + \boldsymbol{\varepsilon}_M$. The angle $\vartheta = 0.01 \ll 1$ corresponds to a small variation from the local equilibrium axis of less than $1°$ degree. Such value is small enough to ensure that non-linear effects are not dominant in the simulated spectrum. The symmetry of the perturbation field used in Eq.(6.2) corresponds to a uniform tilt (*i.e.* in same azimuthal direction) of the magnetic moments located near the center of the disk. Such symmetry of the perturbation field reproduce the symmetry used during the RF magnetic field excitation sequence. One thus expect to reveal the SW spectrum projected along the $\ell = 0$-index. We then simulate the magnetization decay inside the whole sample. The decay is recorded in a 10 ns time window with a sampling interval of 5 ps. At every time step, the spatial average of the in-plane component of the magnetization is recorded. For each layer $j = 1, 2$, we cconsider the complex reduced magnetization

$$\langle c_j(t)\rangle = (\langle M_{jx}(t)\rangle - i\langle M_{jy}(t)\rangle)/(2M_j) \qquad (6.3)$$

inside the layer. A complex Fourier transform of c leads to the frequency spectrum of the magnetization decay. In order to compare it to the experimental data, where the spectrum is recorded as a function of field [see FIG.(6.8b)] we have applied the affine transformation to the frequency data

$$H = \frac{2\pi}{\gamma}(f - f_0) + H_0 \qquad (6.4)$$

where $f_0 = 8.1$ GHz is the RF frequency used in the measurement and H_0 is the static field used in the simulations. Such linear correction assumes that the sample is well into the saturation regime. This is valid above 0.8 T and discrepancies between the simulation and the mechanical-FMR data are expected below this threshold. FIG.(6.8a) shows the power density spectrum of the time decay of the full averaged reduced magnetization $\langle c \rangle = (\langle c_1 \rangle t_1 + \langle c_2 \rangle t_2)/(t_1 + t_2)$, where t_1 and t_2 represent respectively the thickness of the thin and thick layer. The eigen-values of all the peaks are reported in Table.6.2. Since we also have access to the spectrum inside the individual layer, we have indicated the contribution of each layer to the simulated spectrum by modulating the contrast inside the circle symbols in the plot. A light circle indicates resonance which mostly occur in the thin layer, while dark circle indicate resonance which occur mostly in the thick layer. The first two peaks are thus resonances occurring in the thick layer, while the third peak is a resonance occurring in the thin layer. We emphasize at this point that the relative amplitude between the peaks in the simulated spectrum have no intrinsic meaning since it depends on the form of the perturbation field. In contrast to the amplitude of the peaks, the relative phase and the relative amplitude of the precession between the two magnetic layers give an insight about the coupled dynamics.

The first peak of the spectrum labeled $a_{0,0}$ occurs at the same field location as the peak at $H_{\blacksquare}$ observed experimentally. In order to visualize the corresponding precession profile, we have registered the spatial orientation of the transverse magnetization in the rotating frame at each eigen-values of the spectrum. This is obtained by calculating the Fourier transform of the quantity c at every mesh. The results are shown in FIG.(6.9) using different representations. The first column shows the precession profile along the median direction in the thin (light blue) and in the thick (dark blue) layer. A 2D view of the spatial distribution of the transverse magnetization is shown in the two right columns of FIG.(6.9), respectively for both the top and bottom layer, using the normalized color scale defined in section 5.4, where the hue indicates the phase (or direction) of the transverse component of the magnetization $M_\perp$, while the brightness indicates the amplitude of the longitudinal component, $M_\parallel$. From the color code panel, we see that all the modes of FIG.(6.9) have the same phase along the azimuthal direction and thus they should all bear the same index $\ell = 0$. The lowest energy mode corresponds to the most uniform mode with the largest wave-vector. This mode is also associated with a small uniform resonance in the thin layer. This mode thus has the index $m = 0$. From the phase between the two dynamic susceptibility, one observes that the two modes between the thick and the thin are oscillating in antiphase. In summary the spatial profile shown in FIG.(6.9) confirms the lowest energy mode should be labeled a_{00} since this mode bears the indices a (mode anti-symmetric), $\ell = 0$ and $m = 0$. The second peak labeled a_{01} occurs close to the peak $H_{\boxdot}$. This peak corresponds also to a resonance in the thick layer, and the color representation of the local power absorption shows that this is the first harmonic ($m = 1$), with one line of node in the radial direction. Again the two layers are oscillating in antiphase as clearly shown by the profile along a median direction. The profile also shows that this mode is coupled to the first harmonic of the thin layer ($m = 1$). We emphasize once more that the relative phase between two different modes has no intrinsic signification since it depends on the initial condition. We find, however, that despite our initial condition which synchronize all the modes at $t = 0$, the center of the disks of the thick layer does not rotate exactly at the same phase between the two patterns shown for the two modes a_{00} and a_{01}. We associate this difference to small error in the sampling of the fourier spectrum. A more proper comparison should look at the phase at exactly the resonance (or maximum of the peak). The third peak is labeled $s_{0,0}$ and it located close to the peak at $H_\square$. It corresponds this time to a uniform ($m = 0$) precession mainly located in the thin layer. This is again in agreement with the observed spectrum in FIG.(6.8b). The mode $s_{0,0}$ corresponds this time to the two layers vibrating symmetrically. We observe that the simulated pattern of the $s_{0,0}$ slightly violates the cylindrical symmetry both in the thin and in the thick layer. Since there is nothing in our problem that should produce this asymmetry, we ascribe this effect to the limit of the software and to a problem of propagation of errors (the resolution set in the program is 10^{-7}). Although the asymmetry is significant, we do not expect this to change much the predicted eigen-value for this mode.

The simulation works shown above also allow an estimation of the amount of dynamical coupling between the disks. From the profiles shown in FIG.(6.9), one can infer that in the case of the fundamental mode, a_{00}, the amplitude of precession is distributed in the ratio of 81% contribution from the thick layer and 19% contribution from the thin layer. This illustrates dramatically that although the spectral deformation are of the order of the linewidth, the excitation of the adjacent layer is not small. This characteristics must be weighted by the thickness of the layer, and this ratio drops for symmetric modes (modes of the thin layer). In the case of the mode s_{00}, the relative weight drops to a ratio of 92% contribution from the thin layer and 8% contribution from the thick layer. From these values one can estimate the amount of field created by the layers one another.

As a check, another simulation has been performed by F. Boust and N. Vukadinovic using a software base on finite differences. The dynamical susceptibility spectra of the two Py disks has been simulated by a micromagnetic code developed by S. Labbé [61] and later by F. Boust and N. Vukadinovic [13, 100]. In this approach, the disk volume is discretized by a regular cubic mesh of total size $128 \times 128 \times 16$, where each cube has an edge size of 2 nm. Two 3D codes are used to calculate the dynamical response. The first code calculates the stable configuration of the magnetization vector $\boldsymbol{M}(\boldsymbol{r})$ at $H_0 = 1$ T by solving the Landau-Lifshitz equation in the time domain. In this simulation, the presence of the perturbing sphere of the MRFM was not directly incorporated in the code and instead a constant offset of 0.57 GHz (corresponding to an offset field of 190 G) was added to all the eigen-values. The second code computes the full dynamic susceptibility tensor $\hat{\chi}$ from the linearization of the Landau-Lifshitz equation around the local equilibrium configuration. The used material parameters are identical to the ones used by Nmag. This code has been used to calculate the eigen-value of the three lowest energy modes having the $\ell = 0$ symmetry. The calculated eigen-value for the mode a_{00} is 5.9 GHz while the calculated eigen-value for the mode s_{00} is 9.7 GHz. These values are in good agreement with the ones obtained by the Nmag micromagnetic code (see Table 6.2). The predicted eigen-value of the mode a_{01} is 8.7 GHz, a value somewhat different from the result of Nmag, but the difference is attributed to the approximation made, where a constant offset has been used to account for the stray field of the sphere instead of doing the complete perturbation of the perturbing influence [22]. These simulations also confirm the amount of dynamical dipolar coupling. In the case of the fundamental mode, a_{00}, the two layers vibrate anti-symmetrically and the amplitude of precession is distributed in the ratio of 79% contribution from the thick layer and 21% contribution from the thin layer. In the case of the mode s_{00}, the relative weight drops to a ratio of 91% contribution from the thin layer and 9% contribution from the thick layer. From these values one can estimate the amount of field created by the layers one another.

Finally, one can also extract from the simulations the thickness dependence of the precession profile. We find that the profile is thickness independent within the uncertainty of the calculated profile which is about ±2%. This confirms the validity of the 2D approximation, and it explains why the analytical model works so well in the prediction of the resonance location.

We have repeated the same simulation, but this time using an orthoradial perturbation field. Starting again from the equilibrium configuration, we add at $t = 0$ the following perturbation field at each node of the mesh:

$$\boldsymbol{\varepsilon}_M(r,z) = \vartheta \sum_{m<6} J_1(k_{1m} r)\hat{\boldsymbol{e}}_r \times \hat{\boldsymbol{e}}_z \tag{6.5}$$

where $\hat{\boldsymbol{e}}_r$ is the unit vector along the radial direction. The value of $\vartheta = 0.01 \ll 1$ is identical. The symmetry of the perturbation reproduces the one induced by the Oersted field of a current flowing perpendicular to the layers. One thus expect to reveal the SW spectrum projected along the $\ell = +1$-index. Again we monitor the time decay of the transverse magnetization but this time we record the spatial average of $\langle c \exp^{-i\phi} \rangle$, where ϕ is the local azimuthal coordinate of the node of the mesh. In other words, we have calculated the spatial average of the cylindrical component of the magnetization in cylindrical coordinates (instead of cartesian). The power density

$H_{●}$, $f_{●}$	$H_{◉}$, $f_{◉}$	$H_{○}$, $f_{○}$	$H_{⊙}$, $f_{⊙}$	$H_{◎}$, $f_{◎}$
1.025 T	0.920 T	0.910 T	0.824 T	0.785 T
7.37 GHz	10.48 GHz	10.92 GHz	13.41 GHz	14.20 GHz
$a_{1,0}$	$a_{1,1}$	$s_{1,0}$	$s_{1,1}$	$a_{1,2}$
7.32 GHz	10.45 GHz	11.04 GHz	13.48 GHz	14.06 GHz
1.026 T	0.921 T	0.902 T	0.826 T	0.800 T

Table 6.3: Comparative table of the resonance fields and frequencies of the $\ell = +1$ SW modes. Top are the field peaks measured experimentally in the SW spectra excited by an RF current at $f_0 = 8.1$ GHz [see FIG.(6.4b)]. Second line are the experimental frequency peaks measured at $H_0 = 1$ T by sweeping the frequency of the RF current [see FIG.(6.10b]. Third line are the eigen-frequencies extracted from the simulation at $H_0 = 1$ T. Bottom are the corresponding fields through the affine transformation Eq.(6.4).

spectrum shown in FIG.(6.10) represents the dynamics observed under the forced oscillation with $\ell = +1$.

Using the same procedure as above, we have also reported in FIG.6.11 the precession profile as well as a color map of the mode pattern using the same color code convention. The striking new feature of these spectra is the rotating phase in the azimuthal direction, characteristics of the $\ell = +1$ modes. Both sense of rotation are identical compared to the Larmor direction of precession. In the representation of FIG.(6.11) where what is shown is both a top and a bottom view projection of the nano-pillar stack, the images give rise to apparently inverted sense of rotation between the two layers. Repeating the analysis above concerning the a/s and m index, we demonstrate that the labelling of the simulated spectra is clearly consistent with the images provided.

6.4 Micromagnetic simulations at $I_{dc} \neq 0$

Micromagnetic simulations that take into account spin transfer effect are necessary to describe the dynamics in presence of a bias dc current, and the associated selection rules of SW modes. In this section we shall describe a method, based on CRMT, to include spin torque into Nmag computations.

Calculations of current driven dynamics in our nanopillar have been already performed by our group one of our group (V. Rychkov), whithin a macrospin approximation. In this model, one approximates the magnetization texture in each layer with a single magnetization vector. The dynamics of the nanopillar is calculated solving numerically two LLG equations (one for each layer) coupled through dipolar interaction, that include spin torque calculated with CRMT. This approximation allows to describe magnetore-

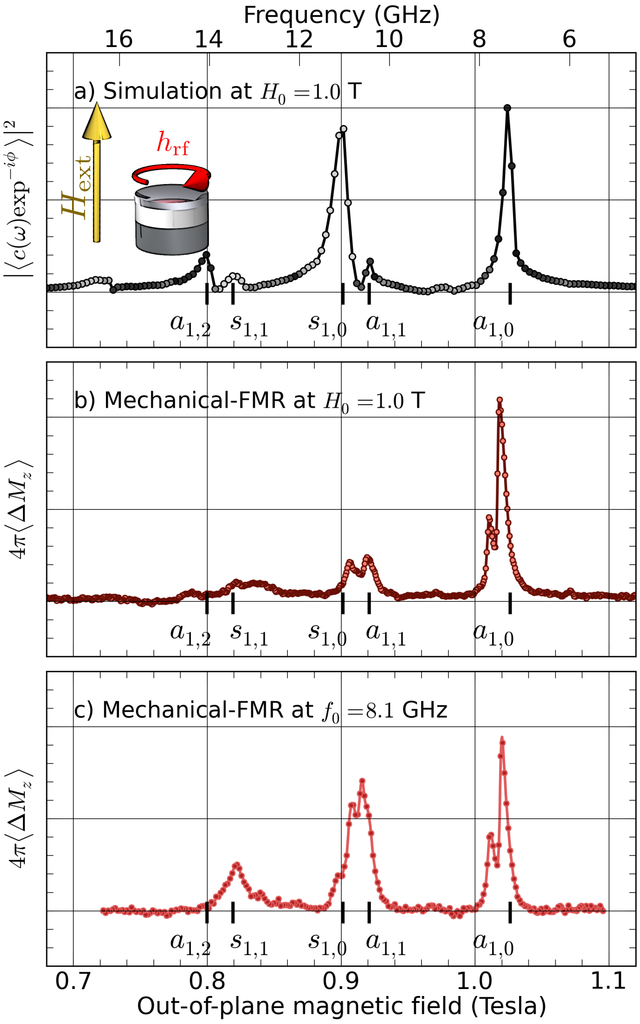

Figure 6.10: (Color online) Comparison between the simulated dynamics with the $\ell = +1$ symmetry at $H_0 = 1$ T (a), the experimental frequency-sweep SW spectrum excited by an RF current through the nano-pillar at $H_0 = 1$ T (b), and the corresponding field-sweep experimental SW spectrum at $f_0 = 8.1$ GHz (c). The simulated spectrum is the Fourier transform of the time evolution of $\langle c(t)\exp^{-i\phi}\rangle$ averaged over the whole sample volume [the frequency is converted into field through the affine transformation Eq.(6.4)]. The contribution of each layer is displayed by the contrast of the circle symbols in the plot: a light (dark) circle indicates that the dynamics mostly occurs in the thin (thick) layer. The peaks are labeled according to their precession profiles shown in FIG.(6.11).

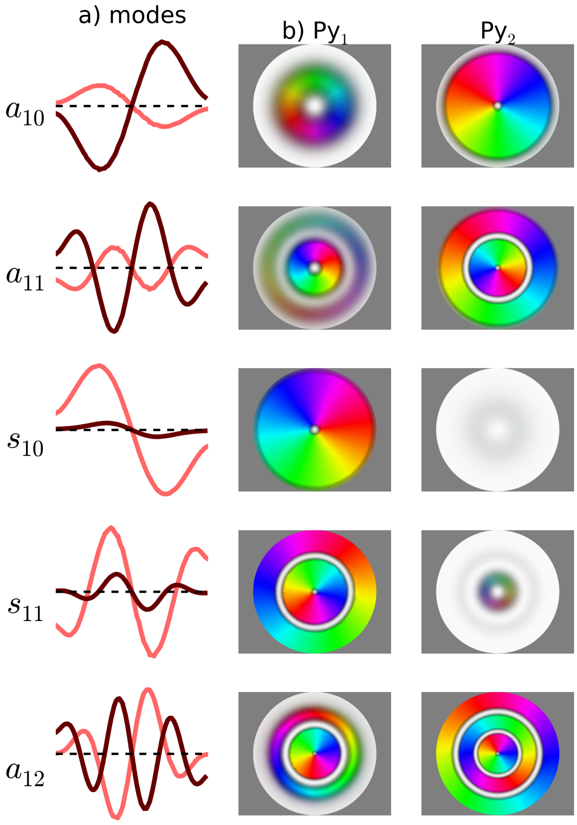

Figure 6.11: (Color online) Simulated precession patterns at the eigen-values displayed in FIG.(6.10a). Column (a) shows the precession profiles across the thin (light red) and thick (dark red) layer. Columns (b) and (c) show the dynamics in respectively the thin and thick layers, with the same color code as FIG.(5.7).

sistive effect, but it cannot describe SW modes, which related to spatial inhomogeneity of the magnetization.

In our simulation we have moved one step further, considering a fully three dimensional texture of the magnetization, and including transport only along $\hat{\boldsymbol{e}}_z$ (neglecting lateral diffusion of electrons). When the simulations described in this work were performed, CRMT was a 1D transport theory, and a three dimensional extension of CRMT theory was under development. Our approach is an intermediate step towards micromagnetic simulation that incorporate a 3D theory of transport. Anyway, even in our simplyfied picture, the selection rules associated to spin torque excitations have been described correctly.

Since CRMT is tabulated with the same set of experimentally accessible parameters as the Valet-Fert theory [see Sec.(3.4)] our method is suitable for a large variety of materials. The algorithm to couple CRMT to Nmag that we shall describe below can be easily adapted to geometries different than a cylinder.

The starting point to include spin torque in our micromagnetic simulation, consists in modifying the LLG equation at each node i of the Nmag mesh as follows:

$$\frac{d\hat{\boldsymbol{e}}_{Mi}}{dt} = -\gamma(\hat{\boldsymbol{e}}_{\boldsymbol{M}i} \times \boldsymbol{H}_{\mathrm{eff},i}) - \alpha\left(\hat{\boldsymbol{e}}_{Mi} \times \frac{d\hat{\boldsymbol{e}}_{Mi}}{dt}\right) + \boldsymbol{\tau}_i/M, \tag{6.6}$$

Here M is the saturation magnetization, $\hat{\boldsymbol{e}}_{Mi} = \boldsymbol{M}_i/M$ is the normalized magnetization, $\boldsymbol{\tau}_i$ is the non equilibrium spin torque, and $\boldsymbol{H}_{\mathrm{eff}\,i}$ is the effective field at site i, which takes into account the coupling with neighbouring sites due to dipolar and exchange interaction as well as the external field. Hereafter we shall describe how to include the torque $\boldsymbol{\tau}_i$, calculated with CRMT, in the LLG equation resolved by Nmag.

6.4.1 Coupling CRMT to Nmag

Magnetization and spin torque are strongly coupled: at each instant, the magnetic configuration determines spin torque, which influences the successive dynamics. In our numerical simulations, spin torque has to be included into Nmag solver as follows:

1. At time t and site i Nmag computes the vector $\hat{\boldsymbol{e}}_{Mi}(t)$, and CRMT the torque $\boldsymbol{\tau}_i(t)$

2. the quantity $\hat{\boldsymbol{e}}_{Mi}(t) + \boldsymbol{\tau}_i(t)dt$, ($dt$ being the integration time step) is set as new initial condition for the Nmag integrator at time t.

3. Nmag performs the time integration of the LLG equation between the time t and $t + dt$, when spin torque is calculated anew and the whole procedure starts again.

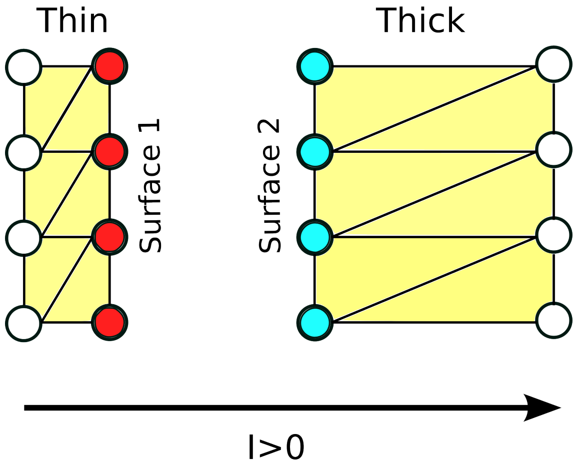

Figure 6.12: A cartoon of the system, where circles represent the sites and the lines that connect them represent the mesh. The two permalloy disks are viewed from profile, with the current flowing along the z axis. Spin torque acts directly only on the sites lying at surfaces 1 and 2: these are the only sites for which the LLG equation has to be modified according to Eq.(6.6). The other sites are affected by spin torque via exchange and dipolar interaction. Different colours have been chosen for surface sites to stress the fact that the torque is different in surfaces 1 and 2.

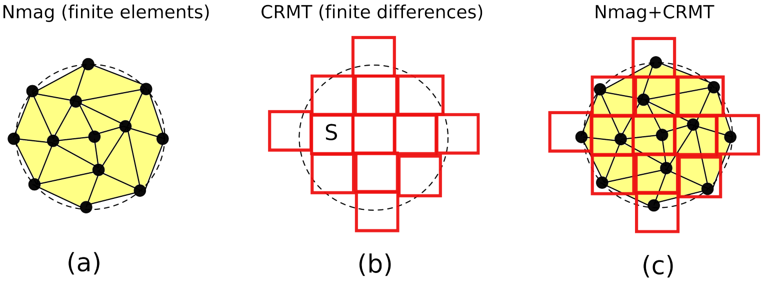

Figure 6.13: Different simplified representation of our system. In fig. (a) the disk is discretized using finite elements where each dot consists in a site i with magnetization $\hat{\boldsymbol{e}}_{Mi}$, connected to the other sites through an irregular mesh. In fig. (b) the same disk is discretized using finite differences, as an assembly of pillars (represented by red squares) connected in parallel, each one with the same cross section S. Fig. (c): each CRMT pillar contains one site lying at the surface. See text for details about the coupling between CRMT and finite element representation.

Since the penetration length of transverse spins is about 2-3 nm, [see section (4.4.1)], spin torque acts only at the surfaces of the two disks that face (hereafter referred as surface 1 and 2 for thin and thick layer respectively). For meshes bigger than 3 nm, torque acts only the sites lying on those surfaces, and we consider that spin torque depends only on the magnetic configurations of these sites. We shall describe the points of surfaces 1 and 2 using Eq. (6.6), and all the other points with the LLG equation whithout spin torque. A schematic of this simplification is shown in FIG.(6.12).

To perform this computation we need to associate to each site i a CRMT system. For this purpose we consider the Nmag system as divided into columns of sites, each column K representing a CRMT pillar with cross section S_K. The nanopillar is viewed as an assembly of these columns connected in parallel, and spin torque has to be calculated in each column using CRMT, and then associated to the sites lying on the column. This "CRMT representation" of the system is based on finite differences, which consist into discretization of space in regular cubic cells. Nmag is based on finite elements, where space is discretized with irregular triangles or thetraedra that connect the sites. Our algorithm consists in a method to divide the system, that couples these different representations [see FIG.(6.13)].

To calculate spin torque, let us consider the column K shown in FIG.(6.15) This column contains one site at surface 1 and one site at surface 2 At time t these sites have magnetizations $\hat{\boldsymbol{e}}_{M1}(t)$ and $\hat{\boldsymbol{e}}_{M2}(t)$, which form an angle θ. Using CRMT we calculate the corresponding torques. For example, the torque $\boldsymbol{\tau}_1(\theta)$ acting on $\hat{\boldsymbol{e}}_{M1}$ reads:

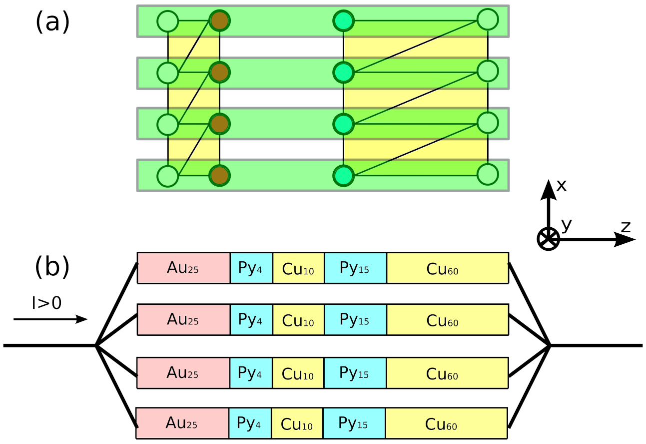

Figure 6.14: A schematic of the technique used to divide the system (viewed from provile, with current flowing in the z direction) into an assembly of one dimensional columns, each one described using CRMT. (a) The columns of sites inside the system are identified (see text for details). (b) In CRMT representation, the system is described as an assembly of columns *connected in parallel.* Spin torque and resistance is calculated in each CRMT column. Notice that Nmag does not consider normal materials, while in CRMT they are included (since they influence electronic transport).

$$\boldsymbol{\tau}_1^{crmt} = \frac{1}{4\pi} N_{ch} f_1(\theta) eU [\hat{\boldsymbol{e}}_{M1} \times (\hat{\boldsymbol{e}}_{M1} \times \hat{\boldsymbol{e}}_{M2})] \tag{6.7}$$

where N_{ch} is the number of propagative channels entering the column, e is the electron charge, U is the potential difference between the contacts, θ is the angle between $\hat{\boldsymbol{e}}_{M1}$ and $\hat{\boldsymbol{e}}_{M2}$, and f_1 (f_2) accounts for the angular dependence of the torque in the thin (thick) layer and is the output of CRMT. This torque is expressed in Joules, while the torque that enters the LLG equation (6.6) for the normalized magnetization is $\boldsymbol{\tau}_j = (g\mu_B)/(\hbar V_j)\boldsymbol{\tau}_j{}^{crmt}$, for $j = 1, 2$. V_j is the volume that has to be associated to each site, that shall be defined below. The CRMT calculation (6.7) has to be repeated for all the columns that constitute the system, in order to obtain the torque for each site of surface 1 and 2.

In general the mesh is not regular, so that there is not an obvious way to divide the system into columns. FIG.(6.15) illustrates the method used for the division of the system. We start considering a site with position $\boldsymbol{r}_1$ on surface 1, and we measure the distances between $\boldsymbol{r}_1$ and all the sites of surface 2. Among these sites we consider the nearest one to $\boldsymbol{r}_1$, for example $\boldsymbol{r}_2$, and we assign $\boldsymbol{r}_1$ and $\boldsymbol{r}_2$ to the same column. We proceed in the same way for all the sites of surface 1, until each pair of sites of surface 1 and 2 have been associated to a column. This procedure is not optimal in terms

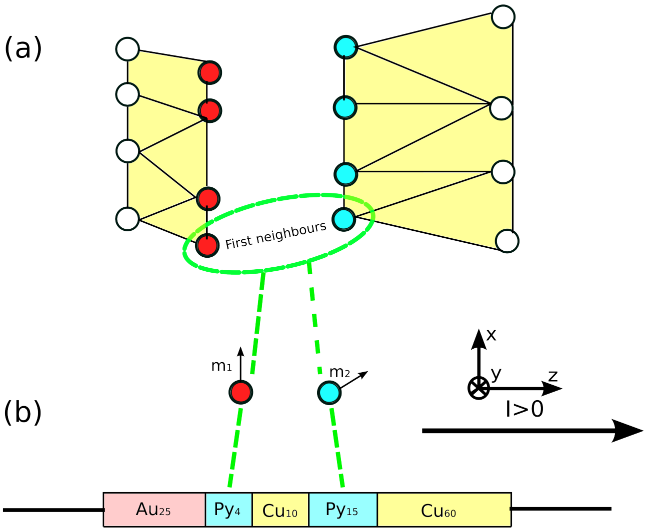

Figure 6.15: A representation of the technique used to compute spin torque for the sites of the surfaces 1 and 2.The system is viewed from profile, with the current flowing along the z axis. The mesh is irregular (the irregularity has been exagerated for better visualization of the technique used to build the CRMT columns). (a) At first one selects a site of surface 1 and looks for its nearest neighbour among the sites of surface 2. (b) to each couple of sites with magnetization $\hat{\boldsymbol{e}}_{M1}$ and $\hat{\boldsymbol{e}}_{M2}$ we associate a CRMT system where $\hat{\boldsymbol{e}}_{M1}$ and $\hat{\boldsymbol{e}}_{M2}$ represent the direction of the magnetizations inside the thin and thick Py layers correspondingly.

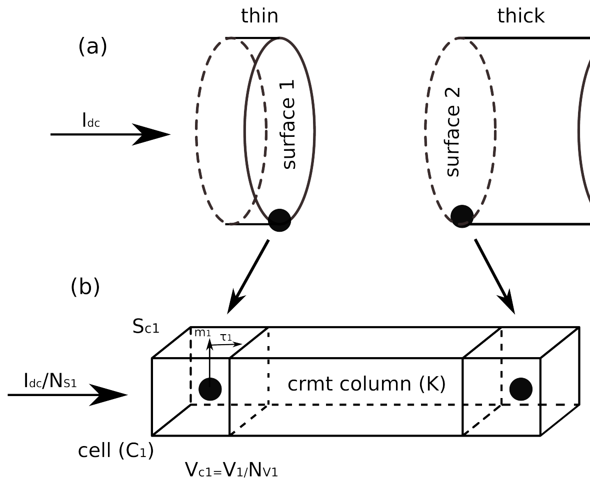

Figure 6.16: (a) For each couple of sites (represented by black dots) of the Nmag mesh lying surface 1 and 2 we define a column K with given cross section, which represents the CRMT system. In each column K there are two cells: C_1 (thin layer) and C_2 (thick layer), that contains respectively one sites of surface 1 and one site of surface 2. The effective spin torque that acts on site 1 with magnetization $\hat{\boldsymbol{e}}_{M1}$ (left) is proportional to the current that crosses C_1 divided by the volume of the cell C_1. We assume that all the columns of surface 1 (and consequently all the cells) have the same cross section, which is simply the surface of the disk divided by the total number of sites N_{S1}. Through the whole system flows a current I_{dc}. Since the columns are connected in parallel, each column (and consequently each cell) of surface 1 layer receives a current $I_{S1} = I_{dc}/N_{S1}$. The same procedure has to be repeated for C_2.

of computation performances but, since it has to be done only once before starting the simulation, it takes a time which is negligible (a few seconds for our mesh) if compared to the time needed to perform the whole simulation.

Starting from Eq.(6.7) , we define now a proper expression for spin torque that depends on the discretization of the system and on the injected current. In our "CRMT picture" the sample is dicretized parallelepiped-shaped columns, each column describing the transport properties of a thin subpart of the system. According to this subdivision, each CRMT column contains two cells corresponding to the two sites atsurfaces $j = 1, 2$, for which spin torque has to be calculated, as shown in FIG.(6.16). Let's focus on the thin layer, which is divided into N_{S1} columns. According to our subdivision, N_{S1} is equal to the number of sites lying at surface 1.

We consider the column K of FIG.(6.16), which contains site 1. The torque $\boldsymbol{\tau}_1$ that acts on $\hat{\boldsymbol{e}}_{M1}$ is the spin current deposited inside the cell

C_1, and is proportional to the current that flows through the C_1 divided its volume V_{C1}. We assume that each cell of the thin layer has the same volume $V_{c1} = V_1/N_{V1}$, where V_1 is the total volume and N_{V1} is the total number of sites contained in the thin layer. in the same way, we assume that each cell of thin layer has the same cross section $S_{C1} = S_1/N_{S1}$, S_1 being the area of surface 1. Starting from Eq.(6.7), we write the torque as

$$\boldsymbol{\tau}_1 = \frac{g\mu_B N_{V1}}{\hbar V_1}\frac{N_{ch}}{4\pi} f_i(\theta) eU \hat{\boldsymbol{w}}_1 \tag{6.8}$$

where for simplicity we have set $\hat{\boldsymbol{w}}_1 = \hat{\boldsymbol{e}}_{M1} \times (\hat{\boldsymbol{e}}_{M1} \times \hat{\boldsymbol{e}}_{M2})$. Since the columns are connected in parallel, the current through each column of the thin layer is given by $I_1 = I_{dc}/N_{S1}$. This current is related to the potential difference between the conductors via the Ohm's law: $eU = R_K I_{dc}/N_{S1}$, where the resistance R_K of the column K depends on the angle θ between $\hat{\boldsymbol{e}}_{M1}$ and $\hat{\boldsymbol{e}}_{M2}$ and on the Sharvin resistance $\mathcal{R}_{sh}$:

$$R_K = \frac{\mathcal{R}_{sh}}{T_K(\theta) S_{c1}}, \tag{6.9}$$

T_K being the transmission probability for an electron to cross column K (see chapters 2 and 3). The torque now reads:

$$\boldsymbol{\tau}_1 = \frac{g\mu_B}{\hbar V_1}\frac{N_{V1}}{N_{S1}}\frac{eN_{ch}}{4\pi}\frac{\mathcal{R}_{\text{sh}}}{S_{C1}} I_{dc}\frac{f_1(\theta)}{T_K(\theta)}\hat{\boldsymbol{w}}_1. \tag{6.10}$$

From the definition of Sharvin resistance, $\mathcal{R}_{\text{sh}} = h/(e^2 N_{ch})$, the previous formula becomes

$$\boldsymbol{\tau}_1 = \frac{g\mu_B}{2eV_1}\frac{N_{V1}}{N_{S1}} I_{dc} F_1(\theta)\hat{\boldsymbol{w}}_1, \tag{6.11}$$

where $F_1(\theta) = f_1(\theta)/T_K(\theta)$ is the angular dependence of spin torque calculated by our CRMT numerical simulations. This formula the same as Eqs.5.12, where spin torque is written as

$$\frac{\gamma I_{dc} M}{2\pi\lambda}\hat{\boldsymbol{w}}, \tag{6.12}$$

whith $\lambda^{-1} = (\eta h)/(2eMV)$ [see Eq.(5.13)], where η is the degree of spin polarization. In our computation $\eta = \frac{N_{V1}}{N_{S1}} F_1(\theta)$ accounts for the geometric characteristic of the layer through N_{V1}/N_{S1}(number of sites at the surface and inside the volume), and for the characteristic of the material and the configuration of the magnetization through $F(\theta)$(CRMT calculation). substituting $\gamma\hbar$ with $g\mu_B$ Eq.(6.12) becomes $(g\mu_B I_{dc}\eta)/(2eV)$, which is the same as Eq.(6.11).

This is the final expression that has to be included in the LLG equation (6.6). The torque is proportional to I_{dc}, as it should be, and the dependence

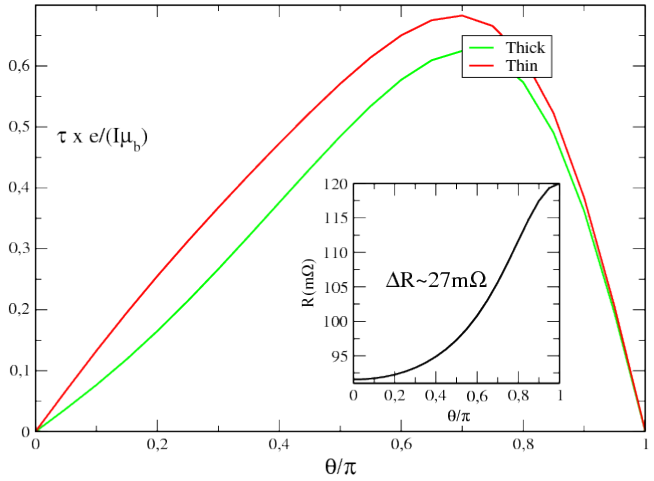

Figure 6.17: Main panel: spin torque for thin and thick layer as a function of the angle between the magnetizationsvof thin and thick layers. *Small panel:* Angular dependence of the conductance.

$4\pi M_1$ (G)	α_1	$4\pi M_2$ (G)	α_2	γ (rad.s¯1.G)
7.8×10^3	1.6×10^{-2}	9.4×10^3	8×10^{-3}	1.87×10^7

Table 6.4: Parameters of thin (1) and thick (2) layer used in micromagnetic simulations with spin torque.

on discretization of the mesh is described by the two factors N_{V1} and N_{S1}, which account respectively for the number of points inside the volume $V_1 = t_1 \pi R^2$ and on the surface 1 with area πR^2, t_1 being the thickness of the thin layer and R being the radius of the pillar. The same procedure has to be done to calculate the torque inside the cell C_2 of each column K in which the pillar is divided. The angular dependence of spin torque and resistance in our system, computed using CRMT, is shown in FIG.(6.17). The torque shown in this figure is perpendicular to the magnetization, and takes into account the triple product of the form $\boldsymbol{e}_M \times \boldsymbol{e}_M \times \boldsymbol{P}$, which depends on the orientation of the magnetization $\hat{\boldsymbol{e}}_M$ and on the polarization $\boldsymbol{P}$ of the current in each layer. The difference of resistance between parallel and antiparallel state, $\Delta R = 27$ mΩ, calculated using CRMT, is close to the experimental value shown in the magnetoresistance hysteresis curve of the nanopillar [see FIG.(6.18)].

The computation performances of Nmag are sensitively slower when the magnetization is far from equilibrium. As a consequence, the discretization length of 3-4 nm used in Sec.(6.3) was too time consuming. In our simulations, we have used a mesh with an average discretization length of 13.8 nm.

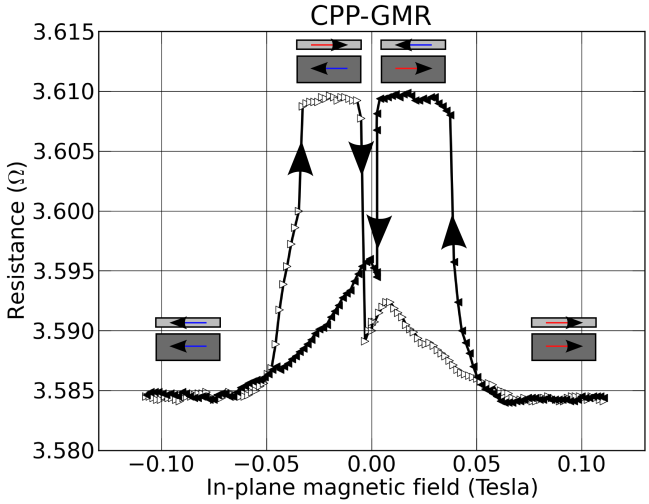

Figure 6.18: Magnetoresistance hysteresis curve of the nanopillar for an in-plane mgnetic field. The dark (respectively light) symbols indicate the magnetic field being ramped up (respectively down).

This value is variable according to the layer, whithin a minimum of 4 nm in the thin layer and a maximum of 15 nm in the thick layer. This corresponds to 651 nodes for the thin layer and 748 nodes for the thick layer. All the simulations have been performed with an external field H_{ext} along $\hat{\boldsymbol{e}}_z$. When the simulations described below were done, in experiments we used a different nanopillar than the one described in Sec.(6.2). The parameters of the older nanopillar, that have been used in our simulations (Tab.3.7), are slightly different. As we shall see, these differences do not affect significantly our results, which are still accurate enough to be comparable with experiments and to describe correct selection rules. In our simulation we haven't taken into account the presence of the magnetic tip of the cantilever, but we have introduced its effect *a posteriori* shifting the spectrum of 5.7 MHz towards high frequency.

In FIG.(6.19) we have compared the spectrum calculated with our coarse mesh with the spectrum calculated with the thinner mesh used in simulations of Sec.(6.3). The spectra have been calculated using the parameters of table (3.7) In both spectra we recognize the modes $a_{\ell,0}$, $a_{\ell,1}$ and $s_{\ell,0}$, for $\ell = 0, 1$. Their frequencies, reported in the table below, are similar, and we can safely describe the system using our coarse mesh.

According to our identifications of the SW modes performed in chapter 5 and at the beginning of this chapter, the modes $s_{0,0}$ and $s_{1,0}$ are the ones withassociated to the dynamics of the thin layer that have lower energy. For this reason they are the modes most easily excited by spin torque in

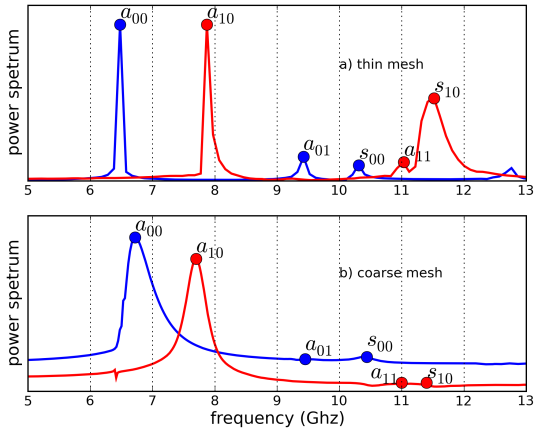

Figure 6.19: Comparison between the two spectra obtained at $I_{\mathrm{dc}} = 0$ with the thin mesh (a) and with the coarse mesh (b) used for simulations of current driven dynamics. The two spectra have been calculated using the parameters of table (3.7), and give close results. This confirms that we can safely use the coarse mesh to describe the system.

Modes	a_{00}	a_{01}	s_{00}	a_{10}	a_{11}	s_{10}
freq. thin mesh (GHz)	6.48	9.43	10.31	7.87	11.03	11.52
freq. coarse mesh (GHz)	6.72	9.45	10.44	7.7	11	11.45

our configuration, where the negative current I_{dc} destabilizes the thin layer and stabilizes the thick one. Spin torque excites all the symmetries in the same way, so that the selection rules for $\ell = 0, 1$ are given only by the initial configuration of the magnetization. Initial conditions where the magnetization is uniformely tilted in a given direction with respect to $\hat{\boldsymbol{e}}_z$ favors $l = 0$ modes, while initial conditions where the magnetization is tilted in orthoradial direction with respect to the equilibrium axis $\hat{\boldsymbol{e}}_z$ favors $\ell = 1$ modes. To excite the modes $\ell = 0$ we have started from a configuration where the magnetization is uniformly tilted along $\hat{\boldsymbol{e}}_x$ with a polar angle of 19.5 degrees, then we have computed the time evolution of the system in presence of oersted field and spin torque. For the excitation of $\ell = 1$ modes we have started from a configuration where the magnetization is uniformely aligned with $\hat{\boldsymbol{e}}_z$, and we have applied the following perturbation field at each node of the mesh:

$$\varepsilon_M(r,z) = \theta \hat{\boldsymbol{e}}_M(\boldsymbol{r},\boldsymbol{z}) \times \hat{\boldsymbol{e}}_r = \theta \hat{\boldsymbol{e}}_z \times \hat{\boldsymbol{e}}_r \tag{6.13}$$

with $\theta = 0.01$, corresponding to a uniform tilt in orthoradial direction. then

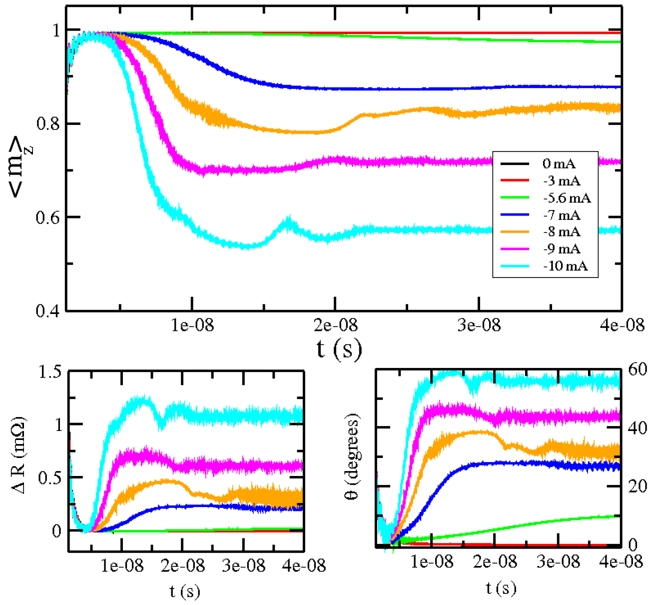

Figure 6.20: (a) time evolution of the longitudinal component of the space averaged magnetization of the thin layer, calculated for different currents, for an external field $H_z = 10KOe$ applied along $\hat{\boldsymbol{e}}_z$; (b) resistance as a function of time calculated for different currents; (c) precession angle as a function of time calculated for different currents. After an intial transient regime, the precession is stable in time.

we have calculated the time evolution of the system in presence spin torque and oersted field. The time step of our simulations is 5 ps. We have recorded the time decay of the magnetization in both layers, averaged in cartesian and cylindrical coordinates in the same way as in Sec.(6.3), to study modes with $\ell = 0$ and 1 correspondingly.

6.4.2 Resistance as a function of current

In this section we shall see how the resistance of the system changes as a function of dc current and applied magnetic field. abrupt changes of the resistance allow to identify the different dynamical regimes of the nano oscillator. In particular, we shall compare calculations of resistance with time resolved dynamics of the magnetization, to see how the precession changes when current increases.

At first, we show the time decay of the normalized magnetization (averaged in cartesian coordinates) $\langle \boldsymbol{m} \rangle_1 = \langle \boldsymbol{M}_1 / M_1 \rangle$ and $\langle \boldsymbol{m}_2 \rangle = \langle \boldsymbol{M}_2 / M_2 \rangle$ inside both layers, at different currents and magnetic fields. At sufficently high current, both $\langle \boldsymbol{m}_1 \rangle$ and $\langle \boldsymbol{m}_2 \rangle$ precess with an angle α_1 and α_2 with respect to the equlibrium axis $\hat{\boldsymbol{e}}_z$. Since we are interested in the variation of resistance ΔR as a function of the angle θ between $\langle \boldsymbol{m}_1 \rangle$ and $\langle \boldsymbol{m}_2 \rangle$, we have set the resistance to zero in the parallel configuration. In FIG.(6.20a) we have plotted the average longitudinal magnetization $\langle m_{z,1} \rangle$ of the thin layer as a function of time for different bias current, while FIG.(6.20b) and c show ΔR and θ as a function of time. The simulation has been performed with an external field $H_z = 10$ KOe under the initial conditions for the excitation of the modes $\ell = 0$, and the decay has been monitored for 40 ns.

In this simulation the distinction between subcritical and supercritical regimes appears clearly: at low bias currents $\langle m_{z,1} \rangle$ is aligned with $\hat{\boldsymbol{e}}_z$, while starting from -5.6 mA the damping is compensated and the system starts autooscillating. This appears as a reduction of the longitudinal magnetization.. FIG.(6.20) allow to estimate the critical current I_{th} around -5.6 mA, where the stable precession becomes visible. In the next section we shall calculate critical current from the analysis of the spectrum, and we shall see that this first extimation is quite precise. Notice that, the higher is the current, the shorter is the time needed for the magnetization to reach steady precession state. With a current -10 mA about 10 ns are needed to open a stable precession angle of 60°. At higher currents, reversal and stable precession can be reached in about 5 ns.

For a precise caracterization of the dynamics, in FIG.(6.21) we report a phase diagram of the resistance as a function of field (between 8 and 13 KOe) and current (between 0 and -29 mA). At high currents (more than -10 mA) the resistance oscillates as a function of time, so that time averaged resistance has to be considered. To obtain this phase diagram, we have monitored the decay for 20 ns, and we have time-averaged the resistance in the window between 15 and 20 ns. The diagram can be divided into 4 regions (delimited by dashed white and black lines) with different dynamics.

Region (1), in dark-blue tone, is the subcritical regime, where the current is not sufficient to compensate damping, and both layers are oriented along $\hat{\boldsymbol{e}}_z$. It corresponds to a region of low resistance. In region (2) (light blue tone), current starts exciting the precession of the thin layer. As a small precession angle opens, the resistance increases slightly. Notice that critical current depends on the applied fields: since it is responsible for the stiffness of the system: as field increases, critical current is higher. Region 3 starts around 10 mA, where the diagram changes abruptly: The magnetization $\boldsymbol{m}_1$ is partially reversed, with a precession angle that approaches 160^{circ} at fields higher than 10.5 KOe. The dipolar interaction due to the reversal of the thin layer, induces a precession of the thick layer. In this regime both layers precess with angles α_1 and α_2 oscillating with time, which cause fluctuations of the resistance. These fluctuations are damped with time, but still visible at 20 ns. Region (4) is similar to region (3), since both layer are precessing. The difference consists in the fact that the oscillations of α_1 and α_2 disappear quickly (about 5 ns).

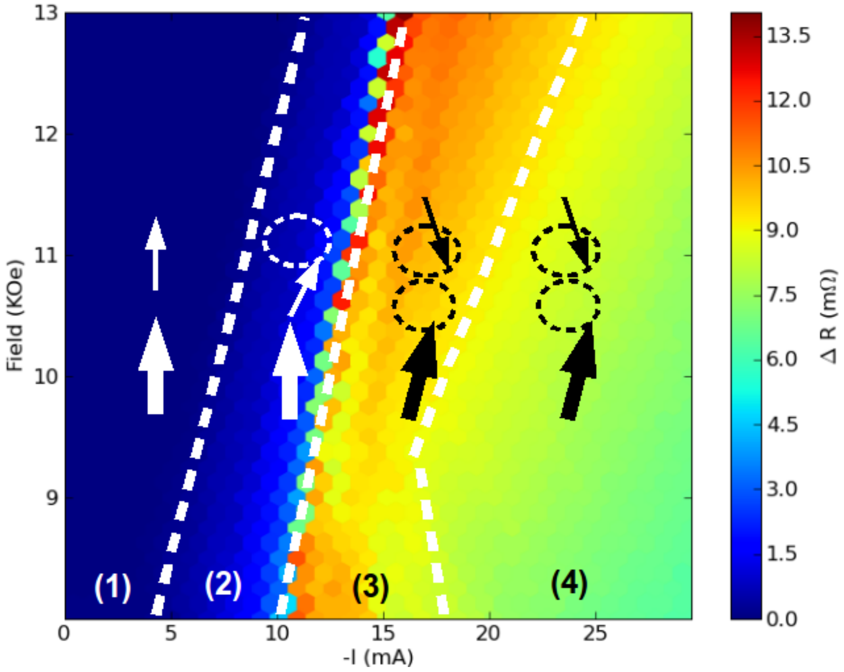

Figure 6.21: Simulated phase diagram of the resistance as a function of current and magnetic field. The diagram is divided in 4 regions with different dynamics. Region (1): both the layers are aligned with $\hat{\boldsymbol{e}}_z$; region (2): precession of the thin layer; regions (3) and (4): magnetization reversal and precession of both layers (see text).

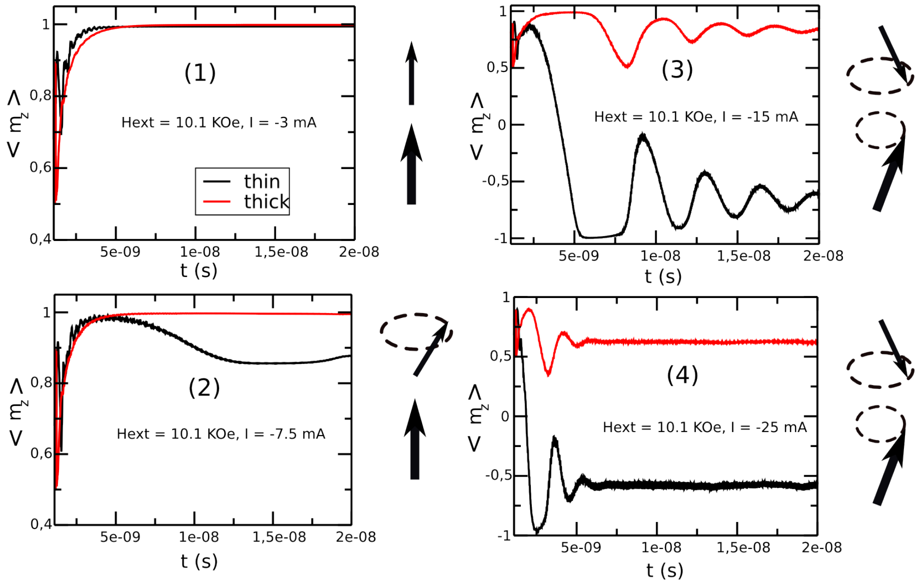

Figure 6.22: longitudinal average magnetization of thin (black) and thick (red) layer as a function of time, calculated in each of the regions of the phase diagram shown in FIG.(6.21).

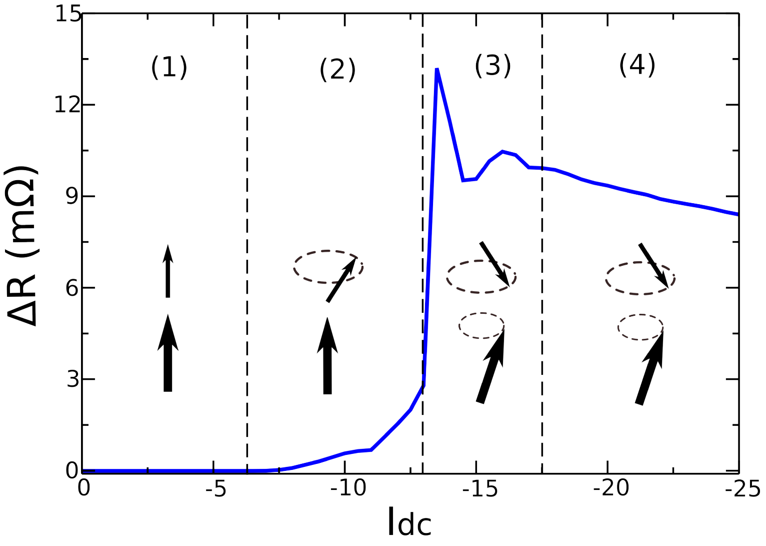

Figure 6.23: Resistance as a function of current calculated for $H_{\mathrm{ext}} = 11$ KOe. Resistance varies sensitively from one region to the other, with the steepest variation in region (3), when reversal occurs.

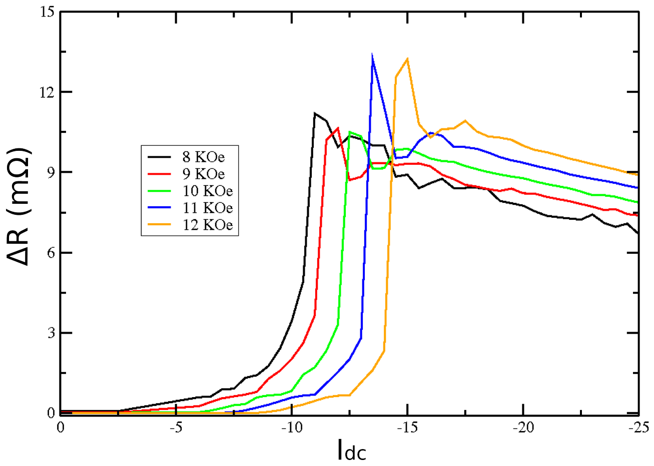

Figure 6.24: Resistance as a function of current calculated for different applied field $\boldsymbol{H}_{\text{ext}}$. The stronger is the external field, the highest is the current needed to destabilize the magnetization. The maximum of the resistance (about half of the GMR) corresponds to a precession angle of about 156° .

The subdivision in regions with different resistances can be easily seen in FIG.(6.23), where we have reported the resistance as a function of current, calculated at $H_{\text{ext}} = 1.1$ KOe. In region (3) one can see large variation of the resistance as a function of current, that are not present in region (4), where resistance decreases uniformly with current. More details of the resistance as a function of current, calculated for different applied fields, are shown in FIG.(6.24). Here the dependence of critical current on field appears clearly.

The dynamics of the different regions is shown in FIG.6.22 where we have reported the time evolution of $\langle m_{z,1} \rangle$ (thin) and $\langle m_{z,2} \rangle$ (thick) respectively in black and red tones. Above critical current [region (2)], $\langle m_{z,1} \rangle$ decreases (precession of the thin layer), while $\langle m_{z,2} \rangle$ equals one (no precession of the thick layer). This is coherent with the chosen direction of the current, which compenates the damping of thin layer and increases the damping of thick layer. At higher current, both layers precess as shown in regions (3) and (4).

The phase diagram FIG.(6.21) has been compared with macrospin computations [FIG.(6.26)] performed by V. Rychkov and experimental datas [FIG. (6.25]. Macrospin offers a qualitative description of the different regions, which is similar to ours. In particular, the frontiers between region (1) and (2) and regions (2) and (3) are situated at similar values of current and field. In both cases, the line between regions (2) and (3), where reversal occurs, starts near −10. This value is lower than the experimental one, where reversal occurs between −15 and −20 mA. The main difference between our simulations and macrospin consists in region (3), which in macrospin appears completely homogeneus. In our simulations we can observe separate peaks

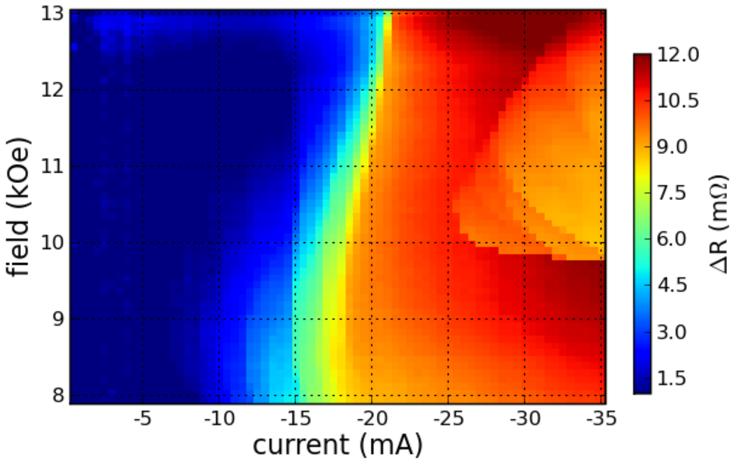

Figure 6.25: Experimental phase diagram that shows resistance as a function of current and applied field.

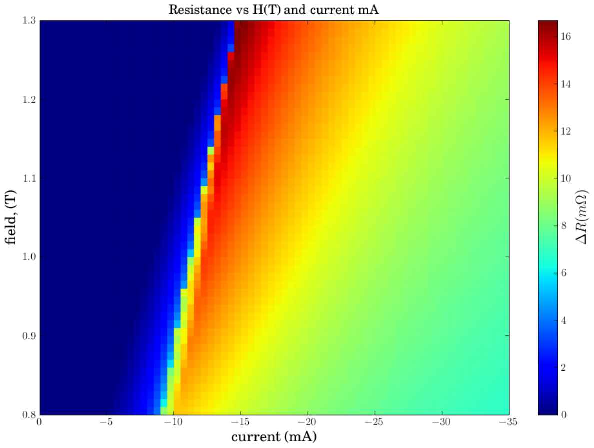

Figure 6.26: Resistance as a function of current and applied field calculated whithin a macrospin approximation coupled to CRMT, for the computation of current driven dynamics.

that are the signature of the presence of different modes. Indeed, the possibility to detect different SW modes is the most important difference between this 3D model and a simple macrospin approximations. Our computations have allowed to describe the different regions of the experimental phase diagram in terms of different dynamics of the magnetization. The agreement between theoretical and experimental phase diagrams is not merely qualitative: in both diagrams the maximum of the resistance is around 12 mΩ, and the resistance of regions (1) and (2) reproduces experimental datas quite correctly. However, there are two major differences: at first, in our simulations the reversal occurs around −10 mA (between regions 2 and 3), while in experiments the reversal occurs starting from about −15 mA. Then, at high current (starting from -20 mS) experimental datas and simulations are quite different. This discrepancy could have different origins, for example the fact that non linear effects (such as the dependence of the damping parameters α_{LLG} on current) play an important role at high current, or that some simplifying assumption that we have made in our model (such as the absence of lateral diffusion of electrons) has to be discarded at high current. In the following, we shall consider only regions 1 and 2, where our simulations can describe the dynamics correctly.

6.4.3 Analysis of the spectrum

In this section we report a comprehensive analysis of the spin wave spectrum, and we describe how it is modified by dc current. Linewidth (full width at half height), frequency and relative height of the resonant peaks as a function of current are the properties that we use to characterize the modes. The simulations have been performed for I_{dc} between 0 and -8 mA, with an applied field of 10 KOe, a range that gives the possibility to observe the behaviour of the system near critical current. This analysis allows for a more comprehensive description of regions 1 and 2 of the phase diagram of FIG.(6.21).

The modes s_{00} and s_{10} are the lowest energy modes correponding to an excitation of the thin layer, and for this reasons are the one most easily excited by spin torque (see chapter 5).these modes have been observed in our experiments (see below). As we shall see, our simulations describe correctly the behaviour of these modes excited by spin torque.

FIG.(6.27) shows the power spectrum (in logarithmic scale) for the $\ell = 0$ modes as a function of current. Two important features are clearly visible. first, the relative height of the peaks changes as a function of current: The first group of peaks on the left, visible until −4 mA, corresponds to the mode a_{00} at 6.72 GHz, which dominates the spectrum at low current. This is the uniform mode which corresponds to a precession mainly concentrated in the thick layer. Starting from −4 mA the mode s_{00} at 10.44 GHz is visible. The spectral weight of this mode grows with current and dominates the spectrum

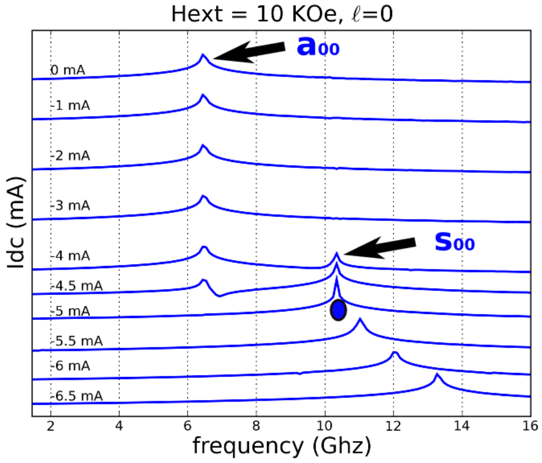

Figure 6.27: Power spectrum (in logarithmic scale) of the modes $\ell = 0$ calculated for different dc currents, whith $H_{\text{ext}} = 10$ KOe. At zero current the mode a_{00} at 6.72 GHz is visible. This mode is associated to the precession of the thick layer. Increasing current (around -4 mA), the mode s_{00} at 10.44 GHz starts growing and eventually dominates the spectrum. This mode is associated to the precession of the thin layer, excited by spin torque. The frequency of $s_{0,0}$ is fixed until the critical threshold and then increases as a function of current. This indicates that critical current for this mode (marked by a blue dot) is between -5 and -5.5 mA.

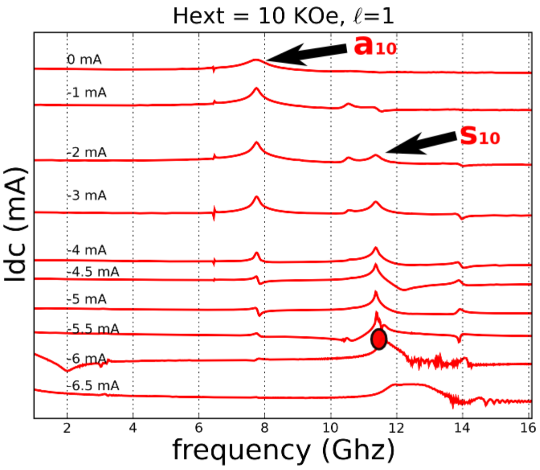

Figure 6.28: Power spectrum (in logarithmic scale) of the modes $\ell = 1$ calculated for different dc currents, whith $H_{\text{ext}} = 10$ KOe. At zero current the mode a_{10} at 7.7GHz is visile. This mode is associated to the precession of the thick layer. Increasing current (around -3 mA), the mode s_{10} at 11.4 GHz starts growing and eventually dominates the spectrum. This mode is associated to the precession of the thin layer, excited by spin torque. The frequency of $s_{1,0}$ is fixed until the critical threshold and then increases as a function of current. This indicates that critical current for this mode (marked by a red dot) is between -5.5 and -6 mA.

starting from −4.5 mA.Physically, this means that at zero current the thick layer carries all the excitation, and when current increases the thin layer is excited and absorbs almost all the energy of spin transfer effect. This behaviour is the signature of the *selection rule* for $\ell = 0$ modes: it shows which mode is much easily excited by spin torque, and relates it to initial conditions of the magnetization. Notice that the peak corresponding to s_{00} grows of about two orders of magnitude around critical current. The frequency of s_{00} is fixed until −5 mA, and then starts growing with current. This gives an indication to find critical current (indicated by a blue dot on the graph), situated between -5 and -5.5 mA,since we expect the frequency to be constant until critical threshold, and then to grow linearly with current [85].

FIG.(6.28) shows the power spectrum (in logarithmic scale) of the thin layer for the $\ell = 1$ modes as a function of current. The group of peaks on the left, visible until −4 mA, corresponds the mode a_{10} at 7,84 GHz, which dominates the spectrum at low current. The presence of this mode indicates that the precession is concentrated mainly in the thick layer. Starting from −3.5 mA the mode s_{10} at 11.4 GHz is visible. The spectral weight of this mode grows with current and dominates the spectrum starting from −4.5 mA. As in the previous case, this indicates that spin torque excites the precession of thin layer. The frequency of s_{10} is fixed until −5.5 mA, and then starts growing with current. This allows to situate critical current (indicated by a red dot on the graph) between -5.5 and -6 mA.

The two spectra displayed in FIGS.(6.27) and (6.28) have been obtained starting from two different initial configuration of the magnetization, described in section (6.4.1). This is useful to describe the two spectra separately, but it does not give any information about the possible cohexistence and competition of modes with different ℓ symmetry. To gain further insight on the properties of the spectrum, in FIG.(6.29) we haved compared $\ell = 0$ and 1 modes. The two different spectra have been obtained starting *exactly from the same initial condition*: at the beginning the magnetization is aligned along $\boldsymbol{e}_z$, and then it is tilted uniformly in the orthoradial direction. Starting from this initial condition, we have recorded the time decay of the magnetization for 40 ns. If one averages the magnetization in cartesian coordinates, then the Fourier transform shows the $\ell = 0$ spectrum, while if one averages the magnetization in cylindrical coordinates, the Fourier transform shows the $\ell = 1$ spectrum. Thus the two panels (a) and (b) of FIG.(6.29) show *exactly the same system* where the spatial average of the magnetization has been calculated in a different way. Changing the way of averaging the magnetization allows to reveal a different spectrum. This shows that the two modes s_{00} and s_{10} cohexist. This competition between modes has been observed experimentally: FIG.(6.30) shows the power spectrum as a function of current and applied field. This measure has been performed at fixed frequency, measuring the resistance fluctuations with a spectrum analyzer.

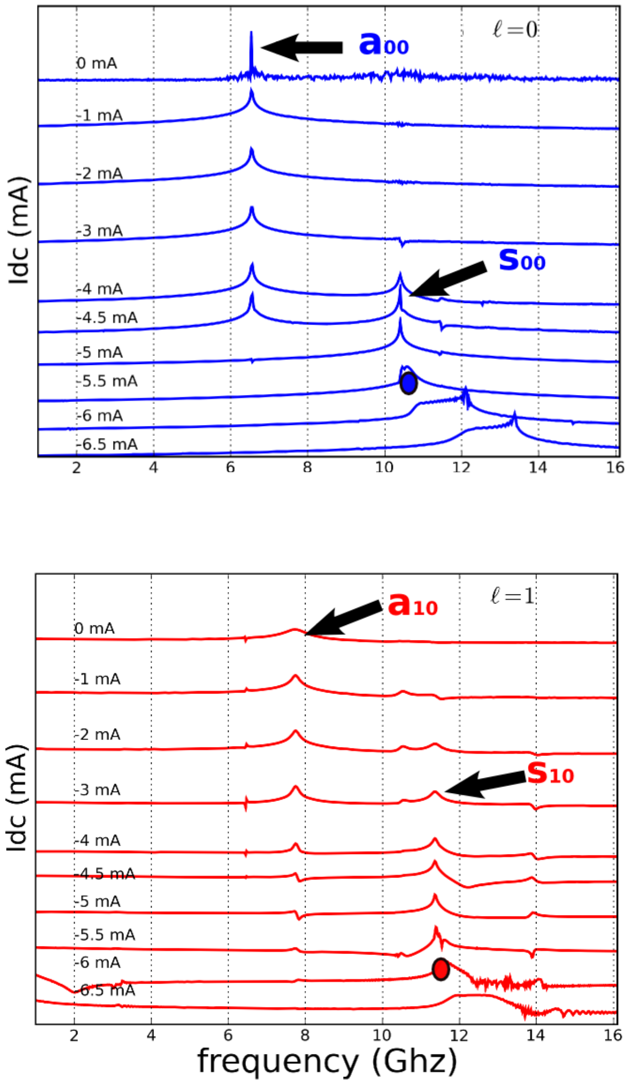

Figure 6.29: Simulation of the competition between $\ell = 0$ (blue tones) and $\ell = 1$ (red tones) modes, computed for different currents. The plot are in logarithmic scale. Changing the way of computing the spatial average of the magnetization allows to see modes with $\ell = 0$ (averaging in cartesian coordinates) and modes with $\ell = 1$ (averaging in cylindrical coordinates).

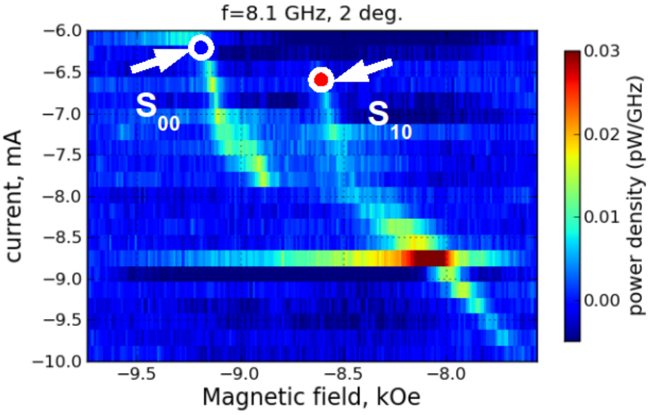

Figure 6.30: Experimental diagram that shows the power spectrum as a function of current and applied field. A dc current is injected to excite the thin layer trhough spin torque. The two modes s_{00} and s_{10} coexist and have different critical current (critical threshold, where the two modes are visible, is indicated by a blue and red dot for $\ell = 0$ and 1 correspondingly).

To make the resistance fluctuations visible, the applied field has a polar angle of 2° with respect to $\hat{\boldsymbol{e}}_z$. the resistance of the system) varies in time with a frequency that changes for different SW modes. In this way one can identify the spectrum from a transport experiment (MRFM has not been used here). This experiment is not *exactly* comparable to our simulations, since the physical conditions are not the same: the experiment is performed in field domain, with a polar angle that shifts the overall spectrum toward *low* fields (*i.e.* *high* frequencies), while our simulations are performed in frequency domains with the field applied along $\boldsymbol{e}_z$. However, our simulations predict the cohexistence of s_{00} and s_{10}, their different critical current, and their frequency shift above the critical threshold, in agreement with experimental observations.

To determine critical current, we have calculated the linewidth (full width at half height) $\Delta f_\ell = 2\alpha\omega_{0,\ell}$ of the resonant peaks of the two modes $s_{\ell 0}$ ($\ell = 0, 1$) as a function of current. The linewidth of mode $s_{\ell 0}$ is related to current I_{dc} by the linear relation

$$\Delta\omega_\ell(I_{dc}) = \alpha\left(1 - \frac{I_{dc}}{I_{th,\ell}}\right)\omega_\ell, \tag{6.14}$$

and vanishes at critical current, when the damping is compensated. The computation of critical current has been done as follows: we have computed the power spectrum of the thin layer for different values of I_{dc}. At each value of current, we have fitted the peak of both modes with a Lorenzian, obtaining linewidth and frequency of the modes as a function of current.

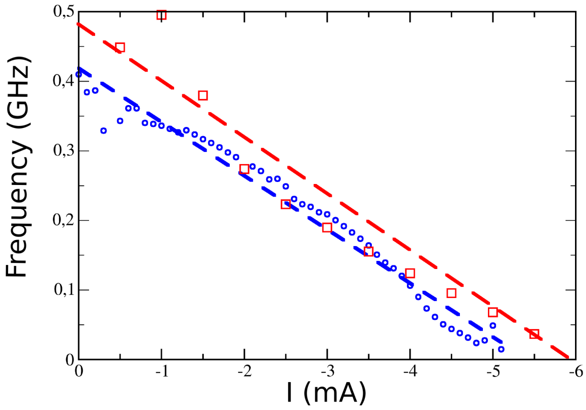

Figure 6.31: Linewidth of the resonant peak of the modes $s_{0,0}$ (blue circles) and s_{10} (red squares) as a function of current, computed with an applied field of 10 KOe. The datas fit the straight lines $\Delta f_0 = -0.08(I - 5.4)$ (blue dashed line) and $\Delta f_1 = -0.08(I - 5.9)$(red dashed line) respectively, from which one finds a critical current of -5.4 and -5.9 mA correspondingly.

FIG. (6.31) shows the linear dependence of the linewidth of both modes on I_{dc}. The linewidth decreases linearly with current for both modes, and fits the straight lines $\Delta f_0 = -0.08(I - 5.4)$ for mode s_{00}, and $\Delta f_1 = -0.08(I - 5.9)$ for mode s_{10}. From these fits one obtains the two critical currents $I_{th,0} = -5.43$ mA and $I_{th,1} = -5.92$ mA. We Notice that in our numerical simulations, the linewidth cannot go to zero *exactly* at critical current. Moreover, near critical threshold the shape of the peaks is slightly distorted, and the exact computation of the linewidth fitting the peak with a Lorentzian is not possible. However, the result of this fit is coherent with the estimation of critical current done observing the spectra FIGS.(6.27) and (6.28). This prediction is comparable with experimental results shown in FIG.(6.30): the modes s_{00} and s_{10} are visible starting from critical current (around -6.2 and -6.6 mA correspondingly. We stress that *exact* comparison between simulations and experiments are not possible in this case, Since we do not simulate the same experimental conditions, we do not expect a perfect agreement with experiments.

We conclude this section with the computation of the nonlinear frequency shift for s_{00} and s_{10}. FIG.(6.32) shows the frequency as a function of current for both modes. As expected, the frequency is constant until the critical threshold. In the supercritical regime, the frequency grows with a slope of 1.89 GHz/mA and 2.55 GHz/mA for modes s_{00} and s_{10} correspondingly. We have compared the prediction for s_{00} with experimental results: FIG.(6.33)

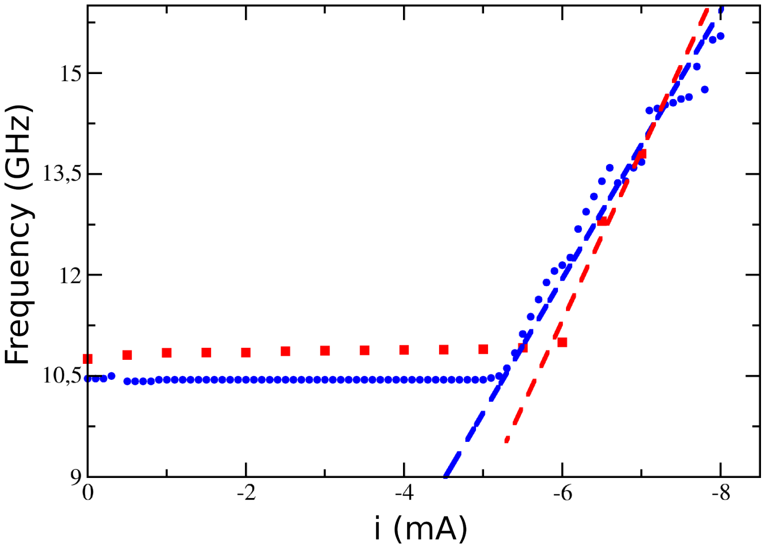

Figure 6.32: Frequency of the modes s_{00} (blue circles) and s_{10} (red squares) as a function of current, computed with an external field of 10 KOe. The frequency is constant in the subcritical regime, and then grows linearly as a function of current, with a slope of 1.89 GHz/mA for s_{00} (blue dashed line) and 2.55 GHz/mA for s_{10}.

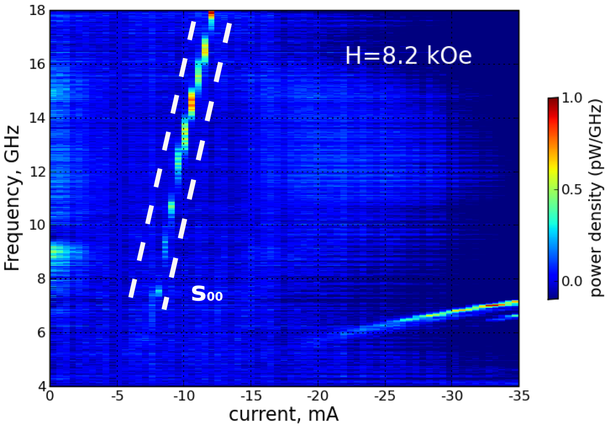

Figure 6.33: Power density as a function of frequency and current, calculated for an external magnetic field $H_{\text{ext}} = 8.2$ KOe. The frequency of the mode s_{00} (visible in the middle of the two white dashed lines) grows linearly as a function of current, with a slope of about $2GHz/mA$.

is a colorplot of the power spectrum as a function of frequency and current. Mode s_{00} (in evidence on the figure) grows with a slope of $2GHz/mA$, in good agreement with our predictions. The simulations and experiments are not performd under the same conditions (the applied field is 8.2 KOe in this experiment), but our prediction reproduces experimental observations quite well.

6.5 Conclusions

In this last section we have summarized the main results of this work. At first, we focus on some conclusive remarks on this chapter, then we shall perform a more general comment on our model of spin transport and its possible applications and improvement

The experimental results shown in this chapter have important consequences regarding the optimization of the performance of STNOs, which are rarely mentioned.

First, an accurate identification of the SW modes according to their symmetry is required to understand the details of the high frequency, but also of the static properties in magnetic nanostructures. For instance, SW modes having different symmetries might influence differently the high frequency noise of a spin-valve device. We also point out possible confusions between the $\ell = 0$ and the $\ell = +1$ SW eigen-modes, whose two spectra are in almost translational correspondence. In particular cases where the magnetization value is inferred from the SW spectrum, mislabeling the lowest energy mode of the $\ell = +1$ SW spectrum as the uniform mode ($\ell = 0$) will lead to a fitted value of the magnetization through the Kittel formula that underestimates the true value by about a kiloGauss. Small misalignment with the perpendicular direction can further enhance the discrepancy.

Second, the collective character of the SW modes can directly influence the spin transfer torque, for which the relative angle between the magnetizations in the two layers matters. One might expect, that the spin transfer efficiency does not only depend on which layer (thick or thin) is dominating the mode, but also on the coupling (anti-symmetrical or symmetrical) between both layers. To maximize spin-transfer effects in the normal configuration, one would like to have ideally the dynamics of the thin layer being coupled anti-symmetrically to the dynamics of the thick layer. Since the anti-symmetric motion is the binding state, this implies that the optimum is obtained when the uniform mode of the thin layer is lower in energy than the uniform mode of the thick layer. If the magnetization is the adjustable parameter, that implies choosing a stack composition where the magnetization of the thin layer exceeds the one of the thick layer.

Third, the above study provides us an unambiguous method to identify the nature of the normal mode that auto-oscillates when the current exceeds the critical threshold. The result of this study will be published elsewhere in an upcoming paper. The precise determination of the SW mode symmetry of the auto-oscillating mode is important for the phase synchronization of a STNO to an external source. In fact, it will be successful only if the latter can couple efficiently to the spin transfer driven auto-oscillation modes, *i.e.*, if it has the appropriate symmetry. Since excitation by the uniform magnetic field produced by an external antenna or by the current across the nanopillar have been demonstrated to be mutually exclusive, depending on the nature of the auto-oscillating mode only one of the two external excitation circuit will provide an efficient mean to synchronize oscillators together.

Finally, the MRFM technique has allowed us to study spin-transfer effects in the normal configuration where ST-FMR effects are hidden due to symmetry reasons. There are strategic reasons to understand in details the dynamics in the perpendicular configuration for STNO applications. Indeed, the excited modes have there the maximum non-linear frequency shift coefficient [86]. This confers to this geometry the widest agility to potentially phase-lock to an external source and therefore it corresponds to one of the optimal candidate to achieve mutual phase synchronization in large arrays of STNOs. Phase synchronization has been identified as a possible mean to dramatically increase the generated microwave power of these nano-oscillators and, at the same time, reduce their linewidth [50, 64, 87, 42, 39, 78, 35, 90, 96]. Also, the perpendicular geometry corresponds to an optimal orientation for the spin polarized current to compensate the damping, leading to a minimal current threshold to produce auto-oscillations [88, 56].

In summary, we have reviewed the importance to classify the SW eigenmodes inside a nano-pillar by their symmetries, in particular regarding their potential applications in magneto-electronics.

Let us now focus on our approaches to quantum transport, developed in chapters 3 and 4. CRMT and TB model are two complementary approaches than can be used together to describe complicated systems where one requires both high computational performances and a fully quantum approach for certain regions (such as tunnel junctions). The good agreement between CRMT and TB for Ohmic conductors allows to parametrize TB for a large variety of materials. The multiscale approach, together with this possibility to describe many different materials, are the aspects that make our model flexible and general.

On the conceptual point of view, CRMT and TB model represent two completely different approaches that relate scattering formalism, Random Matrix Theory, Circuit Theory and Valet-Fert model. This sense our models make a bridge between fully quantum and semiclassical approaches, introducing the concepts of spin accumulation and chemical potential into scattering formalism. Two important relations are at the basis of our "multiscale description" of quantum transport. First, the addition rule for scattering and hat matrices [see sections (2.3.3) and (2.4.1)], which allows to decompose and recompose the system when needed, and second the Fisher-Lee formula [section (4.3)], that relates Green's function to scattering (and hat) matrices. The addition law, which describes transport as a sequence of multiple transmission and reflections amplitudes (or probabilities, if one refers to hat matrices) is the cornerstone of CRMT. In particular, CRMT generalizes Valet-Fert approaches essentially because the Sharvin resistance is included through the addition law, and the matrix structure allows to describe non collinear systems through a rotation in spin space.

The main novelty of this work is the fact that CRMT has been coupled to a micromagnetic code to treat *on an equal footing* the complexity of both electronic transport and magnetization dynamics. This has allowed to describe correctly the spin wave spectrum of spin torque nano oscillator. The fact that we have used CRMT instead of TB for our simulations is essentially due to the different computational peroformances and to the large mesoscopic fluctuations of TB calculations: describing our spin valve with TB model would have been too time consuming and useless, since our system is Ohmic. Coupling CRMT with Nmag has allowed to describe the interplay between electronic transport and magnetization dynamics *locally*, and to take into account the 3D texture of the magnetization and of transport properties. The fact that CRMT has no free parameters has allowed to calculate *exactly* the torque acting on both layers. The identification of the correct selection rules, in agreement with the analytical model of chapter 5 and with experiments, is the main result of this work: it allows to determine critical current, non linear frequency shift and to describe the coexistence (observed experimentally) and the competition of modes with different ℓ symmetry. At the same time, it constitutes a good test of CRMT and of the algorithm used to couple CRMT to Nmag. Notice that a simple macrospin model cannot describe SW modes (apart from an approximation of the uniform mode), and it is not suitable for a realistic description of a STNO. This is the main avantage of a 3D computation.

Several developments and applications of our model are possible. At first, it would be interesting to repeat our simulations with a thinner mesh, to see if some important quantities (like resistance) depend on the mesh. To do this, an optimization of the code that couples CRMT to Nmag should be implemented to obtain better computational performances. It would be interesting to apply our model to the computation of tunnel magnetoresistance. The description of such systems requires the coupling between a *real multiscale model* and a micromagnetic software, since TB model is needed to describe tunneling inside the insulator, while CRMT can be used for metal components.

Concerning possible improvements of our model, we have seen that our description is doubtful at high current [compare our simulations with the experimental phase diagram: FIGS.(6.21) and (6.25)]. A possible explanation is that we have taken the LLG damping coefficient constant, while in reality it depends on current [85]. Another important aspect is that in our simulations we have neglected the lateral diffusion of spins, since the system is described using one dimensional "CRMT columns", where electrons propagate only along the z direction. A further, natural step, is to use a fully three dimensional CRMT model of transport. This model, which was not ready when have performed these simulations, has now been implemented by the group of X. Waintal. Our CRMT-1D model is effective to describe selection rules into a perpendicularly magnetized nanopillar with magnetic field applied along $\boldsymbol{e}_z$, but more complicate configurations (such as magnetic vortexes) may require a CRMT-3D description.

To conclude, the approach taken in this work, is effective in the description of our realistic system, and takes into account the complexity of transport and magnetization dynamics. The agreement as well as the discrepancies that we have found between experiments and simulations are an excellent guide to understand the LLG equation, as well as the validity of our model and of the approximations that we have made. This work can be considered as an intermediate step towards a more complete, fully 3D description of transport and magnetization dynamics in realistic systems.

Bibliography

[1] K. A. Muttalib J. L Pichard A. D. P. Stone, P. A. Mello. In P. A. Lee B. L. Alstshuler and R. A. Webb, editors, *Mesoscopic Phenomena in Solids*, volume 83 of *Topics in Applied Physics*, page 369. North-Holland, Amsterdam, 1991.

[2] E. Akkermans and G. Montambaux. *Mesoscopic physics of electrons and photons.* Cambridge University Press, 2007.

[3] F. J. Albert, J. A. Katine, R. A. Buhrman, and D. C. Ralph. Spin-polarized current switching of a Co thin film nanomagnet. *Appl. Phys. Lett.*, 77(23):3809–3811, 2000.

[4] P. W. Anderson and H. Suhl. Instability in the motion of ferromagnets at high microwave power levels. *Phys. Rev.*, 100:1788, 1955.

[5] Various Authors. *Magnétisme.* EDP Sciences, 1999.

[6] M. N. Baibich, J. M. Broto, A. Fert, F. Nguyen Van Dau, F. Petroff, P. Etienne, G. Creuzet, A. Friederich, and J. Chazelas. Giant magnetoresistance of (001)fe/(001)cr magnetic superlattices. *Phys. Rev. Lett.*, 61(21):2472–2475, Nov 1988.

[7] Gerrit E. W. Bauer, Yaroslav Tserkovnyak, Daniel Huertas-Hernando, and Arne Brataas. Universal angular magnetoresistance and spin torque in ferromagnetic/normal metal hybrids. *Phys. Rev. B*, 67(9):094421, Mar 2003.

[8] C. W. J. Beenakker. Random-matrix theory of quantum transport. *Rev. Mod. Phys.*, 69(3):731–808, Jul 1997.

[9] L. Berger. Emission of spin waves by a magnetic multilayer traversed by a current. *Phys. Rev. B*, 54(13):9353–9358, Oct 1996.

[10] D.V. Berkov and J. Miltat. Spin-torque driven magnetization dynamics: Micromagnetic modeling. *Journal of Magnetism and Magnetic Materials*, 320(7):1238 – 1259, 2008.

[11] G. Binasch, P. Grunberg, F. Saurenbach, and W. Zinn. Enhanced magnetoresistance in layered magnetic structures with antiferromagnetic interlayer exchange. *Phys. Rev. B*, 39(7):4828–4830, 1989.

[12] O. Bohigas, M. J. Giannoni, and C. Schmit. Characterization of chaotic quantum spectra and universality of level fluctuation laws. *Phys. Rev. Lett.*, 52(1):1–4, Jan 1984.

[13] F. Boust and N. Vukadinovic. Micromagnetic simulations of vortex-state excitations in soft magnetic nanostructures. *Phys. Rev. B*, 70:172408, 2004.

[14] Arne Brataas, Gerrit E.W. Bauer, and Paul J. Kelly. Non-collinear magnetoelectronics. *Physics Reports*, 427(4):157 – 255, 2006.

[15] Arne Brataas, Yu. V. Nazarov, and Gerrit E. W. Bauer. Finite-element theory of transport in ferromagnet–normal metal systems. *Phys. Rev. Lett.*, 84(11):2481–2484, Mar 2000.

[16] Matthias Braun, Jürgen König, and Jan Martinek. Theory of transport through quantum-dot spin valves in the weak-coupling regime. *Phys. Rev. B*, 70(19):195345, Nov 2004.

[17] P. W. Brouwer and C. W. J. Beenakker. Effect of a voltage probe on the phase-coherent conductance of a ballistic chaotic cavity. *Phys. Rev. B*, 51(12):7739–7743, Mar 1995.

[18] P. W. Brouwer and C. W. J. Beenakker. Voltage-probe and imaginary-potential models for dephasing in a chaotic quantum dot. *Phys. Rev. B*, 55(7):4695–4702, Feb 1997.

[19] M. Büttiker, Y. Imry, R. Landauer, and S. Pinhas. Generalized many-channel conductance formula with application to small rings. *Phys. Rev. B*, 31(10):6207–6215, May 1985.

[20] I. A. Campbell and A. Fert. In E. P. Wolfarth, editor, *Ferromagnetic materials*, volume 3 of *Lecture Notes in Physics*, page 747. 1982.

[21] C Caroli, R Combescot, P Nozieres, and D Saint-James. Direct calculation of the tunneling current. *Journal of Physics C: Solid State Physics*, 4(8):916, 1971.

[22] V. Charbois, V. V. Naletov, J. Ben Youssef, and O. Klein. Influence of the magnetic tip in ferromagnetic resonance force microscopy. *Appl. Phys. Lett.*, 80:4795, 2002.

[23] V. Charbois, V. V. Naletov, J. Ben Youssef, and O. Klein. Mechanical detection of ferromagnetic resonance spectrum in a normally magnetized Yttrium-Iron-Garnet disk. *J. Appl. Phys.*, 91:7337, 2002.

[24] W. Chen, J.-M. L. Beaujour, G. de Loubens, A. D. Kent, and J. Z. Sun. Spin-torque driven ferromagnetic resonance of co/ni synthetic layers in spin valves. *Appl. Phys. Lett.*, 92(1):012507, 2008.

[25] W. Chen, G. de Loubens, J.-M. L. Beaujour, J. Z. Sun, and A. D. Kent. Spin-torque driven ferromagnetic resonance in a nonlinear regime. *Appl. Phys. Lett.*, 95(17):172513, 2009.

[26] S. Datta. *Electronic Transport in Mesoscopic Systems.* Cambridge University Press, 1995.

[27] Supriyo Datta. Nanoscale device modeling: the green's function method. *Superlattices and Microstructures*, 28(4):253 – 278, 2000.

[28] G. de Loubens. *Spectroscopie micro-onde d'une nanostructure métallique magnétique hybride.* PhD thesis, Université Paris Sud - Paris XI, 2005.

[29] G. de Loubens, V. V. Naletov, and O. Klein. Reduction of the spin-wave damping induced by nonlinear effects. *Phys. Rev. B*, 71(18):180411(R), 2005.

[30] G. de Loubens, V. V. Naletov, O. Klein, J. Ben Youssef, F. Boust, and N. Vukadinovic. Magnetic resonance Studies of the Fundamental Spin-Wave Modes in Individual Submicron Cu/NiFe/Cu Perpendicularly Magnetized Disks. *Phys. Rev. Lett.*, 98(12):127601, 2007.

[31] G. de Loubens, V. V. Naletov, M. Viret, O. Klein, H. Hurdequint, J. Ben Youssef, F. Boust, and N. Vukadinovic. Magnetic resonance spectroscopy of perpendicularly magnetized permalloy multilayer disks. volume 101, page 09F514. AIP, 2007.

[32] G. de Loubens, A. Riegler, B. Pigeau, F. Lochner, F. Boust, K. Y. Guslienko, H. Hurdequint, L. W. Molenkamp, G. Schmidt, A. N. Slavin, V. S. Tiberkevich, N. Vukadinovic, and O. Klein. Bistability of vortex core dynamics in a single perpendicularly magnetized nanodisk. *Phys. Rev. Lett.*, 102(17):177602, 2009.

[33] B. Dieny, V.S. Speriosu, B.A. Gurney, S.S.P. Parkin, D.R. Wilhoit, K.P. Roche, S. Metin, D.T. Peterson, and S. Nadimi. Spin-valve effect in soft ferromagnetic sandwiches. *J. Magn. Magn. Mater.*, 93:101, 1991.

[34] R. A. Duine, A. S. Núñez, Jairo Sinova, and A. H. MacDonald. Functional keldysh theory of spin torques. *Phys. Rev. B*, 75(21):214420, Jun 2007.

[35] A. Dussaux, A. V. Khvalkovskiy, J. Grollier, V. Cros, A. Fukushima, M. Konoto, H. Kubota, K. Yakushiji, S. Yuasa, K. Ando, and A. Fert. Phase locking of vortex based spin transfer oscillators to a microwave current. *arXiv:1009.4076v1*, 2010.

[36] A. Fert, V. Cros, J. M. George, J. Grollier, H. JaffrÃ¨s, A. Hamzic, A. VaurÃ¨s, G. Faini, J. Ben Youssef, and H. Le Gall. Magnetization reversal by injection and transfer of spin: experiments and theory. *Journal of Magnetism and Magnetic Materials*, 272-276(Part 3):1706 – 1711, 2004. Proceedings of the International Conference on Magnetism (ICM 2003).

[37] Thomas Fischbacher, Matteo Franchin, Giuliano Bordignon, and Hans Fangohr. A systematic approach to multiphysics extensions of finite-element-based micromagnetic simulations: Nmag. *IEEE Trans. Magn.*, 43(6):2896–2898, 2007.

[38] Daniel S. Fisher and Patrick A. Lee. Relation between conductivity and transmission matrix. *Phys. Rev. B*, 23(12):6851–6854, Jun 1981.

[39] B. Georges, J. Grollier, M. Darques, V. Cros, C. Deranlot, B. Marcilhac, G. Faini, and A. Fert. Coupling efficiency for phase locking of a spin transfer nano-oscillator to a microwave current. *Phys. Rev. Lett.*, 101(1):017201, 2008.

[40] T.L. Gilbert. A phenomenological theory of damping in ferromagnetic materials. *Magnetics, IEEE Transactions on*, 40(6):3443 – 3449, 2004.

[41] M. Gmitra and J. Barnaś. Current-driven destabilization of both collinear configurations in asymmetric spin valves. *Phys. Rev. Lett.*, 96(20):207205, May 2006.

[42] J. Grollier, V. Cros, and A. Fert. Synchronization of spin-transfer oscillators driven by stimulated microwave currents. *Phys. Rev. B*, 73(6):060409, 2006.

[43] J. Grollier, V. Cros, A. Hamzic, J. M. George, H. Jaffres, A. Fert, G. Faini, J. Ben Youssef, and H. Legall. Spin-polarized current induced switching in Co/Cu/Co pillars. *Appl. Phys. Lett.*, 78(23):3663–3665, 2001.

[44] Bruce A. Gurney, Virgil S. Speriosu, Jean-Pierre Nozieres, Harry Lefakis, Dennis R. Wilhoit, and Omar U. Need. Direct measurement of spin-dependent conduction-electron mean free paths in ferromagnetic metals. *Phys. Rev. Lett.*, 71(24):4023–4026, Dec 1993.

[45] K. Y. Guslienko, S. O. Demokritov, B. Hillebrands, and A. N. Slavin. Effective dipolar boundary conditions for dynamic magnetization in thin magnetic stripes. *Phys. Rev. B*, 66:132402, 2002.

[46] Bret Heinrich, Yaroslav Tserkovnyak, Georg Woltersdorf, Arne Brataas, Radovan Urban, and Gerrit E. W. Bauer. Dynamic exchange coupling in magnetic bilayers. *Phys. Rev. Lett.*, 90(18):187601, May 2003.

[47] Igor Žutić, Jaroslav Fabian, and S. Das Sarma. Spintronics: Fundamentals and applications. *Rev. Mod. Phys.*, 76(2):323–410, Apr 2004.

[48] Albrecht Jander, John Moreland, and Pavel Kabos. Micromechanical detectors for local field measurements based on ferromagnetic resonance (invited). *J. Appl. Phys.*, 89(11):7086–7090, 2001.

[49] O. Redon J. P. Nozieres B. Dieny K. J. Lee, A. Deac. Excitations of incoherent spin-waves due to spin-transfer torque. *Nat. Mater.*, 3(12):877–881, 2004.

[50] Shehzaad Kaka, Matthew R. Pufall, William H. Rippard, Thomas J. Silva, Stephen E. Russek, and Jordan A. Katine. Mutual phase-locking of microwave spin torque nano-oscillators. *Nature*, 437:389–392, 2005.

[51] G. N. Kakazei, P. E. Wigen, K. Yu. Guslienko, V. Novosad, A. N. Slavin, V. O. Golub, N. A. Lesnik, and Y. Otani. Spin-wave spectra of perpendicularly magnetized circular submicron dot arrays. *Appl. Phys. Lett.*, 85(3):443–445, 2004.

[52] Tadao Kasuya. A theory of metallic ferro- and antiferromagnetism on zener's model. *Progress of Theoretical Physics*, 16(1):45–57, 1956.

[53] K. Kazymyrenko and X. Waintal. Knitting algorithm for calculating green functions in quantum systems. *Phys. Rev. B*, 77(11):115119, Mar 2008.

[54] L. Keldysh. *Zh. Eksp. Teor. Fiz.*, (47):1515, 1964.

[55] G. Kießlich, P. Samuelsson, A. Wacker, and E. Schöll. Counting statistics and decoherence in coupled quantum dots. *Phys. Rev. B*, 73(3):033312, Jan 2006.

[56] S. I. Kiselev, J. C. Sankey, I. N. Krivorotov, N. C. Emley, M. Rinkoski, C. Perez, R. A. Buhrman, and D. C. Ralph. Current-Induced Nanomagnet Dynamics for Magnetic Fields Perpendicular to the Sample Plane. *Phys. Rev. Lett.*, 93(3):036601, 2004.

[57] S. I. Kiselev, J. C. Sankey, I. N. Krivorotov, N. C. Emley, R. J. Schoelkopf, R. A. Buhrman, and D. C. Ralph. Microwave oscillations of a nanomagnet driven by a spin-polarized current. *Nature*, 425(6956):380–383, 2003.

[58] O. Klein, V. Charbois, V. V. Naletov, and C. Fermon. Measurement of the ferromagnetic relaxation in a micron-size sample. *Phys. Rev. B*, 67:220407(R), 2003.

[59] O. Klein, V. Charbois, V. V. Naletov, and C. Fermon. Direct measurement of the spin-lattice relaxation in a ferromagnet. *J. Magn. Magn. Mater.*, 272(Suppl. 1):E1027–E1028, 2004.

[60] O. Klein, G. de Loubens, V. V. Naletov, F. Boust, T. Guillet, H. Hurdequint, A. Leksikov, A. N. Slavin, V. S. Tiberkevich, and N. Vukadinovic. Ferromagnetic resonance force spectroscopy of individual submicron-size samples. *Phys. Rev. B*, 78(14):144410, 2008.

[61] S. Labbé and P. Y. Bertin. Microwave polarizability of ferrite particles with non-uniform magnetization. *J. Magn. Magn. Mater.*, 206:93–105, 1999.

[62] L. D. Landau and E. M. Lifshitz. To the theory of the dispersion of the ferromagnetic-body permeability. In *Collected paper*. Ed. Pergamon, 1965.

[63] I. Lee, Y. Obukhov, G. Xiang, A. Hauser, F.Y. Yang, P. Banerjee, D.V. Pelekhov, and P.C. Hammel. Nanoscale scanning probe ferromagnetic resonance imaging using localized modes. *Nature*, 466:845–848, 2010.

[64] F. B. Mancoff, N. D. Rizzo, B. N. Engel, and S. Tehrani. Phase-locking in double-point-contact spin-transfer devices. *Nature*, 437:393, 2005.

[65] Jan Manschot, Arne Brataas, and Gerrit E. W. Bauer. Nonmonotonic angular magnetoresistance in asymmetric spin valves. *Phys. Rev. B*, 69(9):092407, Mar 2004.

[66] Th. Martin and R. Landauer. Wave-packet approach to noise in multichannel mesoscopic systems. *Phys. Rev. B*, 45(4):1742–1755, Jan 1992.

[67] M. L. Mehta. *Random Matrices.* Academic Press, 2004.

[68] P. A. Mello, P. Pereyra, and N. Kumar. Macroscopic approach to multichannel disordered conductors. *Annals of Physics*, 181(2):290 – 317, 1988.

[69] V. V. Naletov, V. Charbois, O. Klein, and C. Fermon. Quantitative measurement of the ferromagnetic resonance signal by force detection. *Appl. Phys. Lett.*, 83:3132, 2003.

[70] V. V. Naletov, G. de Loubens, V. Charbois, O. Klein, V. S. Tiberkevich, and A. N. Slavin. Ferromagnetic resonance spectroscopy of parametric magnons excited by a four-wave process. *Phys. Rev. B*, 75(14):140405, 2007.

[71] L. G. Pereira C. Deranlot F. Petroff G. Faini A. Fert O. Boulle, V. Cros. Shaped angular dependence of the spin-transfer torque and microwave generation without magnetic field. *Nat. Phys*, 3:492, 2007.

[72] Myriam Pannetier, Claude Fermon, Gerald Le Goff, Juha Simola, and Emma Kerr. Femtotesla magnetic field measurement with magnetoresistive sensors. *Science*, 304:1648–1650, 2004.

[73] Wanjun Park, David V. Baxter, S. Steenwyk, I. Moraru, W. P. Pratt, and J. Bass. Measurement of resistance and spin-memory loss (spin relaxation) at interfaces using sputtered current perpendicular-to-plane exchange-biased spin valves. *Phys. Rev. B*, 62(2):1178–1185, Jul 2000.

[74] B. Pigeau, G. de Loubens, O. Klein, A. Riegler, F. Lochner, G. Schmidt, L. W. Molenkamp, V. S. Tiberkevich, and A. N. Slavin. A frequency-controlled magnetic vortex memory. *Appl. Phys. Lett.*, 96(13):132506, 2010.

[75] Benjamin Pigeau, GrÃ©goire de Loubens, Olivier Klein, Andreas Riegler, Florian Lochner, Georg Schmidt, and Laurens W. Molenkamp. Optimal control of vortex-core polarity by resonant microwave pulses. *Nature Phys.*, 2010.

[76] W. H. Rippard, M. R. Pufall, S. Kaka, S. E. Russek, and T. J. Silva. Direct-Current Induced Dynamics in $Co_{90}Fe_{10}/Ni_{80}Fe_{20}$ Point Contacts. *Phys. Rev. Lett.*, 92(2):027201, 2004.

[77] M. A. Ruderman and C. Kittel. Indirect exchange coupling of nuclear magnetic moments by conduction electrons. *Phys. Rev.*, 96(1):99, Oct 1954.

[78] A. Ruotolo, V. Cros, B. Georges, A. Dussaux, J. Grollier, C. Deranlot, R. Guillemet, K. Bouzehouane, S. Fusil, and A. Fert. Phase-locking of magnetic vortices mediated by antivortices. *Nature Nanotech.*, 4:528–532, 2009.

[79] Valentin S. Rychkov, Simone Borlenghi, Henri Jaffres, Albert Fert, and Xavier Waintal. Spin torque and waviness in magnetic multilayers: A

bridge between valet-fert theory and quantum approaches. *Phys. Rev. Lett.*, 103(6):066602, Aug 2009.

[80] I. Rychkova, V. Rychkov, K. Kazymyrenko, S. Borlenghi, and X. Waintal. KNIT : An open source code for quantum transport in multi-terminal systems. *ArXiv e-prints*, October 2010.

[81] D. La Tourette S. Neil, D. Markham. Magnetoresistive measurements of exchange constant in varied-thickness permalloy films. *J. Appl. Phys.*, 65(11):4362–4365, 1989.

[82] J. C. Sankey, P. M. Braganca, A. G. F. Garcia, I. N. Krivorotov, R. A. Buhrman, and D. C. Ralph. Spin-Transfer-Driven Ferromagnetic resonance of Individual Nanomagnets. *Phys. Rev. Lett.*, 96(22):227601, 2006.

[83] Ernst Schlömann. Ferromagnetic resonance at high power levels. Technical report, Technical Report No. R-48, 1959. (unpublished).

[84] Lewis T.O. Shurbet, G.L. and Boullion. Quadraticmatrix equations. *The Ohio Journal of Science*, 74.

[85] A. Slavin and V. Tiberkevich. Nonlinear auto-oscillator theory of microwave generation by spin-polarized current. *IEEE Trans. Magn.*, 45(4):1875–1918, 2009.

[86] A. N. Slavin and V. S. Tiberkevich. Nonlinear self-phase-locking effect in an array of current-driven magnetic nanocontacts. *Phys. Rev. B*, 72(9):092407, 2005.

[87] A. N. Slavin and V. S. Tiberkevich. Theory of mutual phase locking of spin-torque nanosized oscillators. *Phys. Rev. B*, 74(10):104401, 2006.

[88] J. C. Slonczewski. Current-driven excitation of magnetic multilayers. *Journal of Magnetism and Magnetic Materials*, 159(1-2):L1 – L7, 1996.

[89] M. D. Stiles and A. Zangwill. Noncollinear spin transfer in co/cu/co multilayers (invited). *Journal of Applied Physics*, 91(10):6812–6817, 2002.

[90] Phillip Tabor, Vasil Tiberkevich, Andrei Slavin, and Sergei Urazhdin. Hysteretic synchronization of nonlinear spin-torque oscillators. *Phys. Rev. B*, 82(2):020407, 2010.

[91] S. Tandon, M. Beleggia, Y. Zhu, and M. De Graef. On the computation of the demagnetization tensor for uniformly magnetized particles of arbitrary shape. part i: analytical approach. *J. Magn. Magn. Mater.*, 271:9–26, 2004.

[92] Tomohiro Taniguchi, Satoshi Yakata, Hiroshi Imamura, and Yasuo Ando. Determination of penetration depth of transverse spin current in ferromagnetic metals by spin pumping. *Applied Physics Express*, 1(3):031302, 2008.

[93] S. Tarucha, T. Saku, Y. Tokura, and Y. Hirayama. Sharvin resistance and its breakdown observed in long ballistic channels. *Phys. Rev. B*, 47(7):4064–4067, Feb 1993.

[94] Yaroslav Tserkovnyak, Arne Brataas, Gerrit E. W. Bauer, and Bertrand I. Halperin. Nonlocal magnetization dynamics in ferromagnetic heterostructures. *Rev. Mod. Phys.*, 77(4):1375–1421, Dec 2005.

[95] M. Tsoi, A. G. M. Jansen, J. Bass, W.-C. Chiang, M. Seck, V. Tsoi, and P. Wyder. Excitation of a Magnetic Multilayer by an Electric Current. *Phys. Rev. Lett.*, 80(19):4281–4284, 1998.

[96] Sergei Urazhdin, Phillip Tabor, Vasil Tiberkevich, and Andrei Slavin. Fractional synchronization of spin-torque nano-oscillators. *Phys. Rev. Lett.*, 105(10):104101, 2010.

[97] T. Valet and A. Fert. Theory of the perpendicular magnetoresistance in magnetic multilayers. *Phys. Rev. B*, 48(10):7099–7113, Sep 1993.

[98] P. C. van Son, H. van Kempen, and P. Wyder. Boundary resistance of the ferromagnetic-nonferromagnetic metal interface. *Phys. Rev. Lett.*, 58(21):2271–2273, May 1987.

[99] B. J. van Wees, H. van Houten, C. W. J. Beenakker, J. G. Williamson, L. P. Kouwenhoven, D. van der Marel, and C. T. Foxon. Quantized conductance of point contacts in a two-dimensional electron gas. *Phys. Rev. Lett.*, 60(9):848–850, Feb 1988.

[100] N. Vukadinovic and F. Boust. Three-dimensional micromagnetic simulations of magnetic excitations in cylindrical nanodots with perpendicular anisotropy. *Phys. Rev. B*, 75(1):014420, 2007.

[101] K. Wago, D. Botkin, C. S. Yannoni, and D. Rugar. Paramagnetic and ferromagnetic resonance imaging with a tip-on-cantilever magnetic resonance force microscope. *Appl. Phys. Lett.*, 72:2757, 1998.

[102] Xavier Waintal and Piet W. Brouwer. Magnetic exchange interaction induced by a josephson current. *Phys. Rev. B*, 65(5):054407, Jan 2002.

[103] Xavier Waintal, Edward B. Myers, Piet W. Brouwer, and D. C. Ralph. Role of spin-dependent interface scattering in generating current-induced torques in magnetic multilayers. *Phys. Rev. B*, 62(18):12317–12327, Nov 2000.

[104] D A Wharam, M Pepper, H Ahmed, J E F Frost, D G Hasko, D C Peacock, D A Ritchie, and G A C Jones. Addition of the one-dimensional quantised ballistic resistance. *Journal of Physics C: Solid State Physics*, 21(24):L887, 1988.

[105] S.A. Wolf, D. D. Awschalom, R. A. Buhrman, J.M. Daughton, S. von Molnar, M. L. Roukes, A. Y. Chtchelkanova, and D. M. Treger. Spintronics: A Spin-Based Electronics Vision for the Future. *Science*, 294:1488, 2001.

[106] K. Xia, P. J. Kelly, G. E. W. Bauer, A. Brataas, and I. Turek. Spin torques in ferromagnetic/normal-metal structures. *Phys. Rev. B*, 65(22):220401, May 2002.

[107] K. Xia, P. J. Kelly, G. E. W. Bauer, I. Turek, J. Kudrnovský, and V. Drchal. Interface resistance of disordered magnetic multilayers. *Phys. Rev. B*, 63(6):064407, Jan 2001.

[108] Jiang Xiao, A. Zangwill, and M. D. Stiles. Macrospin models of spin transfer dynamics. *Phys. Rev. B*, 72(1):014446, Jul 2005.

[109] Q. Yang, P. Holody, S.-F. Lee, L. L. Henry, R. Loloee, P. A. Schroeder, W. P. Pratt, and J. Bass. Spin flip diffusion length and giant magnetoresistance at low temperatures. *Phys. Rev. Lett.*, 72(20):3274–3277, May 1994.

[110] Q. Yang, P. Holody, R. Loloee, L. L. Henry, W. P. Pratt, P. A. Schroeder, and J. Bass. Prediction and measurement of perpendicular giant magnetoresistances of co/cu/$ni_{84}fe_{16}$/cu multilayers. *Phys. Rev. B*, 51(5):3226–3229, Feb 1995.

[111] Kei Yosida. Magnetic properties of cu-mn alloys. *Phys. Rev.*, 106(5):893–898, Jun 1957.

[112] Z. Zhang, P. C. Hammel, and P. E. Wigen. Observation of ferromagnetic resonance in a microscopic sample using magnetic resonance force microscopy. *Appl. Phys. Lett.*, 68:2005, 1996.

RÉSUMÉ

Transport électronique et dynamique de l'aimantation dans des systèmes magnétiques

L'objectif de ce travail de thèse est de comprendre l'influence mutuelle entre le transport électronique et la dynamique de l'aimantation dans des nanostructures hybrides magnétiques métalliques.

Dans une première partie on a développé un modèle théorique, basé sur la théorie des matrices aléatories, pour décrire au niveau microscopique le transport dépendent du spin dans une nanostructure hétérogène. Ce modèle, appelé CRMT (pour Continuous Random Matrix Theory) a ensuite été traduit dans un code de simulation qui permet de calculer les proprietés locales (couple de transfert de spin, accumulation de spin et courant de spin) et macroscopiques (résistance) du transport dans des conducteurs ohmiques. Le modèle a été validé en le comparant avec une théorie du transport quantique basée sur le calcul des fonctions de Green hors équilibre. Le couplage des ce deux modèles a permis d'effectuer une description multi-échelle du transport dans des nanostructures métalliques hybrides, où les parties ohmiques sont décrites par CRMT et les parties purement quantiques par le formalisme des fonctions de Green.

CRMT a ensuite été incorporé dans un code de simulation micromagnétique, pour décrire de façon réaliste la texture spatiale de la dynamique de l'aimantation induite par le transfert de spin. L'originalité de cette approche réside dans la modélisation des mesures spectroscopiques utilisant une détection mécanique de la résonance ferromagnétique, conduites sur des oscillateurs à transport de spin. Ce travail a permis d'obtenir le diagramme de phase dynamique de l'aimantation, ainsi que les règles de sélection des ondes de spin et la compétition entre les modes propres du systeme lors du passage d'un courant continu à travers la multicouche, en accord partiel avec les données experimentales

Mots-clefs: multicouches magnetiques ; couple de transfert de spin ; approche multi-échelle ; résonance ferromagnétique ; ondes de spin ; règles de sélection.

ABSTRACT

Electronic transport and magnetization dynamics in magnetic systems

The aim of this thesis is to understand the mutual influence between electronic transport and magnetization dynamics in magnetic hybrid metallic nanostructures.

At firs, we have developed a theoretical model, based on random matrix theory, to desribe at microscopic level spin dependent transport in a heterogeneus nanostructure. This model, called Continuous Random Matrix Theory (CRMT), has been implemented in a simulation code that allows one to compute local (spin torque, spin accumulation and spin current) and macroscopic (resistance) transport properties of spin valves. To validate this model, we have compared it with a quantum theory of transport based on the non equilibrium Green's functions formalism. Coupling the two models has allowed to perform a multiscale description of metallic hybrid nanostructures, where ohmic parts are described using CRMT, while purely quantum parts are described using Green's functions.

Then, we have coupled CRMT to a micromagnetic simulation code, in order to describe the complex dynamics of the magnetization induced by spin transfer effect.

The originality of this approach consists in modelizing a spectroscopic experiment based on a mechanical detection of the of ferromagnetic resonance, and performed on a spin torque nano oscillator. This work has allowed us obtain the dynamical phase diagram of the magnetization, and to detect the selection rules for spin waves induced by spin torque, as well as the competion between the eigenmodes of the system when a dc current flows through the multilayer, in partial agreement with experimental data.

Keywords: magnetic multilayers; spin torque/spin transfer effect; multiscale approach; ferromagnetic resonance; spin waves; selection rules.